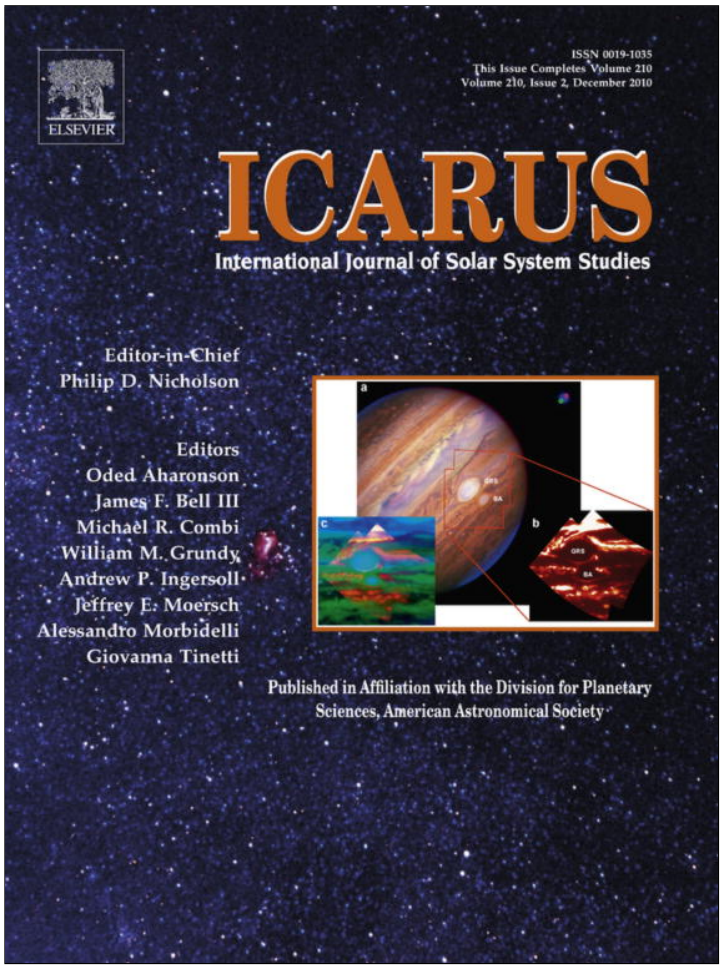

Icarus 210 (2010) 785–816

Contents lists available at ScienceDirect

Icarus

journal homepage: www.elsevier.com/locate/icarus

The opposition and tilt effects of Saturn's rings from HST observations

Heikki Salo [a,*], Richard G. French [b]

[a] Dept. of Physics, Astronomy Division, Univ. of Oulu, PO Box 3000, FI-90014, Finland
[b] Astronomy Department, Wellesley College, Wellesley, MA 02481, United States

ARTICLE INFO

Article history:
Received 30 March 2009
Revised 2 July 2010
Accepted 2 July 2010
Available online 1 August 2010

Keywords:
Saturn, Rings
Planetary rings
Hubble Space Telescope observations
Photometry
Radiative transfer

ABSTRACT

The two major factors contributing to the opposition brightening of Saturn's rings are (i) the *intrinsic brightening* of particles due to coherent backscattering and/or shadow hiding on their surfaces, and (ii) the *reduced interparticle shadowing* when the solar phase angle $\alpha \to 0°$. We utilize the extensive set of Hubble Space Telescope observations (Cuzzi, J.N., French, R.G., Dones, L. [2002]. Icarus 158, 199–223) for different elevation angles B and wavelengths λ to disentangle these contributions. We assume that the intrinsic contribution is independent of B, so that any B dependence of the phase curves is due to interparticle shadowing, which must also act similarly for all λ's. Our study complements that of Poulet et al. (Poulet, F., Cuzzi, J.N., French, R.G., Dones, L. [2002]. Icarus 158, 224), who used a subset of data for a single $B \sim 10°$, and the French et al. (French, R.G., Verbiscer, A., Salo, H., McGhee, C.A., Dones, L. [2007b] PASP 119, 623–642) study for the $B \sim 23°$ data set that included exact opposition. We construct a grid of dynamical/photometric simulation models, with the method of Salo and Karjalainen (Salo and Karjalainen [2003]. Icarus 164, 428–460), and use these simulations to fit the elevation-dependent part of opposition brightening. Eliminating the modeled interparticle component yields the intrinsic contribution to the opposition effect: for the B and A rings it is almost entirely due to coherent backscattering; for the C ring, an intraparticle shadow hiding contribution may also be present.

Based on our simulations, the width of the interparticle shadowing effect is roughly proportional to B. This follows from the observation that as B decreases, the scattering is primarily from the rarefied low filling factor upper ring layers, whereas at larger B's the dense inner parts are visible. Vertical segregation of particle sizes further enhances this effect. The elevation angle dependence of interparticle shadowing also explains most of the B ring tilt effect (the increase of brightness with elevation). From comparison of the magnitude of the tilt effect at different filters, we show that multiple scattering can account for at most a 10% brightness increase as $B \to 26°$, whereas the remaining 20% brightening is due to a variable degree of interparticle shadowing. The negative tilt effect of the middle A ring is well explained by the the same self-gravity wake models that account for the observed A ring azimuthal brightness asymmetry (Salo, H., Karjalainen, R., French, R.G. [2004]. Icarus 170, 70–90; French, R.G., Salo, H., McGhee, C.A., Dones, L. [2007]. Icarus 189, 493–522).

1. Introduction

Saturn's rings, like most atmosphereless objects in the Solar System, exhibit an opposition effect: a rapid increase in the brightness when the Sun-observer phase angle $\alpha \to 0°$. Most strikingly, this has been demonstrated directly by the zero-phase Cassini images (Déau et al., submitted for publication), showing a bright localized spot on the ring location centered at exact opposition. Similarly, Hubble Space Telescope observations during the exceptional 2005 opposition (French et al., 2007b) revealed that the brightness increase continues all the way to zero phase angle: in 2005, the Earth was transiting the Sun as seen from Saturn, implying a minimum α set by the finite solar radius of 0.029°, with the brightness increasing by about 1/3 for $\alpha < 0.5°$, in addition to a similar increase between $0.5° < \alpha < 6°$.

Two main explanations have been offered for the opposition brightening of Saturn's rings: (1) the intrinsic brightening of the grainy ring particle surfaces, and (2) the reduced amount of mutual interparticle shadowing between ring particles, as the phase angle $\alpha \to 0°$. The main contributor to intrinsic brightening is likely to be the coherent backscattering mechanism (CB), based on constructive interference between the incoming and outgoing light rays (Akkermans et al., 1988; Shkuratov, 1988; Hapke, 1990; Muinonen et al., 1991; Mishchenko, 1992), although shadow hiding (SH) at the particle's surface (Hapke, 2002) may also contribute. Coherent backscattering, as well as surface shadow hiding, are complicated functions of the particle surface structure and optical properties

* Corresponding author.
E-mail address: heikki.salo@oulu.fi (H. Salo).

0019-1035/$ - see front matter © 2010 Elsevier Inc. All rights reserved.
doi:10.1016/j.icarus.2010.07.002

of the grains; these mechanisms are currently topics of extensive theoretical and laboratory studies (Nelson et al., 2000, 2002; Hapke et al., 2006, 2009; Shepard and Helfenstein, 2007; Shkuratov et al., 2007). In contrast, the interparticle shadowing (e.g. Hapke, 1986; Irvine, 1966) contribution is not sensitive to physical particle properties, but is primarily determined by the optical depth and volume filling factor of the ring. In what follows, we will consistently call this latter effect "interparticle shadowing," rather than "shadow hiding" or "mutual shadowing," in order to avoid any possible misinterpretation in terms of shadows associated with roughness of the surfaces of ring particles.

Classically, the strong and narrow opposition brightening of Saturn's rings was interpreted in terms of interparticle shadowing in a low volume density ring. Near to opposition, the shadow a particle casts on other particles becomes more and more hidden by the particle itself. The smaller the volume density, the longer the average shadow cylinders are before hiding another particle: a more precise alignment of illumination and viewing is thus needed for this effect to become important. In particular, Lumme et al. (1983) calculated the interparticle shadowing contributions for homogeneous B ring models, and showed that the then-existing phase curves could be accounted for solely by this effect, provided that the ring has a low volume density of the order of $D \approx 0.02$. This corresponds in the case of identical particles to a multilayer with a thickness of several tens of particle diameters. Such a low volume density seemed to contradict dynamical models (e.g. Araki and Tremaine, 1986; Wisdom and Tremaine, 1988; Salo, 1992a) that, based on the laboratory measurements of the elasticity of ice (Bridges et al., 1984), predicted that the rings should flatten to a closely packed near-monolayer state with a thickness of few particle diameters at most, indicating $D > 0.1$. For such a large volume density, a homogeneous ring would have a much wider opposition effect than the observed brightening. Therefore, Mishchenko and Dlugach (1992) and Mishchenko (1993) suggested that the brightening is instead due to CB (see also Muinonen et al., 1991).[1] Mishchenko (1993) also argued that CB is strongly supported by the Lyot (1929) and Johnson et al. (1980) measurements of negative linear polarization, whose magnitude drops rapidly within $\alpha < 0.5°$. Indeed, during 1990s the CB became accepted as the standard explanation for Saturn's rings opposition effect, and the Cassini VIMS observations have also been interpreted within this framework (Nelson, 2008).

However, the interpretation of the opposition effect solely in terms of intrinsic brightening has a severe problem: improved dynamical models of flattened rings *do in fact predict* a fairly narrow interparticle shadowing opposition peak, if a particle size distribution is taken into account (Salo and Karjalainen, 2003; hereafter SK2003). This is because, for a fixed D, the effective mean width of shadow cylinders drops faster than their mean length when the size distribution is broadened. Photometric simulations in SK2003 indicate that the effect is well-matched by Hapke (1986) size distribution models for semi-infinite particle layers. Interestingly, if the currently favored wide particle size distributions with width $R_{max}/R_{min} \sim 100$ (Marouf et al., 1983; French and Nicholson, 2000) are assumed, interparticle shadowing can account for most of the opposition brightening for $\alpha > 0.5°$, and even have a significant contribution for $\alpha < 0.5°$ (SK2003; French et al., 2007b). Nevertheless, the strong surge near $\alpha = 0°$ and the wavelength dependence of phase curves (French et al., 2007b) unambiguously show the intrinsic contribution to be present. Therefore, both intrinsic and interparticle shadowing mechanisms are likely to affect the opposition brightening, although it has been surprisingly difficult to disentangle their contributions to the phase curves.

In this paper we propose that the *intrinsic brightening and interparticle shadowing can be reliably separated by a comparison of the opposition phase curves at different ring opening angles*. Namely, whereas the intrinsic contribution should be the same regardless of elevation, the interparticle shadowing contribution is expected to be very sensitive to the viewing elevation. This prediction follows from dynamical simulations, which indicate a vertically nonuniform particle distribution. As explored in detail in SK2003, the width of the modeled interparticle shadowing peak gets narrower for more shallow illumination, since the reflection will be more and more dominated by the low volume density upper layers; see Fig. 1 for an illustration. This B dependence of the effective volume density should be further augmented by the particle size distribution, since small particles are expected to have a larger scale height than the larger particles. Moreover, an extended particle size distribution will lead to a narrower opposition effect, in accordance with theoretical calculations (Hapke, 1986), although a broad particle size distribution alone, without vertical structure, does not imply a B-dependent opposition effect. To test these expectations, we will utilize the extensive set of UBVRI observations of Saturn's rings, obtained with the Hubble Space Telescope's WFPC2 (French et al., 2007b).

In order to separate the intrinsic and interparticle contributions, we will employ a set of dynamical simulation models performed with different optical depths and widths of the size distribution. The opposition phase curves are calculated for these models, covering the range of viewing elevations accessible from the Earth. We then match the observed elevation angle dependence with the simulated one, using the common phase curve range ($\alpha = 0.5$–$6.0°$) available for all elevations and filters, and obtain a set of best-fitting size distributions for the different ring components. The known contribution of interparticle shadowing in these simulation models, for any phase or elevation angle, can then be extracted from the observed data points, to yield opposition phase curves representing just the intrinsic contribution. The success of the extraction procedure can be tested by the requirement that the remaining intrinsic contribution must depend only on wavelength and ring location, and not on elevation angle.

An additional test for the importance of interparticle shadowing is provided by the B ring tilt effect (the reflectivity I/F increases with elevation by 30% for the ground based geometries), which is traditionally interpreted as resulting from increased multiple scattering at larger elevation angles (Esposito and Lumme, 1977; Lumme et al., 1983). In SK2003, we proposed that the tilt effect can also arise due to an elevation angle dependent opposition effect: at large elevations (say, $B = 26°$ as in Fig. 1) the observed brightness is enhanced by the wide interparticle shadowing opposition peak, which at smaller elevations ($B = 4°$ in Fig. 1) becomes so narrow that it is confined inside the typical observation phase angle of few degrees. The full HST data set, with sufficient B and α coverage, and excellent photometric accuracy, offers an ideal tool for testing this hypothesis. As a side result, we also obtain an accurate estimate for the amount of multiple scattering, and thus set constraints on the intrinsic ring particle phase function. Note that Cassini imaging data available to date, though having superior spatial resolution and a broader coverage of phase angles, do not enable such a systematic study of the opposition effect at different elevations.

The plan of the paper is as follows. In Section 2, we compare HST data at different elevations. We show that the observed phase curves are steeper at smaller elevation angles, and moreover that this steepening is independent of wavelength, consistent with what is expected for an interparticle shadowing effect. In Section 3, we devise a method for extracting the elevation-dependent part

[1] The notion of an intrinsic opposition peak originated much earlier; see e.g. Cook et al., 1973; Hämeen-Anttila and Vaaraniemi, 1975; Irvine et al., 1988.

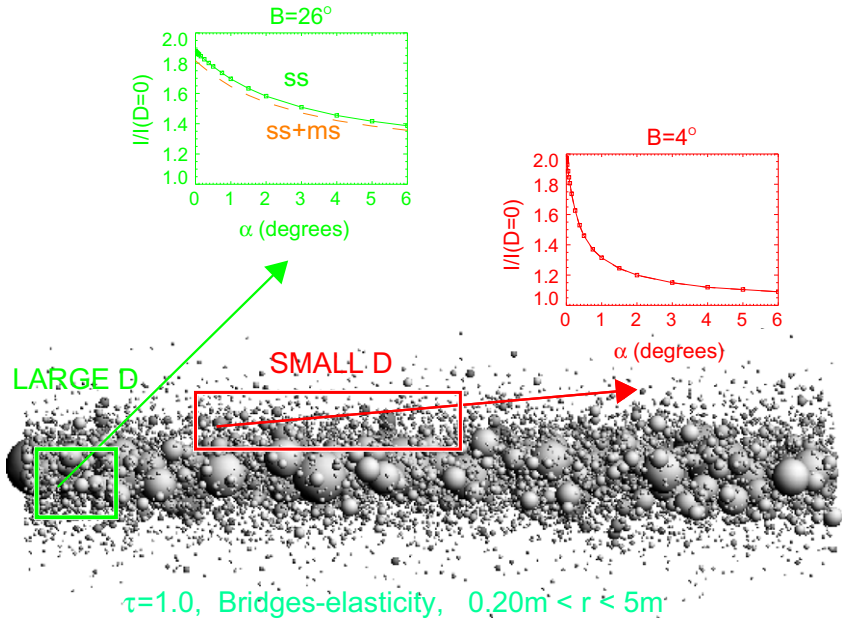

Fig. 1. An illustration of the opposition brightening due to reduced interparticle shadowing. A side view of a dynamical simulation model is displayed, together with opposition phase curves calculated for two different observing elevations. An $n_S = 3.09$ power-law phase function with Bond albedo 0.5 is assumed. The curves display $I/I(D = 0)$, where $I(D = 0)$ is the theoretical brightness for a classical zero volume density ring. The curves for the single scattering (ss) component and total brightness including multiple scattering (ss + ms) are shown separately, with solid and dashed lines (for $B = 4°$ the multiply-scattered component is negligible). At large elevation angles ($B = 26°$) the light rays are able to penetrate to central layers, where the typical particle separations are comparable to particle size: such a high volume density leads to a broad opposition brightening curve. On the other hand, at small elevation angles ($B = 4°$) the reflection happens mainly in the rarefied upper layers, where particle separations are large compared to their size: such a small effective volume density leads to a much narrower opposition effect.

of the opposition brightening, utilizing dynamical and photometric simulations. Section 4 then shows the results of fitting models to the observations, and discusses the implications for the relative magnitudes of the intra-particle and interparticle opposition effects. The intrinsic opposition effect phase curves are also presented in a tabular form, in terms of parameters for two different fitting formulas (a linear-exponential fit, and a simplified Hapke model including both CB and SH). Section 5 discusses the close interrelation between the interparticle mutual shadowing opposition effect and the tilt effect, and uses the observed tilt effect at different wavelengths to estimate the amount of multiple scattering. Section 6 summarizes our conclusions.

2. Elevation angle dependence of HST phase curves

2.1. Previous analysis of HST phase curves

There are two previous studies of the opposition phase curves based on a subset of the same HST observations used here. In Poulet et al. (2002), the HST data obtained during Cycle 7 for 10° elevation angle were fitted with various models for the intrinsic opposition effect, including the Hapke (1986) shadow hiding model, the Drossart (1993) fractal phase function, and the Shkuratov et al. (1999) model combining coherent backscattering and shadow hiding. However, no allowance was made for a possible interparticle shadowing contribution, and subsequent HST observations made it clear that the minimum $\alpha \approx 0.3°$ in the data utilized by Poulet et al. (2002) was too large to accurately constrain the models.

French et al. (2007b) combined the 2005 observations at exact opposition for ~23° elevation with the data from Cycles 10–12 at comparable elevation (~26°), which allowed for much more accurate fits of the phase curves than Poulet et al. (2002) were able to obtain. In particular, linear-exponential fits, and fits with the Hapke (2002) shadow hiding/coherent backscattering model, indicated that the HWHM of the opposition peak varies in the range 0.1–0.2°. The effect of interparticle shadowing was studied separately, using Monte Carlo simulations, which indicated that the observed opposition surge is stronger and narrower than what can be attributed even to a quite extended particle size distribution (with width $R_{max}/R_{min} \lesssim 100$). Nevertheless, the high-quality near-opposition phase curves (see Fig. 2 in French et al. (2007b)) give an impression of possibly two superposed components, the more extended of which might represent the interparticle contribution.

2.2. HST observations at different elevations

In the current study we use the full HST data set for $|B| = 4.5–26°$ (see Table 1 in French et al. (2007b)), which has been processed and calibrated as described in French et al. (2007a). Throughout our analysis we use the *geometrically corrected* I/F (Hämeen-Anttila and Pyykko, 1972; Dones et al., 1993; and Cuzzi et al., 2002), obtained by reducing the observations at slightly different B and B' (the elevation angles of the Earth and the Sun, respectively) to an effective common elevation angle B_{eff}:

$$\sin B_{eff} \equiv \mu_{eff} = \frac{2\mu\mu'}{\mu + \mu'}, \tag{1}$$

where $\mu \equiv |\sin B|$ and $\mu' \equiv |\sin B'|$, by

$$(I/F)_{corr} = (I/F)\frac{\mu + \mu'}{2\mu'}. \tag{2}$$

This correction factor is exact for the reflected singly scattered light[2] from a classical many-particle thick ring (volume density $D \to 0$), and should hold quite well even when multiple scattering is included (Lumme, 1970; Price, 1973) or when scattering from a

[2] The formula for the singly scattered reflected light is given by Eq. (6) in Section 3.1. When the correction factor is applied to single scattering, $\frac{\mu+\mu'}{2\mu'} \times (I/F)_{ss}(\mu, \mu') = \frac{A p}{8}(1 - \exp(-2\tau/\mu_{eff}))$, which equals $(I/F)_{ss}(\mu = \mu' = \mu_{eff})$ for all values of τ.

realistic geometrically thin particle disk is considered. Inclusion of this geometric correction is very important in our case, where observations from different elevation angles are compared with each other. For large α there can be significant differences in B and B', and the correction factor $\frac{\mu+\mu'}{2\mu'}$ may amount to as much as 20% for low elevation observations. If uncorrected, this spurious effect of variable observing geometries would easily overwhelm the true elevation angle dependence of ring brightness. During a single HST Cycle, $B_{\rm eff}$ is more or less constant (within a few tenths of degree) although B and B' may vary by a few degrees (see Table 1 in French et al. (2007a); Fig. 1 in French et al. (2007b)). This will allow us to group together all data from each individual HST Cycle. In what follows, we will omit the subscript and denote the geometrically corrected observed brightnesses simply as I/F.

To illustrate that a clear elevation angle dependent contribution is indeed present in the full HST data set, Fig. 2 compares the radial I/F profiles at large elevation ($B_{\rm eff} \sim 23°$) with those at $B_{\rm eff} = 4.5°$, which is the lowest elevation angle for which observations are available. The solid lines indicate observations at phase angles close to 6°, 2°, and 0.5°. Indeed, for $B_{\rm eff} = 4.5°$ the relative brightening as α decreases is clearly stronger. For example, the typical B ring I/F is enhanced by about 25% when α decreases from 6° to 2° for $B_{\rm eff} = 4.5°$, but only by about 15% for $B_{\rm eff} = 23°$ (Fig. 3). A similar increase is seen between $\alpha \sim 2°$ and $\sim$0.5°. The fact that the relative enhancement increases for lower B is qualitatively in agreement with the interparticle shadowing example of Fig. 1; in Section 3 we will make a more detailed comparison to our Monte Carlo models, after first characterizing the elevation angle dependence of the observations. The figure also shows the I/F profile for $B = 22.9°$, obtained at exact opposition (French et al., 2007b), illustrating that a major part of the opposition brightening takes place inside $\alpha \sim 0.5°$.

The magnitude of opposition brightening and its dependence on elevation (at least for the broader component outside $\alpha = 0.5°$) are fairly similar for the C ring in comparison to the optically much denser B and A rings (see Fig. 3). At first glance, this might appear to contradict the importance of interparticle shadowing, which is expected to be very sensitive to τ. Nevertheless, there seems to be a positive correlation between brightness increase and the local optical depth, as required if at least part of the brightening is due to reduced interparticle shadowing. A similar correlation between the slope of the phase curve at $B_{\rm eff} \sim 26°$ and the C ring optical depth was discussed in French et al. (2007b).

In French et al. (2007b), the high elevation angle data set (Cycles 10–13) was analyzed in detail for three ring regions: $a = 78{,}000$–$83{,}000$ km (the C ring; this region excludes most prominent ringlets and plateaus), $a = 100{,}000$–$107{,}000$ km (the B ring), and $a = 127{,}000$–$129{,}000$ km (the A ring; this is the region where the azimuthal brightness asymmetry is strongest).

Since the data covered phase angles near to zero, it was possible to fit various detailed backscattering models to the phase curves. In particular, besides the physically-motivated Hapke (2002) models, it was shown that the data are quite well described by an empirical linear-exponential model

$$\frac{I(\alpha)}{F} = a' \exp(-\alpha/d') + b' + k'\alpha, \tag{3}$$

commonly used for fitting of satellite and asteroid near-opposition phase curves (Kaasalainen et al., 2003). The parameters a' and d' describe the amplitude and width of the narrow opposition peak, while b' and k' give the background intensity and linear slope of the phase curve. The half-width at half-maximum for the exponential component is HWHM = $d'\ln 2$. In French et al. (2007b) a detailed analysis of the model parameters was presented as a function of ring location and wavelength.

Unfortunately, at the smaller elevation angles, the HST data are too sparse to allow such a four-parameter fit (or a Hapke fit with seven parameters). The data we use, in addition to those shown in Tables 2–4 in French et al. (2007b), are listed in Tables 1–3, representing measurements of average geometrically corrected I/F from Cycles 6–9 for the three ring regions (C, B, A) defined above. In some cases, there are measurements for only 3–4 distinct phase angles. Fig. 4 collects the phase curves for six sets of elevation angles, with the mean effective values of $B_{\rm eff} = 4.5°$, 10.2°, 15.4°, 20.1°, 23.6°, and 26.1° (Cycles 6, 7a, 7b, 8, 9 + 13, and 10 − 12, respectively). The curves are normalized to I/F at $\alpha = 6°$, and the two most-widely separated filters, F336W and F814W, are shown. For the lowest elevation angle, only two B ring phase angle data points

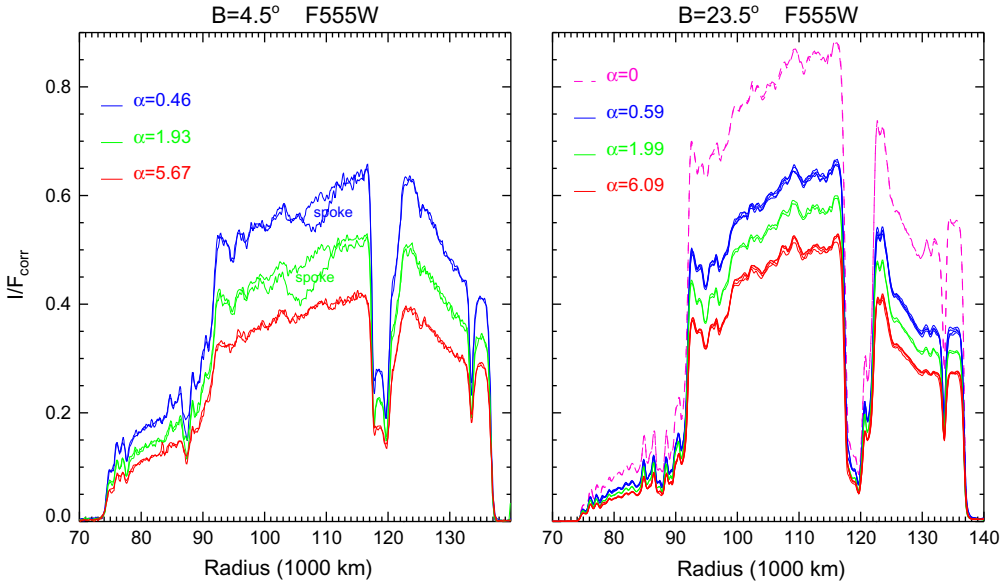

Fig. 2. Examples of the ansa I/F profiles for $B_{\rm eff} = 4.5°$ (left) and for $B_{\rm eff} = 23.5°$ (right). Solid lines collect the observations in F555W filter close to common phase angles $\alpha \sim 6°$, $\sim$2°, and $\sim$0.5°. The almost overlapping curves correspond to profiles extracted from adjacent east/west ansa images: note that for $B_{\rm eff} = 4.5°$ the images for the two lowest phase angles had spokes in the east ansa (McGhee et al., 2005), affecting the mid B ring profiles (the affected portions of these images are omitted from all subsequent analyses). At right, the profile at exact opposition is also shown (for $B = 22.9°$). Here, as in all the subsequent plots, the corrected I/F is shown, compensating for the small differences in B and B' during each subset of observations.

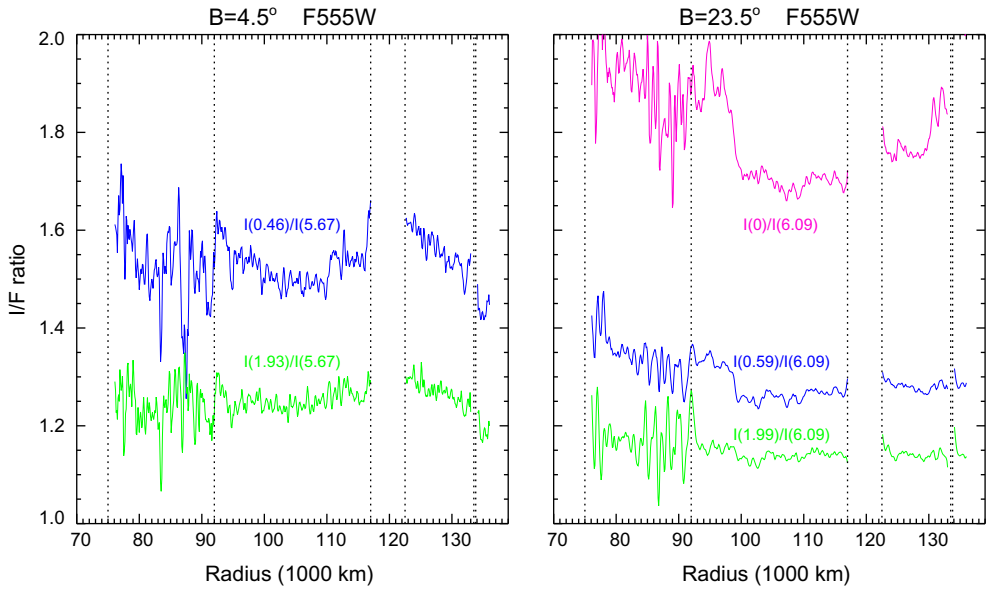

Fig. 3. Same as Fig. 2, except that the profiles have been divided by that at $\alpha \sim 6°$. Comparison of the two opening angles illustrates a clear elevation angle dependence in the magnitude of relative opposition brightening (at least for the common interval $0.5° < \alpha < 6°$).

are available for the F336W filter, due to the contamination of images by B ring spokes. Also shown in the plot are two-parameter log-linear fits of the form

$$\frac{I(\alpha)}{F} = a \ln \alpha + b. \tag{4}$$

These fits were also used in the normalization of the data to a common phase angle $\alpha = 6°$ in Fig. 4. In order to assure a uniform coverage of phase angles at different elevations, the fits were made restricting to values $\alpha > 0.25°$. Such simple fits seem to match the data quite well. Nevertheless, for the most extensive data sets ($B_{\rm eff} = 26.1°$, $23.6°$) it is evident that a steeper logarithmic slope would be appropriate for $\alpha < 0.5°$, justifying the use of more complicated fitting formulae when sufficient data are available. Note that the log-linear intensity fitting formula is in practice almost indistinguishable from the log-linear magnitude fits utilized by Lumme et al. (1983) and Bobrov (1970).

Concentrating on the wider regime $\alpha > 0.5°$, Fig. 4 suggests that the enhanced opposition brightening at smaller elevations is well captured by the log-linear fits. A systematic increase of the logarithmic slope with decreasing $B_{\rm eff}$ is seen in all filters for all ring regions. This is most clearly seen in Fig. 5, which compares the observations at different elevation angles for the F555W filter. The values of the parameters a and b, for different filters and ring regions, are listed in Table 4.

In order to further characterize the elevation angle dependence of opposition effect, and to separate the intrinsic and interparticle contribution, we turn to modeling in the next section.

3. Disentangling the mutual interparticle shadowing and intraparticle contributions

3.1. Mathematical formulation

We assume that the intensity at phase angle α, effective elevation angle $B_{\rm eff}$, normal optical depth τ, and wavelength λ, can be written in the form

$$(I/F)(\alpha, B_{\rm eff}, \tau, \lambda) = [f_i(\alpha, \lambda) f_e(\alpha, B_{\rm eff}, \tau) + Q_{ms}(B_{\rm eff}, \tau, \lambda)] \times (I/F)_{ss}(\alpha, B_{\rm eff}, \tau, \lambda), \tag{5}$$

where f_i denotes the *intrinsic* (e.g. due to coherent backscattering and/or shadow hiding at the particles' surfaces) and f_e the *external* (due to reduced interparticle mutual shadowing) contribution to the opposition brightening of the singly scattered radiation, Q_{ms} is the fractional contribution of multiple scattering, and $(I/F)_{ss}$ is the theoretical single scattering intensity of reflected light,

$$(I/F)_{ss} = \frac{A(\lambda) P(\alpha, \lambda) \mu'}{4(\mu + \mu')} \left(1 - \exp\left[-\tau\left(\frac{1}{\mu} + \frac{1}{\mu'}\right)\right]\right), \tag{6}$$

where A is the (possibly wavelength-dependent) Bond albedo of the particles and P is the particle phase function.[3] For a classical, zero volume density ring there is no interparticle shadowing, and thus $f_e = 1$. Likewise, $f_i = 1$ corresponds to the absence of an intrinsic opposition peak; the theoretical maxima for each of these factors is 2. Note that here Q_{ms} includes just the interparticle multiple scatterings, not the possible multiple reflection events at the particle surface, thought to be responsible for the coherent backscattering effect. Our goal is to separate the intrinsic and external contributions f_i and f_e. Note that our Eqs. (5) and (6) assume that the ring can be described by a single uniform optical depth, whereas the actual rings are known to possess local density variations due to self-gravity wakes (Colwell et al., 2006, 2007; Hedman et al., 2007). Besides such local variations, the resolution element of HST observations is so large that it includes a superposition of different optical depths, due to large scale radial structure of rings. Because of this, all the parameters in the equations, including τ, f_i, and f_e, must be considered as effective mean values.

In what follows we assume that f_i depends on wavelength but is independent of $B_{\rm eff}$ or τ. On the other hand, f_e is independent of wavelength, but is likely to depend on both $B_{\rm eff}$ and τ. The multiply-scattered contribution vanishes for $\tau \to 0$ and for $B_{\rm eff} \to 0$; in general its contribution is expected to be small for all Earth-based geometries (Cuzzi et al., 2002). We shall therefore ignore Q_{ms} in this section, an approximation that is justified in Section 5.

[3] The separation of particle's intrinsic opposition brightening and its phase function is somewhat arbitrary; here, the phase function $P(\alpha, \lambda)$ stands for the overall angular distribution of the scattered radiation due to surface topography and illumination.

Table 1
C ring: 78,000–83,000 km.

F336W		F439W		F555W		F675W		F814W	
α	I/F_{corr}	α	I/F_{corr}	α	I/F_{corr}	α	I/F_{corr}	α	I/F_{corr}
Cycle 6 $\|B_{eff}\|$ = 4.30–4.66°									
0.4605	0.1235	0.4607	0.1514	0.4609	0.1680	0.4611	0.1840	0.4613	0.1962
1.9249	0.0955	0.4617	0.1524	0.4619	0.1692	0.4621	0.1860	1.9257	0.1554
1.9315	0.0966	1.9251	0.1201	1.9253	0.1319	1.9255	0.1489	5.6708	0.1322
5.6705	0.0780	1.9318	0.1198	1.9320	0.1367	5.6709	0.1230	–	–
5.6711	0.0774	5.6704	0.0980	5.6704	0.1104	–	–	–	–
–	–	5.6710	0.0973	5.6709	0.1107	–	–	–	–
Cycle 7a $\|B_{eff}\|$ = 10.01–10.29°									
0.2997	0.0880	0.2998	0.1108	0.2998	0.1204	0.2998	0.1351	0.2999	0.1377
0.3000	0.0879	0.3000	0.1109	0.3000	0.1209	0.3000	0.1311	0.3001	0.1385
0.4948	0.0818	0.4946	0.1027	0.4944	0.1115	0.4943	0.1210	0.4941	0.1274
0.4958	0.0811	0.4956	0.1016	0.4954	0.1094	0.4952	0.1209	0.4951	0.1260
0.9774	0.0733	0.4957	0.1014	0.9770	0.1014	0.9767	0.1099	0.9765	0.1169
0.9843	0.0717	0.9772	0.0930	0.9837	0.0985	0.9834	0.1087	0.9832	0.1132
1.9911	0.0650	0.9839	0.0911	1.9906	0.0905	1.9904	0.0999	1.9901	0.1043
1.9979	0.0645	0.9840	0.0910	1.9975	0.0893	1.9972	0.0992	1.9970	0.1027
6.0165	0.0554	1.9908	0.0831	6.0165	0.0790	6.0165	0.0858	6.0165	0.0903
6.0168	0.0546	1.9977	0.0818	6.0168	0.0779	6.0168	0.0862	6.0169	0.0893
–	–	6.0165	0.0717	–	–	–	–	–	–
–	–	6.0165	0.0714	–	–	–	–	–	–
–	–	6.0165	0.0716	–	–	–	–	–	–
–	–	6.0165	0.0714	–	–	–	–	–	–
–	–	6.0168	0.0706	–	–	–	–	–	–
Cycle 7b $\|B_{eff}\|$ = 15.40–15.49°									
0.3156	0.0659	0.3156	0.0825	0.3158	0.0885	0.3158	0.0975	0.3159	0.1016
0.3160	0.0661	0.3157	0.0830	0.3162	0.0890	0.3163	0.0957	0.3164	0.1022
0.6866	0.0586	0.3161	0.0826	0.6861	0.0798	0.6859	0.0878	0.6857	0.0914
0.6927	0.0575	0.6864	0.0747	0.6923	0.0777	0.6921	0.0841	0.6918	0.0903
1.1982	0.0533	0.6925	0.0718	1.1978	0.0724	1.1975	0.0784	1.1973	0.0846
1.2042	0.0537	1.1980	0.0672	1.2034	0.0737	1.2031	0.0800	1.2029	0.0853
6.2567	0.0417	1.2036	0.0687	6.2567	0.0589	6.2566	0.0656	6.2566	0.0684
6.2568	0.0407	1.2038	0.0687	6.2567	0.0576	6.2567	0.0636	6.2567	0.0676
–	–	1.2039	0.0687	–	–	–	–	–	–
–	–	6.2567	0.0545	–	–	–	–	–	–
–	–	6.2567	0.0530	–	–	–	–	–	–
Cycle 8 $\|B_{eff}\|$ = 20.05–20.17°									
0.2956	0.0542	0.2957	0.0682	0.2958	0.0718	0.2959	0.0790	0.2959	0.0826
0.2971	0.0544	0.2957	0.0680	0.2958	0.0727	0.2973	0.0795	0.2973	0.0848
0.4244	0.0523	0.2957	0.0681	0.2958	0.0725	0.4233	0.0771	0.4231	0.0806
0.4257	0.0506	0.2972	0.0693	0.2972	0.0738	0.4251	0.0741	0.4249	0.0776
6.1038	0.0346	0.4240	0.0664	0.4235	0.0702	6.1037	0.0534	6.1036	0.0580
6.1052	0.0340	0.4241	0.0662	0.4236	0.0707	6.1049	0.0527	6.1049	0.0562
–	–	0.4242	0.0666	0.4238	0.0700	–	–	–	–
–	–	0.4255	0.0643	0.4253	0.0675	–	–	–	–
–	–	6.1038	0.0455	6.1037	0.0494	–	–	–	–
–	–	6.1051	0.0444	6.1050	0.0474	–	–	–	–
–	–	6.1051	0.0442	6.1050	0.0475	–	–	–	–
–	–	6.1052	0.0443	6.1050	0.0471	–	–	–	–
Cycle 9 $\|B_{eff}\|$ = 23.54–23.69°									
0.2681	0.0487	0.2682	0.0622	0.2683	0.0657	0.2684	0.0710	0.2685	0.0746
0.2702	0.0488	0.2682	0.0620	0.2684	0.0651	0.2705	0.0706	0.2706	0.0744
0.5852	0.0443	0.2703	0.0617	0.2704	0.0649	0.5862	0.0655	0.5864	0.0688
0.5870	0.0437	0.2703	0.0617	0.2704	0.0644	0.5880	0.0640	0.5882	0.0678
1.9914	0.0369	0.5854	0.0565	0.5858	0.0604	1.9925	0.0562	1.9929	0.0602
1.9915	0.0368	0.5856	0.0565	0.5860	0.0594	1.9927	0.0556	6.0951	0.0514
6.0947	0.0313	0.5873	0.0558	0.5876	0.0590	6.0950	0.0472	6.0954	0.0531
6.0952	0.0319	0.5874	0.0557	0.5878	0.0582	6.0954	0.0501	–	–
–	–	1.9918	0.0483	1.9922	0.0515	–	–	–	–
–	–	1.9919	0.0479	1.9923	0.0509	–	–	–	–
–	–	6.0948	0.0407	6.0949	0.0434	–	–	–	–
–	–	6.0948	0.0405	6.0949	0.0429	–	–	–	–
–	–	6.0948	0.0405	6.0950	0.0434	–	–	–	–
–	–	6.0953	0.0419	6.0953	0.0449	–	–	–	–

Table 2
B ring: 100,000–107,000 km.

F336W		F439W		F555W		F675W		F814W	
α	I/F_{corr}	α	I/F_{corr}	α	I/F_{corr}	α	I/F_{corr}	α	I/F_{corr}
Cycle 6 $\lvert B_{eff}\rvert$ = 4.30–4.66°									
0.4605	0.2681	0.4607	0.4421	0.4609	0.5588	0.4611	0.6222	0.4613	0.6515
1.9249	0.1875	0.4617	0.4432	0.4619	0.5592	0.4621	0.6207	1.9257	0.5055
1.9315	0.2043	1.9251	0.3298	1.9253	0.4261	1.9255	0.4948	5.6708	0.4406
5.6705	0.1595	1.9318	0.3595	1.9320	0.4640	5.6709	0.4211	–	–
5.6711	0.1601	5.6704	0.2875	5.6704	0.3737	–	–	–	–
–	–	5.6710	0.2862	5.6709	0.3740	–	–	–	–
Cycle 7a $\lvert B_{eff}\rvert$ = 10.01–10.29°									
0.2997	0.2904	0.2998	0.4820	0.2998	0.6062	0.2998	0.6760	0.2999	0.7053
0.3000	0.2932	0.3000	0.4845	0.3000	0.6087	0.3000	0.6795	0.3001	0.7071
0.4948	0.2735	0.4946	0.4597	0.4944	0.5813	0.4943	0.6507	0.4941	0.6734
0.4958	0.2774	0.4956	0.4650	0.4954	0.5794	0.4952	0.6590	0.4951	0.6701
0.9774	0.2497	0.4957	0.4652	0.9770	0.5447	0.9767	0.6118	0.9765	0.6351
0.9843	0.2523	0.9772	0.4263	0.9837	0.5474	0.9834	0.6261	0.9832	0.6359
1.9911	0.2249	0.9839	0.4331	1.9906	0.5028	1.9904	0.5775	1.9901	0.5874
1.9979	0.2246	0.9840	0.4326	1.9975	0.5059	1.9972	0.5821	1.9970	0.5908
6.0165	0.1768	1.9908	0.3935	6.0165	0.4227	6.0165	0.4789	6.0165	0.4988
6.0168	0.1785	1.9977	0.3965	6.0168	0.4221	6.0168	0.4881	6.0169	0.4963
–	–	6.0165	0.3228	–	–	–	–	–	–
–	–	6.0165	0.3223	–	–	–	–	–	–
–	–	6.0165	0.3228	–	–	–	–	–	–
–	–	6.0165	0.3218	–	–	–	–	–	–
–	–	6.0168	0.3255	–	–	–	–	–	–
Cycle 7b $\lvert B_{eff}\rvert$ = 15.40–15.49°									
0.3156	0.2935	0.3156	0.4891	0.3158	0.6099	0.3158	0.6928	0.3159	0.7053
0.3160	0.2947	0.3157	0.4890	0.3162	0.6153	0.3163	0.6863	0.3164	0.7118
0.6866	0.2661	0.3161	0.4895	0.6861	0.5673	0.6859	0.6475	0.6857	0.6582
0.6927	0.2672	0.6864	0.4508	0.6923	0.5756	0.6921	0.6427	0.6918	0.6672
1.1982	0.2469	0.6925	0.4545	1.1978	0.5495	1.1975	0.6175	1.1973	0.6417
1.2042	0.2426	1.1980	0.4288	1.2034	0.5440	1.2031	0.6129	1.2029	0.6368
6.2567	0.1867	1.2036	0.4223	6.2567	0.4405	6.2566	0.5088	6.2566	0.5189
6.2568	0.1862	1.2038	0.4217	6.2567	0.4441	6.2567	0.5139	6.2567	0.5231
–	–	1.2039	0.4216	–	–	–	–	–	–
–	–	6.2567	0.3381	–	–	–	–	–	–
–	–	6.2567	0.3419	–	–	–	–	–	–
Cycle 8 $\lvert B_{eff}\rvert$ = 20.05–20.17°									
0.2956	0.2971	0.2957	0.4951	0.2958	0.6180	0.2959	0.7049	0.2959	0.7174
0.2971	0.2968	0.2957	0.4940	0.2958	0.6241	0.2973	0.6932	0.2973	0.7214
0.4244	0.2814	0.2957	0.4951	0.2958	0.6183	0.4233	0.6774	0.4231	0.6886
0.4257	0.2818	0.2972	0.4924	0.2972	0.6201	0.4251	0.6785	0.4249	0.6899
6.1038	0.1890	0.4240	0.4731	0.4235	0.5935	6.1037	0.5202	6.1036	0.5417
6.1052	0.1899	0.4241	0.4725	0.4236	0.5995	6.1049	0.5300	6.1049	0.5402
–	–	0.4242	0.4727	0.4238	0.5940	–	–	–	–
–	–	0.4255	0.4752	0.4253	0.5957	–	–	–	–
–	–	6.1038	0.3459	6.1037	0.4568	–	–	–	–
–	–	6.1051	0.3496	6.1050	0.4561	–	–	–	–
–	–	6.1051	0.3493	6.1050	0.4606	–	–	–	–
–	–	6.1052	0.3494	6.1050	0.4563	–	–	–	–
Cycle 9 $\lvert B_{eff}\rvert$ = 23.54–23.69°									
0.2681	0.2992	0.2682	0.4980	0.2683	0.6286	0.2684	0.7115	0.2685	0.7241
0.2702	0.2991	0.2682	0.4974	0.2684	0.6223	0.2705	0.7090	0.2706	0.7229
0.5852	0.2706	0.2703	0.4970	0.2704	0.6261	0.5862	0.6644	0.5864	0.6751
0.5870	0.2702	0.2703	0.4961	0.2704	0.6212	0.5880	0.6665	0.5882	0.6779
1.9914	0.2286	0.5854	0.4588	0.5858	0.5847	1.9925	0.6038	1.9929	0.6219
1.9915	0.2288	0.5856	0.4583	0.5860	0.5781	1.9927	0.5970	6.0951	0.5538
6.0947	0.1929	0.5873	0.4590	0.5876	0.5868	6.0950	0.5318	6.0954	0.5438
6.0952	0.1928	0.5874	0.4591	0.5878	0.5804	6.0954	0.5341	–	–
–	–	1.9918	0.4068	1.9922	0.5277	–	–	–	–
–	–	1.9919	0.4061	1.9923	0.5229	–	–	–	–
–	–	6.0948	0.3531	6.0949	0.4669	–	–	–	–
–	–	6.0948	0.3538	6.0949	0.4622	–	–	–	–
–	–	6.0948	0.3531	6.0950	0.4664	–	–	–	–
–	–	6.0953	0.3493	6.0953	0.4578	–	–	–	–

Table 3
A ring: 127,000–129,000 km.

F336W		F439W		F555W		F675W		F814W	
α	I/F_{corr}	α	I/F_{corr}	α	I/F_{corr}	α	I/F_{corr}	α	I/F_{corr}
Cycle 6 $\|B_{eff}\|$ = 4.30–4.66°									
0.4605	0.2768	0.4607	0.4358	0.4609	0.5275	0.4611	0.5746	0.4613	0.6017
1.9249	0.2126	0.4617	0.4409	0.4619	0.5300	0.4621	0.5769	1.9257	0.4918
1.9315	0.2100	1.9251	0.3497	1.9253	0.4247	1.9255	0.4806	5.6708	0.3935
5.6705	0.1600	1.9318	0.3512	1.9320	0.4326	5.6709	0.3755	–	–
5.6711	0.1609	5.6704	0.2772	5.6704	0.3396	–	–	–	–
–	–	5.6710	0.2733	5.6709	0.3405	–	–	–	–
Cycle 7a $\|B_{eff}\|$ = 10.01–10.29°									
0.2997	0.2594	0.2998	0.4071	0.2998	0.4943	0.2998	0.5417	0.2999	0.5658
0.3000	0.2592	0.3000	0.4057	0.3000	0.4891	0.3000	0.5375	0.3001	0.5601
0.4948	0.2436	0.4946	0.3832	0.4944	0.4652	0.4943	0.5116	0.4941	0.5339
0.4958	0.2446	0.4956	0.3883	0.4954	0.4676	0.4952	0.5218	0.4951	0.5301
0.9774	0.2202	0.4957	0.3883	0.9770	0.4366	0.9767	0.4796	0.9765	0.4993
0.9843	0.2247	0.9772	0.3544	0.9837	0.4375	0.9834	0.4886	0.9832	0.4998
1.9911	0.1976	0.9839	0.3603	1.9906	0.3993	1.9904	0.4490	1.9901	0.4596
1.9979	0.1994	0.9840	0.3600	1.9975	0.4033	1.9972	0.4533	1.9970	0.4636
6.0165	0.1516	1.9908	0.3239	6.0165	0.3278	6.0165	0.3622	6.0165	0.3789
6.0168	0.1530	1.9977	0.3303	6.0168	0.3271	6.0168	0.3705	6.0169	0.3790
–	–	6.0165	0.2590	–	–	–	–	–	–
–	–	6.0165	0.2590	–	–	–	–	–	–
–	–	6.0165	0.2594	–	–	–	–	–	–
–	–	6.0165	0.2582	–	–	–	–	–	–
–	–	6.0168	0.2631	–	–	–	–	–	–
Cycle 7b $\|B_{eff}\|$ = 15.40–15.49°									
0.3156	0.2369	0.3156	0.3697	0.3158	0.4442	0.3158	0.4940	0.3159	0.5037
0.3160	0.2382	0.3157	0.3702	0.3162	0.4486	0.3163	0.4898	0.3164	0.5105
0.6866	0.2129	0.3161	0.3711	0.6861	0.4081	0.6859	0.4540	0.6857	0.4638
0.6927	0.2146	0.6864	0.3371	0.6923	0.4175	0.6921	0.4554	0.6918	0.4709
1.1982	0.1965	0.6925	0.3435	1.1978	0.3942	1.1975	0.4335	1.1973	0.4513
1.2042	0.1944	1.1980	0.3214	1.2034	0.3897	1.2031	0.4296	1.2029	0.4469
6.2567	0.1470	1.2036	0.3154	6.2567	0.3128	6.2566	0.3538	6.2566	0.3620
6.2568	0.1497	1.2038	0.3158	6.2567	0.3176	6.2567	0.3602	6.2567	0.3669
–	–	1.2039	0.3158	–	–	–	–	–	–
–	–	6.2567	0.2497	–	–	–	–	–	–
–	–	6.2567	0.2550	–	–	–	–	–	–
Cycle 8 $\|B_{eff}\|$ = 20.05–20.17°									
0.2956	0.2253	0.2957	0.3505	0.2958	0.4209	0.2959	0.4713	0.2959	0.4798
0.2971	0.2233	0.2957	0.3506	0.2958	0.4249	0.2973	0.4600	0.2973	0.4795
0.4244	0.2125	0.2957	0.3504	0.2958	0.4213	0.4233	0.4481	0.4231	0.4558
0.4257	0.2132	0.2972	0.3491	0.2972	0.4203	0.4251	0.4533	0.4249	0.4598
6.1038	0.1402	0.4240	0.3335	0.4235	0.4015	6.1037	0.3382	6.1036	0.3518
6.1052	0.1437	0.4241	0.3333	0.4236	0.4043	6.1049	0.3480	6.1049	0.3567
–	–	0.4242	0.3331	0.4238	0.4014	–	–	–	–
–	–	0.4255	0.3375	0.4253	0.4054	–	–	–	–
–	–	6.1038	0.2409	6.1037	0.3041	–	–	–	–
–	–	6.1051	0.2466	6.1050	0.3068	–	–	–	–
–	–	6.1051	0.2455	6.1050	0.3097	–	–	–	–
–	–	6.1052	0.2461	6.1050	0.3069	–	–	–	–
Cycle 9 $\|B_{eff}\|$ = 23.54–23.69°									
0.2681	0.2199	0.2682	0.3414	0.2683	0.4118	0.2684	0.4572	0.2685	0.4671
0.2702	0.2200	0.2682	0.3412	0.2684	0.4083	0.2705	0.4571	0.2706	0.4669
0.5852	0.1976	0.2703	0.3424	0.2704	0.4130	0.5862	0.4241	0.5864	0.4318
0.5870	0.1950	0.2703	0.3418	0.2704	0.4099	0.5880	0.4189	0.5882	0.4285
1.9914	0.1665	0.5854	0.3129	0.5858	0.3827	1.9925	0.3788	1.9929	0.3908
1.9915	0.1667	0.5856	0.3125	0.5860	0.3772	1.9927	0.3743	6.0951	0.3473
6.0947	0.1381	0.5873	0.3107	0.5876	0.3786	6.0950	0.3329	6.0954	0.3394
6.0952	0.1378	0.5874	0.3098	0.5878	0.3743	6.0954	0.3323	–	–
–	–	1.9918	0.2732	1.9922	0.3395	–	–	–	–
–	–	1.9919	0.2730	1.9923	0.3360	–	–	–	–
–	–	6.0948	0.2372	6.0949	0.2992	–	–	–	–
–	–	6.0948	0.2375	6.0949	0.2966	–	–	–	–
–	–	6.0948	0.2369	6.0950	0.2989	–	–	–	–
–	–	6.0953	0.2334	6.0953	0.2924	–	–	–	–

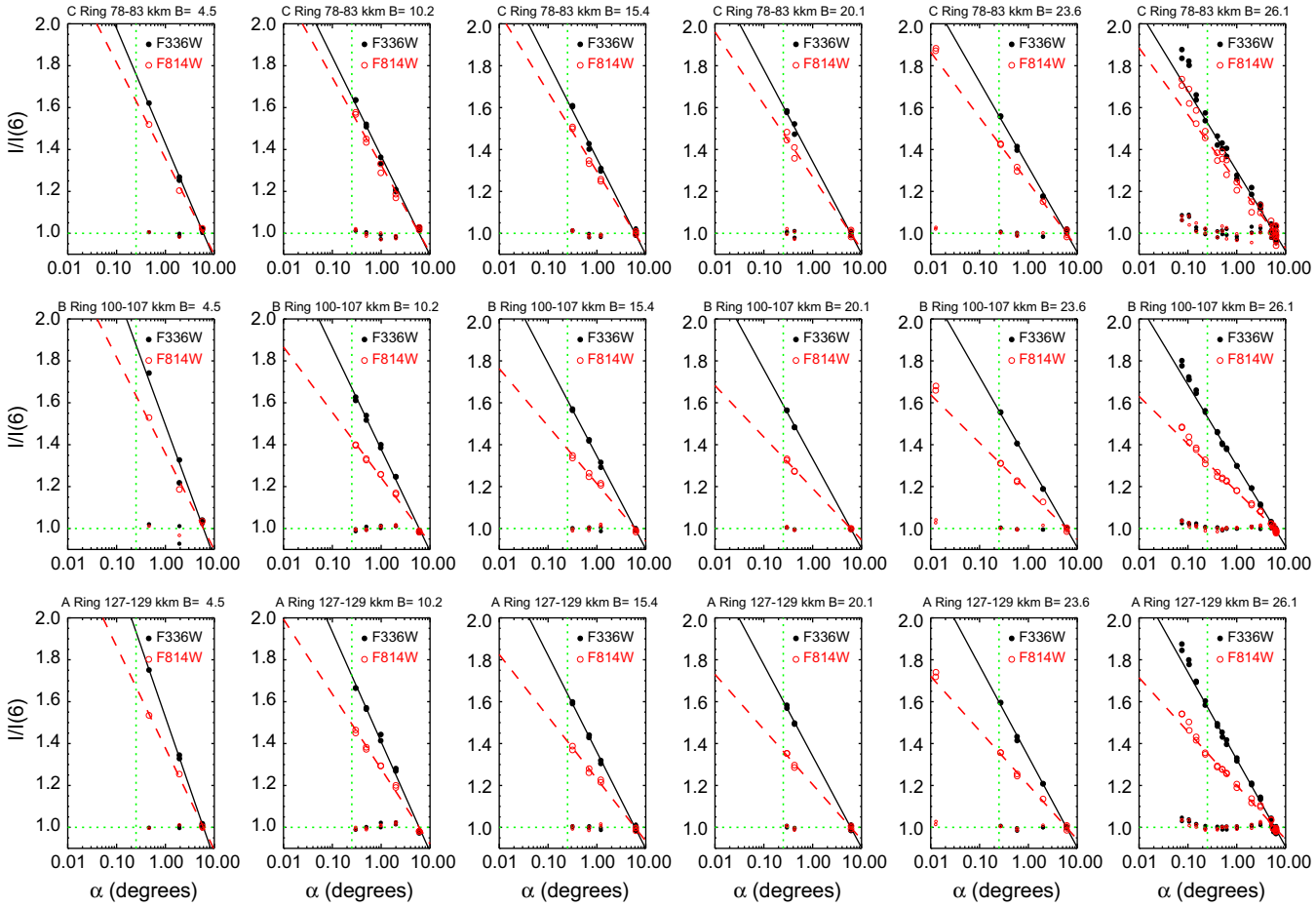

Fig. 4. Opposition phase curves of different ring regions at different elevation angles, with I/F normalized to that at $\alpha = 6°$. The C ring (upper row), the B ring (middle) and the A ring (lower) regions are the same as those studied in French et al. (2007b). From left to right the elevation angle increases from $B_{\rm eff} = 4.5°$ to 26.1°. Curves for two different filters are shown, F336W and F814W. The lines indicate log-linear fits of the form $I/F = a\ln\alpha + b$, obtained using values for $\alpha > 0.25°$. Also shown are the residuals of the fits (deviation of small symbols from unity). This fit range, excluding the near to opposition data points, was chosen in order to give a similar coverage of phase angles for all elevations: note that for $B_{\rm eff} = 23.6°$ there are additional small α measurements falling outside the fitted range.

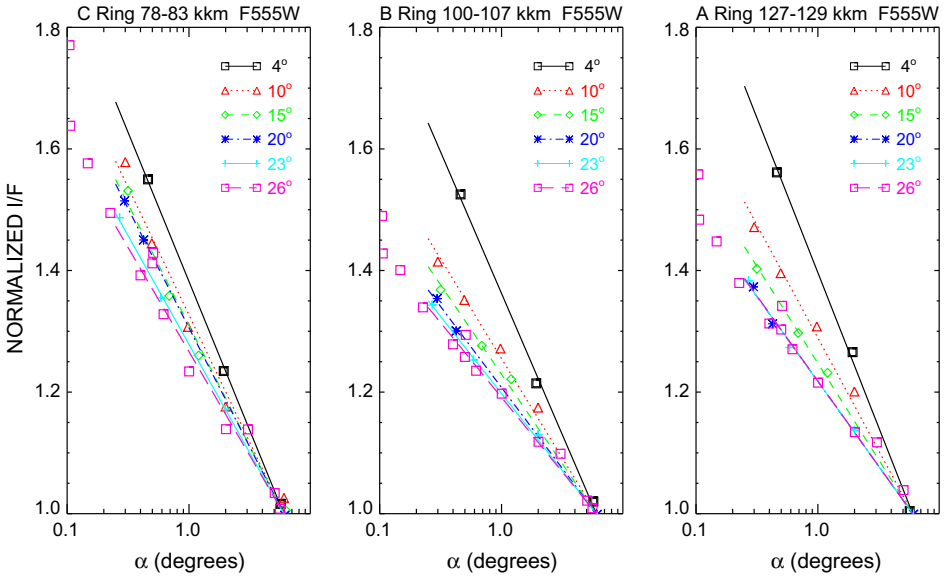

Fig. 5. Phase curves for the C, B, and A ring regions in the F555W filter, with the data from different elevation angles collected in each frame. The lines indicate the log-linear fits obtained using data values with $\alpha > 0.25°$ (same as in Fig. 4 for F336W and F814W filters).

Table 4
Log-linear fits to normalized HST phase curves.[a]

	F336W		F439W		F555W		F675W		F814W	
B_{eff}	a	b	a	b	a	b	a	b	a	b
C ring 78,000–83,000 km										
26.1	−0.0048	0.0377	−0.0060	0.0491	−0.0061	0.0521	−0.0063	0.0561	−0.0067	0.0606
23.6	−0.0055	0.0412	−0.0067	0.0529	−0.0068	0.0559	−0.0071	0.0612	−0.0071	0.0650
20.1	−0.0066	0.0461	−0.0079	0.0589	−0.0082	0.0627	−0.0086	0.0685	−0.0086	0.0725
15.4	−0.0082	0.0557	−0.0097	0.0707	−0.0100	0.0759	−0.0105	0.0829	−0.0112	0.0878
10.2	−0.0110	0.0736	−0.0127	0.0932	−0.0139	0.1015	−0.0153	0.1115	−0.0159	0.1164
4.5	−0.0182	0.1088	−0.0217	0.1348	−0.0232	0.1503	−0.0248	0.1657	−0.0257	0.1751
B ring 100,000–107,000 km										
26.1	−0.0321	0.2488	−0.0451	0.4337	−0.0501	0.5594	−0.0527	0.6317	−0.0550	0.6564
23.6	−0.0340	0.2533	−0.0460	0.4359	−0.0513	0.5568	−0.0564	0.6365	−0.0551	0.6505
20.1	−0.0352	0.2529	−0.0476	0.4345	−0.0530	0.5531	−0.0574	0.6290	−0.0577	0.6448
15.4	−0.0361	0.2524	−0.0501	0.4325	−0.0573	0.5503	−0.0599	0.6227	−0.0630	0.6406
10.2	−0.0380	0.2484	−0.0548	0.4247	−0.0611	0.5389	−0.0640	0.6101	−0.0684	0.6276
4.5	−0.0424	0.2299	−0.0624	0.3917	−0.0741	0.4993	−0.0811	0.5568	−0.0850	0.5784
A ring 127,000–129,000 km										
26.1	−0.0243	0.1781	−0.0325	0.2885	−0.0356	0.3562	−0.0363	0.3921	−0.0379	0.4076
23.6	−0.0260	0.1844	−0.0334	0.2961	−0.0361	0.3616	−0.0394	0.4034	−0.0388	0.4137
20.1	−0.0270	0.1907	−0.0344	0.3067	−0.0373	0.3740	−0.0405	0.4162	−0.0405	0.4270
15.4	−0.0299	0.2024	−0.0396	0.3248	−0.0440	0.3970	−0.0450	0.4393	−0.0474	0.4528
10.2	−0.0355	0.2193	−0.0499	0.3526	−0.0539	0.4308	−0.0568	0.4779	−0.0600	0.4937
4.5	−0.0464	0.2413	−0.0648	0.3896	−0.0749	0.4729	−0.0779	0.5183	−0.0827	0.5402

[a] a and b are the fit parameters in $\frac{I(\alpha)}{F} = a \ln \alpha + b$ (Eq. (4); phase angle α expressed in degrees, natural logarithm).

Assuming $Q_{ms} = 0$, the fractional brightness increase (denoted by OE) in some interval $\alpha_{max} \rightarrow \alpha_{min}$ can be written as

$$\begin{aligned} OE(B_{eff},\tau,\lambda) &= \frac{I(\alpha_{min},B_{eff},\tau,\lambda)}{I(\alpha_{max},B_{eff},\tau,\lambda)} \\ &\approx \frac{f_i(\alpha_{min},\lambda) f_e(\alpha_{min},B_{eff},\tau) P(\alpha_{min},\lambda)}{f_i(\alpha_{max},\lambda) f_e(\alpha_{max},B_{eff},\tau) P(\alpha_{max},\lambda)} \\ &= OE_i(\lambda) OE_e(B_{eff},\tau) \frac{P(\alpha_{min},\lambda)}{P(\alpha_{max},\lambda)}, \end{aligned} \tag{7}$$

where we have denoted $OE_i \equiv f_i(\alpha_{min})/f_i(\alpha_{max})$ and $OE_e \equiv f_e(\alpha_{min})/f_e(\alpha_{max})$. To eliminate the intrinsic brightening and the contribution from the particle phase function, we normalize OE by its value at some fixed elevation $B_{eff} = B_{norm}$. This ratio contains only the external contribution,

$$\frac{OE(B_{eff},\tau,\lambda)}{OE(B_{norm},\tau,\lambda)} = \frac{OE_e(B_{eff},\tau,\lambda)}{OE_e(B_{norm},\tau,\lambda)}, \tag{8}$$

since the interparticle shadowing contribution f_e is the only factor that depends on B_{eff}.

In Fig. 6 we show the observed brightness enhancement OE_{obs} as a function of elevation angle, for the previously defined C, B, and A ring regions. The range $\alpha_{max} = 6°$ and $\alpha_{min} = 0.5°$ is chosen, as the brightening in this range is likely to be due to the interparticle mutual shadowing effect, rather than the more narrow intrinsic opposition peak. For this range of phase angles, the log-linear fits of the previous section fits can be used with good accuracy, so that

$$OE_{obs} \equiv I(0.5°)/I(6.0°) = \frac{a \ln 0.5 + b}{a \ln 6.0 + b}, \tag{9}$$

where a and b are the fit parameters in Eq. (4). As seen in Fig. 6 (upper row; see also Table 5), the typical values of OE_{obs} for the C, B, and A ring regions are 1.25–1.4 for $B_{eff} = 26.1°$, increasing to 1.5–1.75 for $B_{eff} = 4.5°$. To show that an interparticle shadowing contribution is indeed present, the lower row in Fig. 6 shows OE_{obs} normalized to that at $B_{eff} = 26.1°$. If we assume, as in Eq. (8), that the intrinsic contribution is independent of B, the effect seen in the lower row must be due solely to the dependence of interparticle mutual shadowing on the opening angle. For the A and B ring regions the ratio $OE_{obs}(4.5°)/OE_{obs}(26.1°)$ is about 1.2, and about 1.1 for the C ring region. That we are seeing an interparticle shadowing effect is further supported by the fact that the ratio $OE_{obs}/OE_{obs}(26.1°)$ is similar for all filters, as it should be if it arises from interparticle shadowing. It also supports the assumption that multiple scattering Q_{ms} is insignificant. That is, a significant multiple scattering contribution would make the shape of the curves depend on the filter, since the particle albedo increases toward longer optical wavelengths.[4]

Similarly, to eliminate the interparticle shadowing contribution to OE we may normalize by its value at wavelength $\lambda = \lambda_{norm}$,

$$\frac{OE(B_{eff},\tau,\lambda)}{OE(B_{eff},\tau,\lambda_{norm})} = \frac{OE_i(\lambda)}{OE_i(\lambda_{norm})} \frac{P(\alpha_{min},\lambda)/P(\alpha_{min},\lambda_{norm})}{P(\alpha_{max},\lambda)/P(\alpha_{max},\lambda_{norm})}. \tag{10}$$

Here, the first multiplier describes the wavelength-dependent difference in the intrinsic opposition brightening, while the second factor describes the change in the *color* $P(\lambda)/P(\lambda_{norm})$ between α_{max} and α_{min}; these are written separately, since the color change (Cuzzi et al., 2002) might appear over a wider angular range than the narrow intrinsic brightening peak. Since the intrinsic particle behavior should not depend on opening angle, the above ratio should be independent of B_{eff}, as is also verified by HST data.

In order to determine the actual interparticle mutual shadowing contribution to the opposition brightening as a function of α, and not merely its relative contribution via $OE_{obs}/OE_{obs}(26.1°)$, we use simulation modeling in the next sub-section.

3.2. Monte Carlo simulation method

Our photometric calculations are carried out with the method developed in SK2003 and in Salo et al. (2004), based on following

[4] With the inclusion of multiple scattering, Eq. (7) is modified to $OE_{obs}(B_{eff}) = \frac{f(0.5°,B_{eff}) + Q_{ms}(B_{eff}) P(0.5°)/P(6°)}{f(6°,B_{eff}) + Q_{ms}(B_{eff})}$, where $f(\alpha,B_{eff}) \equiv f_i(\alpha,\lambda) f_e(\alpha,B_{eff},\tau)$. Assuming that $Q_{ms} \ll f$ for all B_{eff}, we may approximate $OE_{obs}(B_{eff})/OE(B_{eff}) = 1 + Q_{ms}(B_{eff})[1/f(0.5°,B_{eff}) - 1/f(6°,B_{eff})]$, where OE in the denominator includes just the singly scattered component as in Eq. (7). Assuming that $Q_{ms}(4.5°) \ll Q_{ms}(26.1°)$, we may further approximate $OE_{obs}(4.5°)/OE_{obs}(26.1°) \approx OE(4.5°)/OE(26.1°)(1 + Q_{ms}(26°)(1/f(6°,26.1°) - 1/f(0.5°,26.1°))$. Since $f(0.5°) > f(6°)$, the prefactor of Q_{ms} is positive. This implies that significant multiple scattering would make the curves in the lower row of Fig. 6 steeper in the red filter than in the blue filter, since $Q_{ms}(\text{red}) > Q_{ms}(\text{blue})$.

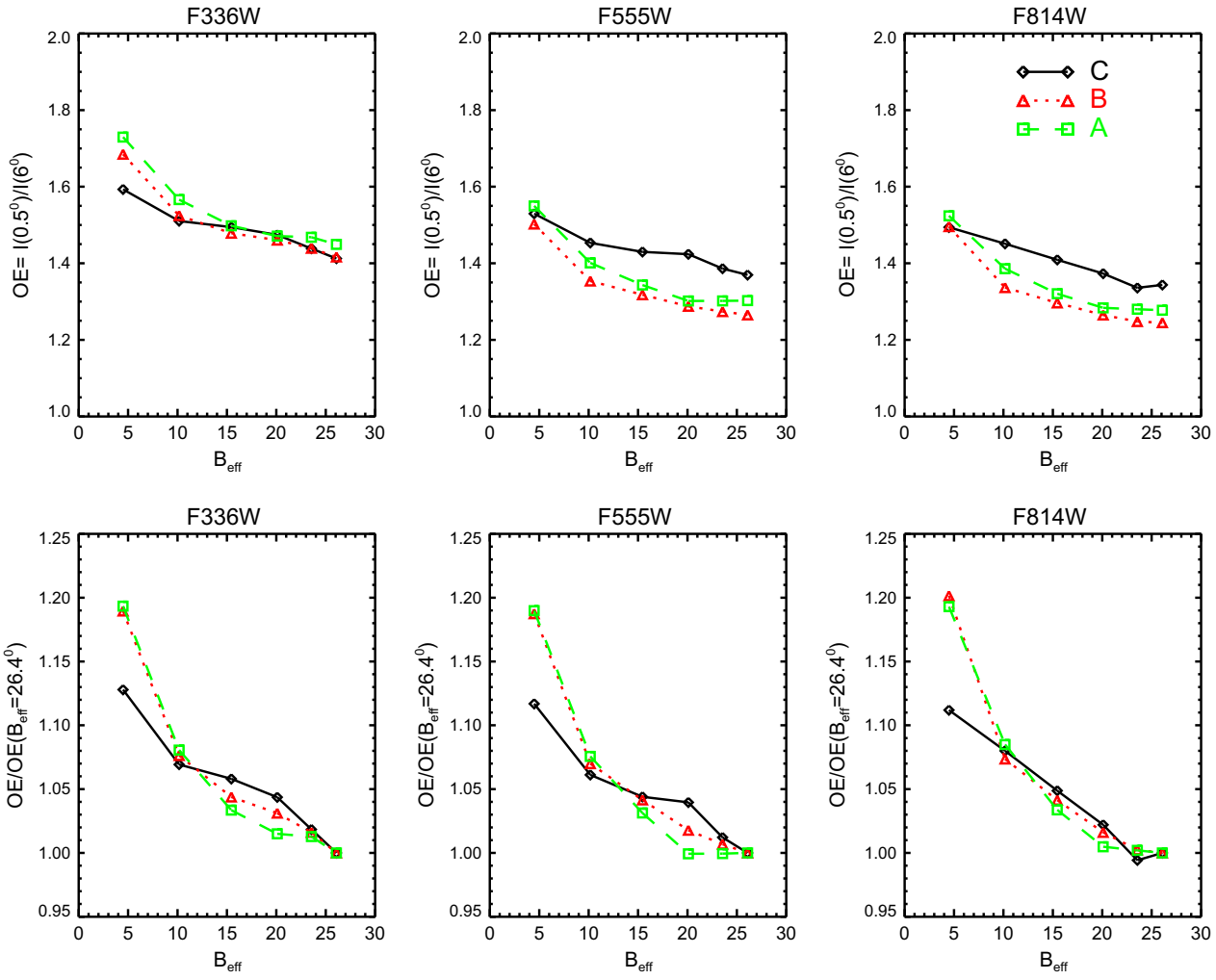

Fig. 6. The wide component of the opposition brightening measured in terms of $OE = I(0.5°)/I(6°)$, obtained from log-linear fits. The upper row shows OE as a function of $B_{\rm eff}$ for the three studied C, B, and A ring regions, for three different filters. In the lower row, OE has been normalized to that at $B_{\rm eff} = 26.1°$.

Table 5
Log-linear fits to HST phase curves: the derived parameters.[a]

	F336W		F439W		F555W		F675W		F814W	
$B_{\rm eff}$	*OE*	*I*/*F*(6°)	*OE*	*I*/*F*(6°)	*OE*	*I*/*F*(6°)	*OE*	*I*/*F*(6°)	*OE*	*I*/*F* (6°)
C ring 78,000–83,000 km										
26.1	1.4125	0.0291	1.3869	0.0384	1.3696	0.0412	1.3467	0.0449	1.3436	0.0485
23.6	1.4386	0.0313	1.4070	0.0409	1.3862	0.0437	1.3640	0.0485	1.3359	0.0523
20.1	1.4741	0.0344	1.4390	0.0448	1.4238	0.0480	1.4018	0.0531	1.3732	0.0572
15.4	1.4945	0.0410	1.4495	0.0534	1.4298	0.0580	1.4084	0.0640	1.4092	0.0678
10.2	1.5104	0.0538	1.4465	0.0705	1.4534	0.0765	1.4541	0.0840	1.4511	0.0878
4.5	1.5932	0.0762	1.5602	0.0960	1.5296	0.1088	1.5078	0.1213	1.4940	0.1291
B ring 100,000–107,000 km										
26.1	1.4164	0.1913	1.3177	0.3528	1.2652	0.4696	1.2436	0.5373	1.2449	0.5579
23.6	1.4393	0.1924	1.3238	0.3534	1.2739	0.4650	1.2619	0.5354	1.2479	0.5519
20.1	1.4606	0.1899	1.3389	0.3492	1.2877	0.4580	1.2713	0.5261	1.2650	0.5414
15.4	1.4785	0.1877	1.3628	0.3428	1.3178	0.4477	1.2886	0.5154	1.2964	0.5278
10.2	1.5245	0.1802	1.4175	0.3264	1.3537	0.4294	1.3211	0.4954	1.3365	0.5051
4.5	1.6849	0.1539	1.5543	0.2799	1.5024	0.3665	1.4900	0.4114	1.4958	0.4261
A ring 127,000–129,000 km										
26.1	1.4494	0.1345	1.3504	0.2303	1.3025	0.2924	1.2760	0.3271	1.2775	0.3397
23.6	1.4680	0.1379	1.3515	0.2362	1.3018	0.2970	1.2946	0.3327	1.2800	0.3442
20.1	1.4711	0.1423	1.3483	0.2452	1.3016	0.3072	1.2925	0.3438	1.2836	0.3545
15.4	1.4980	0.1490	1.3874	0.2539	1.3433	0.3182	1.3115	0.3587	1.3206	0.3678
10.2	1.5663	0.1557	1.4712	0.2632	1.4010	0.3342	1.3750	0.3762	1.3860	0.3862
4.5	1.7297	0.1581	1.5885	0.2735	1.5498	0.3387	1.5114	0.3787	1.5240	0.3921

[a] $OE \equiv I(\alpha = 0.5°)/I(\alpha = 6.0°)$.

a large number of photons through a ring composed of discrete finite-sized particles. The particle fields we use to model the rings are obtained from dynamical simulation models. The particles are assumed to be much larger than the wavelength so that geometric ray tracing can be used. The particle field, with periodic planar boundaries, is illuminated by a parallel beam of photons, and the path of each individual photon is followed in detail from one intersection with a particle surface to the next scattering, until the photon escapes the particle field; the new direction after each scattering is obtained via Monte Carlo sampling of the particle phase function (see e.g. Plass and Kattawar, 1968; Salo, 1988). The brightness at a chosen observing direction is obtained by adding together the contributions of all individual scatterings that are visible from this direction (not blocked by any of the finite-sized particles). Compared to direct Monte Carlo estimates based on tabulating just the directions of escaped photons, this indirect method gives significantly reduced variance of the results (see Fig. 5 in SK2003).

Since we are dealing with low elevation angle observations, the periodic boundaries must be treated very accurately, as described in detail in SK2003. To reduce the effect of the discreteness of the simulated particle fields, results from at least five separate particle snapshots are combined in the phase curves. Also, the particle fields are randomly rotated between successive photons to avoid the possibility that, for example, a single large particle separated from the main particle field could dominate the results. This rotation is allowed when particle fields that are homogeneous in the planar directions are used. In contrast, in the self-gravitating examples, the correct direction of viewing/illumination with respect to gravity wakes must be maintained, in which case a larger number of simulation snapshots (40) is averaged in order to reduce noise. Finally, since our main interest is in the opposition effect, which represents a deviation from the classical zero volume case, it is important that our method can reproduce very accurately the classical results in the asymptotic limit $D \to 0$ (see Fig. 4 in SK2003).

In the current study, two different particle phase functions are used: the Lambert law

$$P_L(\alpha) = \frac{8}{3\pi}[\sin\alpha + (\pi - \alpha)\cos\alpha], \tag{11}$$

and a power-law phase function

$$P_{\text{power}}(\alpha) = c_n(\pi - \alpha)^{n_s}, \tag{12}$$

where c_n is a normalization constant $\left(\int_{4\pi} P(\alpha)d\Omega = 1\right)$. For $n_s = 3.09$, the latter formula gives a good match to the phase function of Callisto (Dones et al., 1993). In the case of Lambert scattering, we utilize the fact that the above given *spherical-particle* phase function (van de Hulst, 1980) follows from a very simple *surface-element* scattering law $S_L(\cos e, \cos i) = \cos e/\pi$, where e and i measure the emergence and incidence angles with respect to the surface element's normal vector (this formula means that the brightness of the Lambert surface element, $I = \pi F \cos i S_L/\cos e = F\cos i$, is independent of viewing angle, being just proportional to the incoming flux). Thus, in each scattering we sample from the distribution S_L to obtain the new photon direction with respect to the normal vector of the local surface element (see SK2003 for details). The advantage of using surface-element scattering is that the location of scatterings on the particle surface is correctly sampled, which is crucial for accurate calculation of mutual interparticle shadowing effects. On the other hand, when using the power-law phase function, we sample from Eq. (12) the new direction with respect to the direction of the incoming photon. Since the particles have a finite size, this necessarily involves an approximation as compared to using a proper surface element law. In SK2003 the Lambert surface-element scattering law and the Lambert spherical-particle phase function treatments were compared in detail (see their Fig. 10), and it was shown that both treatments give very similar results, provided that the scattering location at the particle surface is accurately sampled, so that the emerging photon is continued from the point of scattering (instead of continuing from the particle center, which would be conceptually more in accordance with the use of spherical particle scattering law — this alternative would, however, significantly reduce the opposition brightening).

In the current study we use Lambert surface-element scattering whenever we want accurate estimates of the interparticle shadowing, i.e the function $f_e(\alpha, B_{\text{eff}}, \tau)$ (the spherical-particle treatment would also be sufficiently accurate near opposition, provided that the photon path is continued from the intersection point). The power-law phase function is mainly used in Section 5, where we calculate the contribution of multiple scattering, and want to compare the Lambert and power-law phase functions. Although the amount of multiple scattering itself, I_{ms}, for a given Bond albedo A, is not strongly dependent on the phase function, the fractional contribution $I_{ms}/(I_{ss} + I_{ms})$ will depend on A, as a different A is needed for a given phase function model to match the low α observations dominated by I_{ss}. For example, the ring brightness observed in F555W filter can be matched with the standard $n_s = 3.09$ power-law phase function if $A \sim 0.4$ is adopted. Since the Lambert phase function is less backscattering than this power-law phase function, a larger $A \sim 0.7$ is needed to obtain a similar low α brightness. As a consequence, the role of multiple scattering will be more important in models using the Lambert phase function.

The principal difference between our approach and the Porco et al. (2008) ray tracing method is that we include scatterings to an arbitrary order. Additionally, our method uses Monte Carlo sampling of the particle phase function (either the surface element law, or the spherical particle model), so that after each scattering event a single emerging photon is followed. The computational burden is thus *at most* equally divided between each scattering order (in practice, the few first orders dominate as the photon paths are terminated when they leave the particle layer). On the other hand, in Porco et al. (2008) each successive scattering is represented by a bundle of emerging photons, chosen according to a discretized phase function. This implies that each successive scattering order requires more and more computations (until they become computationally prohibitive; in practice Porco et al. (2008) usually treat orders only up to 4), although their contribution to the final result gets rapidly smaller. Our Monte Carlo approach will lead to identical results, but with a significantly reduced statistical variance for a given computational effort. The improved efficiency of our method might be quite significant in some applications, in particular when dealing with cases where multiple scattering is more important (transmitted radiation, high phase angles, high particle albedo) than in the current topic of opposition brightening, which is dominated by first-order scattering.

3.3. Grid of dynamical and photometric simulation models

We study the effect of ring structure on the expected interparticle mutual shadowing by performing simulations with different dynamical optical depths ($\tau_{\text{dyn}} = 0.1$–2.0) and particle size distributions, assumed to follow a power law distribution

$$dN/dR \propto R^{-q}, \quad R_{\min} < R < R_{\max}, \quad q = 3, \tag{13}$$

with the ratio $R_{\min}/R_{\max} = 0.02$–0.2. In all models the maximum radius $R_{\max} = 5$ m. For the elasticity of particles the Bridges et al. (1984) velocity-dependent coefficient of restitution is assumed

$$\epsilon_n(v_n) = \min[(v_n/v_c)^{-0.234}, 1], \tag{14}$$

where v_n is the normal component of the relative velocity of the impacting bodies and the scale parameter v_c equals

$v_B = 0.0077$ cm s^{-1} in Bridges et al.'s measurements. The simulations are performed for the Saturnocentric distance $a = 100{,}000$ km, with $\Omega = 1.94 \times 10^{-4}$ s^{-1}. Also, to keep the models simple, self-gravity is not included in these simulations (it is studied separately in Section 5 below). The dynamical simulations are performed with the local code, using the periodic boundary conditions introduced by Wisdom and Tremaine (1988) and Toomre and Kalnajs (1991); for more details of the code see Salo (1995) and Salo et al. (2001). These models are then illuminated/viewed from the elevation angles $B = 4$–$26°$ and the phase angle is varied between 0° and 90°. Compared to SK2003, where several examples of opposition brightening were given, and compared to theoretical treatments of Lumme and Bowell (1981) and Hapke (1986), we now cover a larger range of optical depths and viewing elevations in a systematic manner, chosen to correspond to the range of HST observations. Also a larger range of α is explored, with future applications to spacecraft observations in mind (see Section 6).

Note that the simulation models are defined in terms of the dynamical (geometric) optical depth, i.e. the total fractional area of particles. As discussed in SK2003, in general $\tau_{\rm dyn}$ differs from photometric optical depth $\tau_{\rm phot}$, defined in terms of the probability p for a light ray passing through the layer in the perpendicular direction, $p = \exp(-\tau_{\rm phot})$. However, at the classical limit $D = 0$ we have $\tau_{\rm dyn} = \tau_{\rm phot}$, so that when referring to the theoretical I_{ss} in Eq. (6) we make no distinction between dynamical and photometric optical depths, and leave out the subscript from τ.

Fig. 7 displays examples of calculated interparticle shadowing curves, in terms of $f_e = I_{ss}/I_{ss}(D = 0)$. It is immediately evident that the mutual interparticle shadowing opposition effect, measured as a deviation from the classical single scattering result, may extend to several tens of degrees.[5] The maximum amplitude $f_e(\alpha = 0°)$ is practically independent of the adopted size distribution and approaches the theoretical maximum $f_e = 2$ (Irvine, 1966) when the path optical depth $\tau_{\rm path} = \tau_{\rm phot}/\mu + \tau_{\rm phot}/\mu' = 2\tau_{\rm phot}/\mu_{\rm eff}$ is large. Also, $f_e(0°)$ is reduced for smaller $\tau_{\rm path}$, regardless of the assumed particle size distribution: the maximum amplitude is in good agreement with the theoretical estimate (SK2003)

$$f_e(0°) = \frac{2}{1+\exp(-\tau_{\rm path}/2)} \approx 1 + \frac{1}{4}\tau_{\rm path} - 0\left(\tau_{\rm path}^3\right)\ldots, \tag{15}$$

which follows from the theoretical treatment of Lumme and Bowell (1981). In Fig. 7 this estimate is marked with a horizontal line. Also shown in the upper right corner of the frames is the photometric optical depth, which in dense homogeneous systems exceeds $\tau_{\rm dyn}$ by a factor $\sim(1 + D)$ (SK2003; see also Peltoniemi and Lumme, 1992). Notice that Eq. (15) implies a similar dependence on $\tau_{\rm path}$, regardless of which combination of $\tau_{\rm phot}$ and $B_{\rm eff}$ produces it (see Fig. 13 in SK2003 for detailed comparison for homogeneous systems; their $E_{\max}$ corresponds to $f_e(0°)$).

Also shown in Fig. 7 are fits to the simulated shadowing curves, using the Hapke (1986, 2002) formula for the single scattering brightness enhancement due to SH in a semi-infinite particle layer,

$$B_{\rm SH}(\alpha) = 1 + \frac{B_{s0}}{1 + \frac{\tan(\alpha/2)}{h_s}}. \tag{16}$$

Here, B_{s0} is the fractional amplitude, and h_s describes the width of the effect. The fits, indicated by solid curves in Fig. 7 use Monte Carlo results for $\alpha < 10°$. Very good agreement is seen (the mean RMS deviation is 0.01), except for the simulations with the widest size distribution, in which case the fit range extends furthest away from the peak of the function (note that the Hapke SH formula implies $B_{\rm SH}(\alpha) \to 1$ for large α, whereas Monte Carlo simulations indicate $f_e > 1$). Similarly, the Monte Carlo curves are well fitted with the 4-parameter linear-exponential formula, yielding a mean RMS ~ 0.005.

As seen in Fig. 7, the angular width of the simulated interparticle shadowing opposition peak depends strongly on the adopted size distribution, and most importantly, also on the elevation angle. On the other hand, it is nearly independent of $\tau_{\rm dyn}$. Fig. 8 shows the HWHM of the interparticle shadowing enhancement factor, both as obtained directly from $f_e(\alpha)$ curves (in the left), by setting

$$f_e(\alpha = {\rm HWHM}) - 1 = \frac{1}{2}[f_e(\alpha = 0°) - 1], \tag{17}$$

and from the Hapke SH model (HWHM $\approx 2h_s$), as well as from the linear-exponential model fits to the simulation curves. For the Hapke model fits the HWHM's are close to the actual simulation values, whereas for the linear-exponential fits the HWHM's are roughly 2–3 times smaller: the discrepancy is due to the fact that the HWHM for the linear-exponential fit is calculated from the exponential part, although a large part of the fit is due to the linear slope.

The fact that the widest size distribution has the narrowest opposition peak, is consistent with the Hapke (1986) theoretical model for semi-infinite particle layers. According to his formulae,

$$\frac{\rm HWHM}{D(\tau_s = 1)} = \frac{3}{4}\frac{\langle\sigma\rangle\langle R\rangle}{\langle V\rangle} = \frac{3}{4}\frac{\langle R^2\rangle^{1.5}}{\langle R^3\rangle} = \frac{3}{4}Y, \tag{18}$$

where $D(\tau_s = 1)$ is the volume density at the layer where the slant optical depth equals unity, $\langle\sigma\rangle$ and $\langle V\rangle$ are the average scattering cross section and particle volume, and $\langle R\rangle = \sqrt{\langle\sigma\rangle/\pi}$. For a $q = 3$ power law size distribution the Hapke function Y is

$$Y = \frac{\sqrt{2}(\ln W_s)^{1.5} W_s}{(W_s - 1)\left(W_s^2 - 1\right)^{0.5}}, \tag{19}$$

where $W_s = R_{\max}/R_{\min}$. Applied to our size distributions, and using the central plane volume filling factors ($D(z = 0) = 0.32$–0.38) for $D(\tau_s = 1)$, this predicts that HWHM = 3–12°, for $W_s = 50$–5, respectively. In addition to predicting correctly the relative change in HWHM, these width estimates are quite close to the results of the calculations for $B = 26°$, suggesting that for this elevation the reflection is indeed from the dense equatorial layer. On the other hand, for lower elevations the reflection is actually from the upper layers with a substantially smaller effective D (see Fig. 1 for a schematic illustration). According to Fig. 9 in SK2003, for the dynamical simulations studied here, the filling factor at a given vertical coordinate z_0 (on the side of illumination/viewing) is roughly proportional to the path optical depth for a perpendicular illumination reaching this layer,

$$D(z_0) \propto \tau_{\rm phot}(z > z_0). \tag{20}$$

Since for an oblique view $\tau_s = \tau_{\rm phot}/\sin B$, setting $\tau_s \approx 1$ corresponds to reflection from the level z_0 where $\tau_{\rm phot}(z > z_0) \approx \sin B$, at which elevation the volume density $D(z_0) \approx \sin B \times D(z = 0)$. This explains the practically linear dependence,

$${\rm HWHM} \propto B, \tag{21}$$

coming in addition to the size distribution dependence implied by the Hapke (1986) formula. Note that for a vertically uniform ring, the expected width would be independent of $B_{\rm eff}$, regardless of size distribution.

Fig. 9 shows the enhancement factors $f_e(0.5°)$ and $f_e(6°)$, which mark the range of phase angles for which the simulated and observed opposition enhancements will be compared in the next

[5] In fact, the reflected I_{ss} is enhanced for any phase angle: see SK2003. Fig. 7 and the discussion related to it, and Fig. 22 below. This enhancement follows, since for a geometrically thin layer the illuminated upper layers are preferentially visible at every lit side geometry.

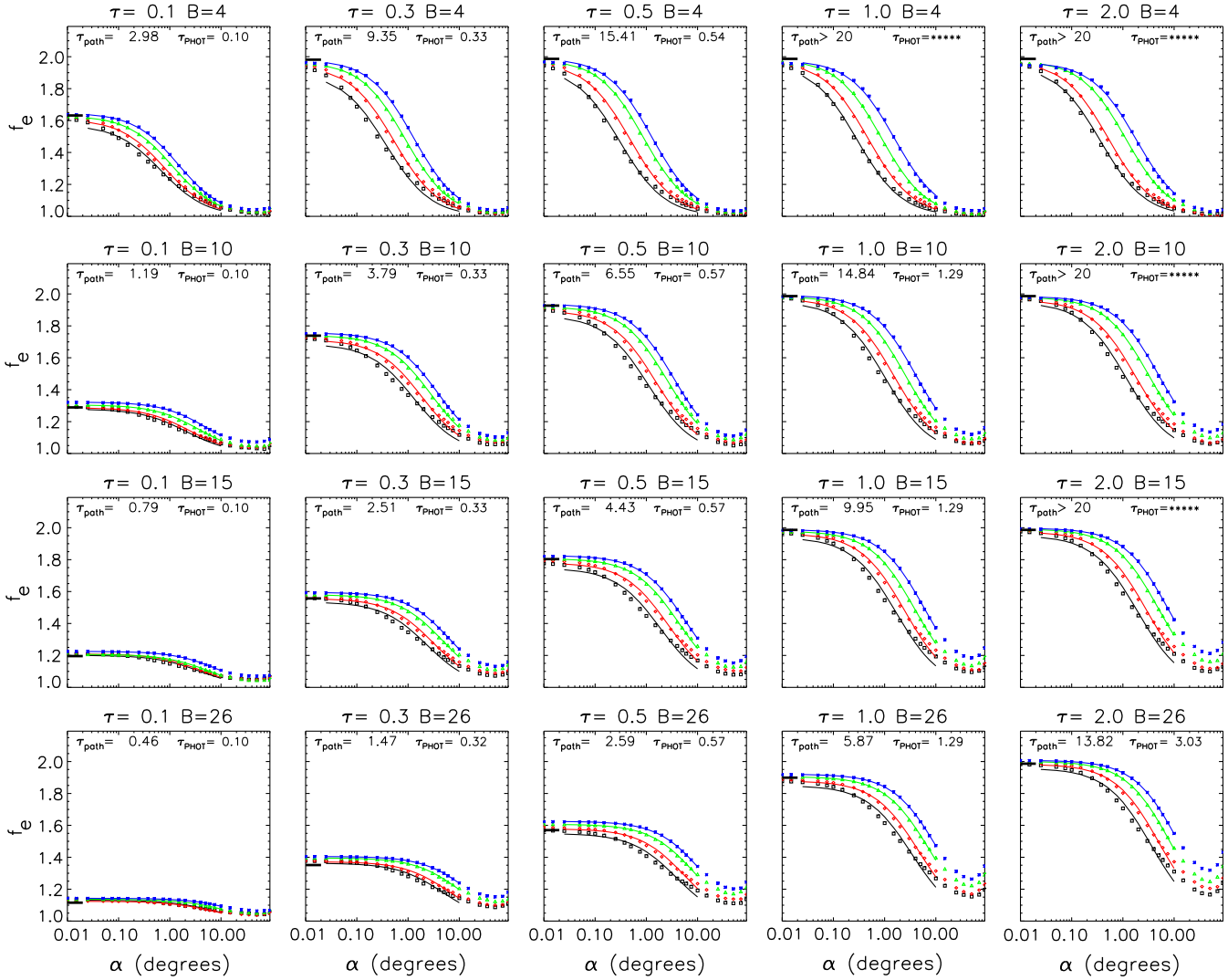

Fig. 7. Grid of dynamical and photometric simulation models performed with different optical depths and widths of particle size distributions. The interparticle shadowing enhancement of the single scattering, $f_e = I_{ss}/I_{ss}(D = 0)$, is plotted as a function of phase angle α; here $I_{ss}(D = 0)$ is the theoretical single scattering intensity for classical zero volume density ring, whereas I_{ss} is the simulated value including the shadowing effects between finite-sized particles. The simulation results are indicated by symbols, while the solid curves indicate Hapke (2002) SH fits to them. The dynamical simulations use the Bridges et al. (1984) elasticity law, and a power law size distribution $dN/dR = R^{-q}$, with $q = 3$ and $R_{max} = 5$ m; the minimum size is $R_{min} = 0.1$–1.0 m. Simulations performed with dynamical optical depths $\tau_{dyn} = 0.1$–2.0 are shown. Self-gravity is not included, and thus the systems remain homogeneous in all planar directions. Photometric Monte Carlo calculations are performed for elevations $B = B_{eff} = 4°$, 10°, 15°, 26°, using a Lambert surface-element scattering law. The numbers in the frames indicate the path optical depth $\tau_{path} = -\ln p$, where p is the probability of a photon to pass through the particle layer, and the calculated normal optical depth $\tau = \tau_{path} \sin B$.

section. Two optical depths ($\tau_{dyn} = 0.1$ and 1.5) are compared: note that although for the small τ_{dyn} the f_e's are much smaller, the ratio $OE_e = f_e(0.5°)/f_e(6°)$ (right hand panel) can still be fairly large for low elevations, at least qualitatively consistent with Fig. 7 showing significant elevation angle dependence of OE_{obs} even for the C ring. For the larger optical depths, the enhancement factors, as well as their ratio, are typically larger: however, the ratio $OE_e = f_e(0.5°)/f_e(6°)$ depends in a quite complicated way on the width of the assumed distribution and the elevation angle. Essentially, this is due to the fact that for the wide distributions, the width of the opposition peak sweeps through the range $\alpha = 0.5$–$6.0°$ when B decreases.

Finally, Fig. 10 shows examples of opposition brightening for different optical depths and elevations, both with and without the inclusion of multiple scattering. Instead of normalizing to the theoretical single scattering values as in the previous figures, the figure shows $I/I(6°)$. In this figure, the $n_s = 3.09$ power-law phase function with $A = 0.5$ was used. The small difference between the total intensity curves and those for single scattering again underlines that, at least for these phase functions, multiple scattering has only a minor role on the near-opposition phase curves. In Section 5, we show that this conclusion is also supported by the tilt-effect observations.

4. Extracting the elevation angle dependent component via model comparisons

4.1. Separating intrinsic and intra-particle contributions

From the analysis presented in Section 3.2, we have not yet determined the absolute contributions of intrinsic (f_i) and interparticle (f_e) contributions to the near-opposition brightness increase. Rather, we have identified the amount of $OE_e(B_{eff})$ relative to $B_{eff} = B_{norm}$, or the relative amount of $OE_i(\lambda)$ relative to $\lambda = \lambda_{norm}$, respectively (here, $OE_e \equiv f_e(\alpha_{min})/f_e(\alpha_{max})$ and $OE_i \equiv f_i(\alpha_{min})/f_i(\alpha_{max})$). In order to estimate the interparticle shadowing enhancement factor $f_e(\alpha, B_{eff})$ we utilize simulation modeling: we compare the observed $OE_{obs}(B_{eff})/OE_{obs}(B_{norm})$ (using $\alpha_{min} = 0.5°$, $\alpha_{max} = 6°$, $B_{norm} = 20°$) to the $OE_e(B_{eff})/OE_e(B_{norm})$ ratios indicated

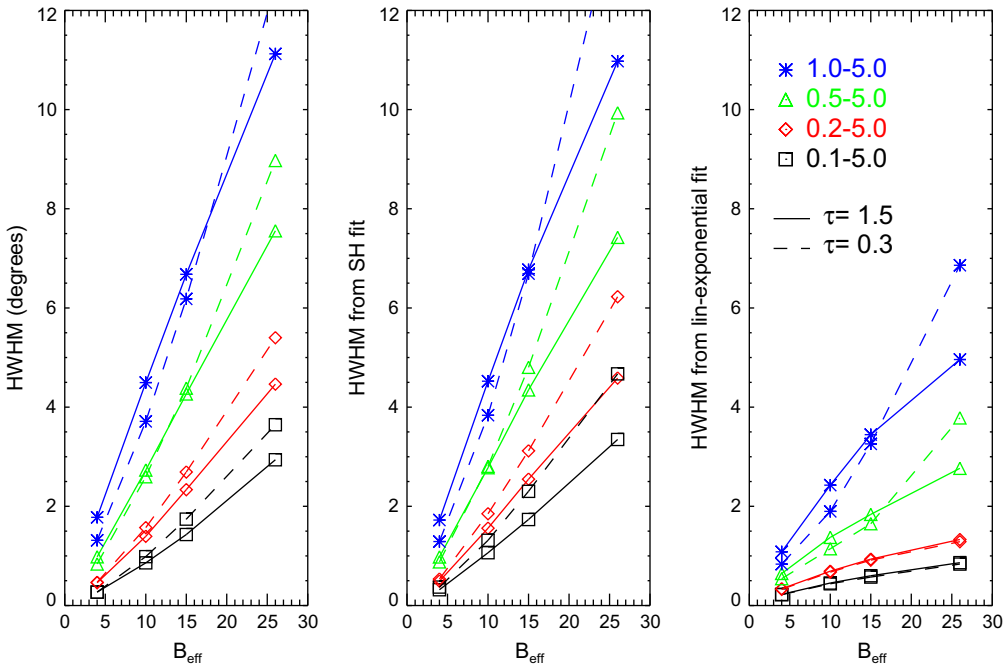

Fig. 8. The half-width half-maximum (HWHM) for the interparticle shadowing effect in the single scattered component $f_e = I_{ss}/I_{ss}(D = 0)$, obtained directly from the simulated $f_e(\alpha)$ curves (left), from Hapke SH fits (middle), and from linear-exponential fits (right) to some of the simulations displayed in Fig. 7.

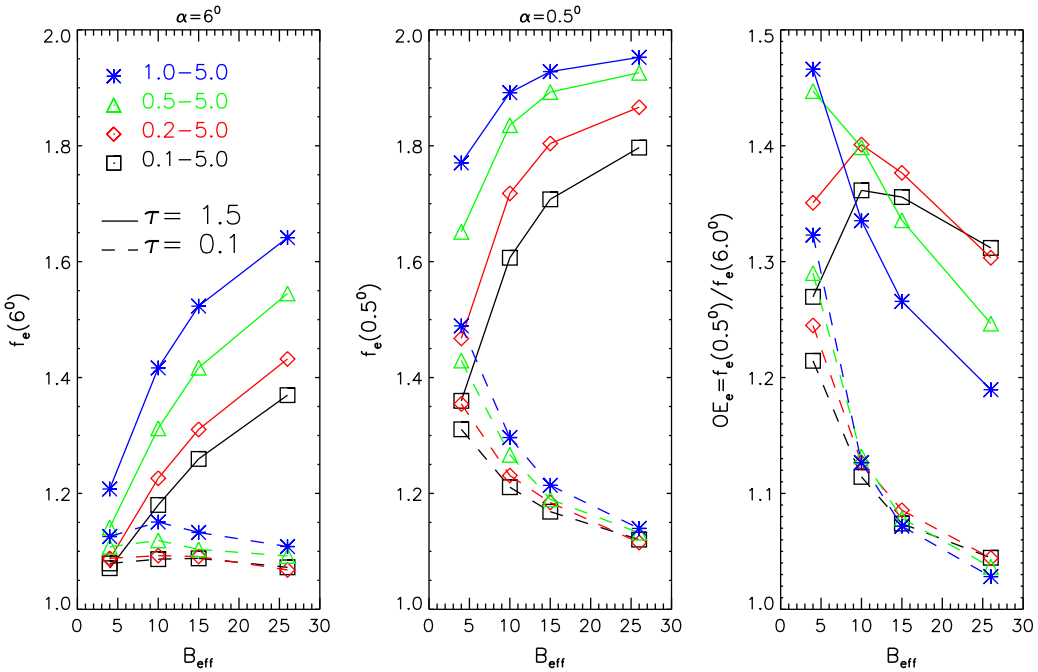

Fig. 9. The interparticle shadowing enhancement of the single scattering, $f_e = I_{ss}/I_{ss}(D = 0)$ evaluated at $\alpha = 6°$ (left) and $\alpha = 0.5°$ (middle). At the right, the ratio $OE_e = f_e(0.5°)/f_e(6°)$ is shown.

by the above described simulations performed for different optical depths and widths of the size distribution.

The best match simulation then implies a particular f_e, and the intrinsic contribution can be estimated from Eq. (5) (ignoring the Q_{ms} term):

$$f_i(\alpha,\lambda) = \frac{I_{\rm obs}(\alpha, B_{\rm eff}, \tau, \lambda)}{I_{ss}(\alpha, B_{\rm eff}, \tau, \lambda)} \frac{1}{f_e(\alpha, B_{\rm eff}, \tau)}, \tag{22}$$

where I_{ss} is the theoretical singly scattered intensity for $D = 0$. Note that there is still some freedom here, since the I_{ss} contains the product $AP(\alpha)$, which, as being independent of $B_{\rm eff}$ cannot be separated from f_i. In practice we will divide the observations with the simulated interparticle shadowing contribution and determine the ratio

$$g_i(\alpha) \equiv \frac{f_i(\alpha)P(\alpha)}{f_i(6°)P(6°)} = \frac{I_{\rm obs}(\alpha)}{I_{\rm obs}(6°)} : \frac{f_e(\alpha)}{f_e(6°)}. \tag{23}$$

The normalized intrinsic effect $g_i(\alpha)$ in the left side is also a quite good approximation for $f_i(\alpha)$ itself. That is, since the intrinsic opposition effect has HWHM < 1°, we have $f_i(6°) \approx 1$. Also, the variation in the phase function between $\alpha = 0°$ and 6° is most likely

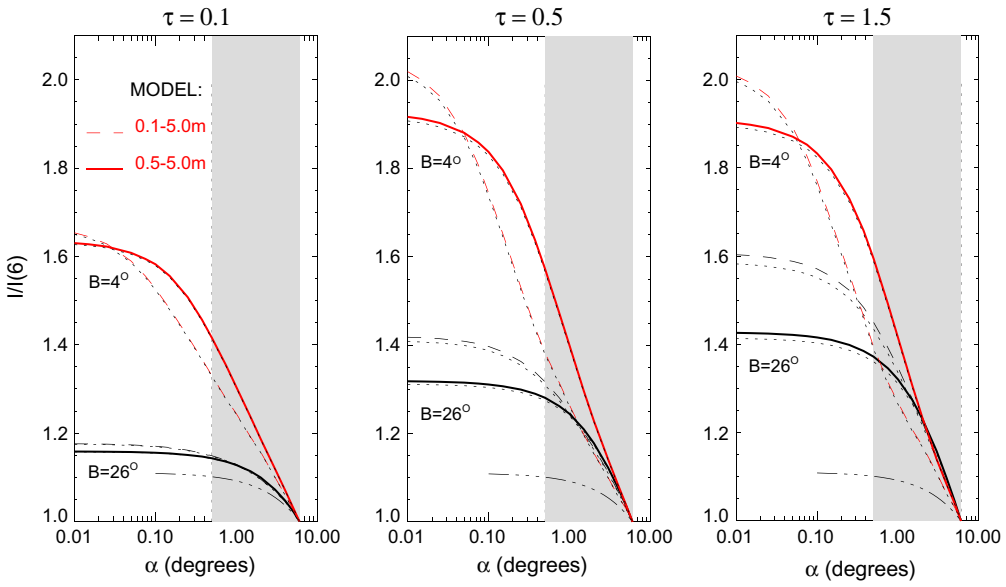

Fig. 10. Opposition phase curves in selected simulation models, including the multiply-scattered contribution: solid and dashed lines indicate the single scattered intensity normalized to $\alpha = 6°$, while dotted lines indicate the same for the total singly + multiply-scattered radiation. The $n_s = 3.09$ power-law phase function is used, with Bond albedo 0.5; the gray dash-dotted curve indicates the contribution from the power-law phase function alone, amounting to about 1.11 for the interval $\alpha = 0$–$6°$. The shaded region indicates the range $\alpha = 0.5$–$6°$ used in the comparison of simulated and observed intensities in Section 4.

very small ($P(0°)/P(6°) = 1.005$ and 1.11 for the Lambert and the $n = 3.09$ power-law phase functions, respectively). As a useful check of the extraction procedure, we can use the fact that observations at all elevation angles should yield the same $g_i(\alpha)$.

Fig. 11 shows this procedure applied to the C, B, A ring regions. In the left panels, the OE_{obs} in the U (F336W) and I (F814W) filters is compared to simulations performed with various widths of the size distribution, while in the right panels, both observations and simulations have been normalized to the OE at $B_{norm} = 20°$. In the left hand panels the observed OE's are clearly larger than the simulated ones, which contain just the interparticle shadowing contribution: the excess is due to the intrinsic opposition effect. Also, the OE in U is clearly larger than in the I filter. However, at right, after normalization to $B_{norm} = 20°$, the observed and simulated elevation angle trends are much closer to each other. Also note how well the normalization removes the wavelength dependence of the observations in the right panels, with the U and I filters behaving in a very similar manner.

For the C ring (upper row in Fig. 11) a detailed comparison is made to simulations with $\tau_{dyn} = 0.1$, in which case the magnitude of the elevation angle dependent OE increases monotonically with the width of the size distribution. Clearly, the best match to the elevation angle dependent part is obtained with the widest studied distribution $W_s = 50$; the curves also suggest that a still larger W_s would further improve the fit. On the other hand, the B ring (middle row) is compared to simulations with $\tau_{dyn} = 2.0$, and now the match is best for a much narrower size distribution $W_s = 5$–10. The main difference in the simulated $OE_e(B_{eff})/OE_e(B_{norm} = 20°)$ curves for small and large τ_{dyn}'s is the turning down at low B_{eff} values in the case of large τ_{dyn} and large W_s. As mentioned earlier, the reason is that in this case the width of the interparticle shadowing peak is so small that it falls inside the studied α range. For the A ring region (lower row) the comparison is made to simulations with $\tau_{dyn} = 1$, and just as for the B ring region, a quite narrow size distribution $W_s \sim 5$ is preferred. Interestingly, for the A ring the $\tau_{dyn} = 1$ (or even $\tau_{dyn} = 2$) case provides a slightly better match than that with the nominal $\tau_{dyn} = 0.5$, although the difference is not large. This is not surprising, taking into account that the mid-A ring is the location where self-gravity wakes are strongest: the actual amount of light reflection must result from a superposition of dense wakes and rarefied gaps, with the wakes having much higher optical depth than the nominal $\tau \sim 0.5$ (Colwell et al., 2006; Hedman et al., 2007). The fact that we are comparing the A ring to non-gravitational simulations in the first place might seem suspect. However, French et al. (2007b) showed that there is very little difference in the phase curve between wake and non-wake simulations.

In order to demonstrate that the above extraction procedure works as intended, Fig. 12 compares the original HST F336W phase curves (left panels) with those after the removal of the elevation angle dependent part (middle). All the curves are shown normalized to $\alpha = 6°$. Clearly, the residual curves in the middle panel, $g_i(\alpha) = f_i(\alpha)\ P(\alpha)/[f_i(6°)P(6°)]$, are all very close to each other, indicating that the removal of the elevation dependent part has been successful (similarly for the other filters; see Fig. 13). The removed interparticle shadowing contributions themselves, $f_e(\alpha)/f_e(6°)$, for the various B_{eff}'s are also shown (right panels).

4.2. Fitting the intrinsic component

Once the elevation angle dependent part of the opposition effect has been removed, it is interesting to make model fits to the residual curves, which presumably represent the true intrinsic opposition effect. In this sub-section, the fit parameters are given for both linear-exponential and Hapke (2002) models. We also compare our results to French et al. (2007b), to see how much the deduced intrinsic parameters differ from those obtained from fits to original high elevation angle data points, where the effect of interparticle shadowing is least pronounced.

Fig. 13 shows the deduced residual intrinsic components (large symbols), together with model fits (thick blue curves), for all five different filters. These data, collecting the observations from all elevations, are also compared with the original high elevation angle data ($B_{eff} \sim 23°$; indicated by small symbols and thin orange curves[6]): since from these latter points the interparticle shadowing contribution has not been removed, the ratio between the data sets measures the amount of interparticle shadowing correction for $B_{eff} = 23°$.

[6] The $B_{eff} = 26°$ data are also included, after they have been corrected to correspond to $B_{eff} = 23°$, by first dividing by $f_e(26°)I_{ss}(26°)$ and then multiplying by $f_e(23°)I_{ss}(23°)$.

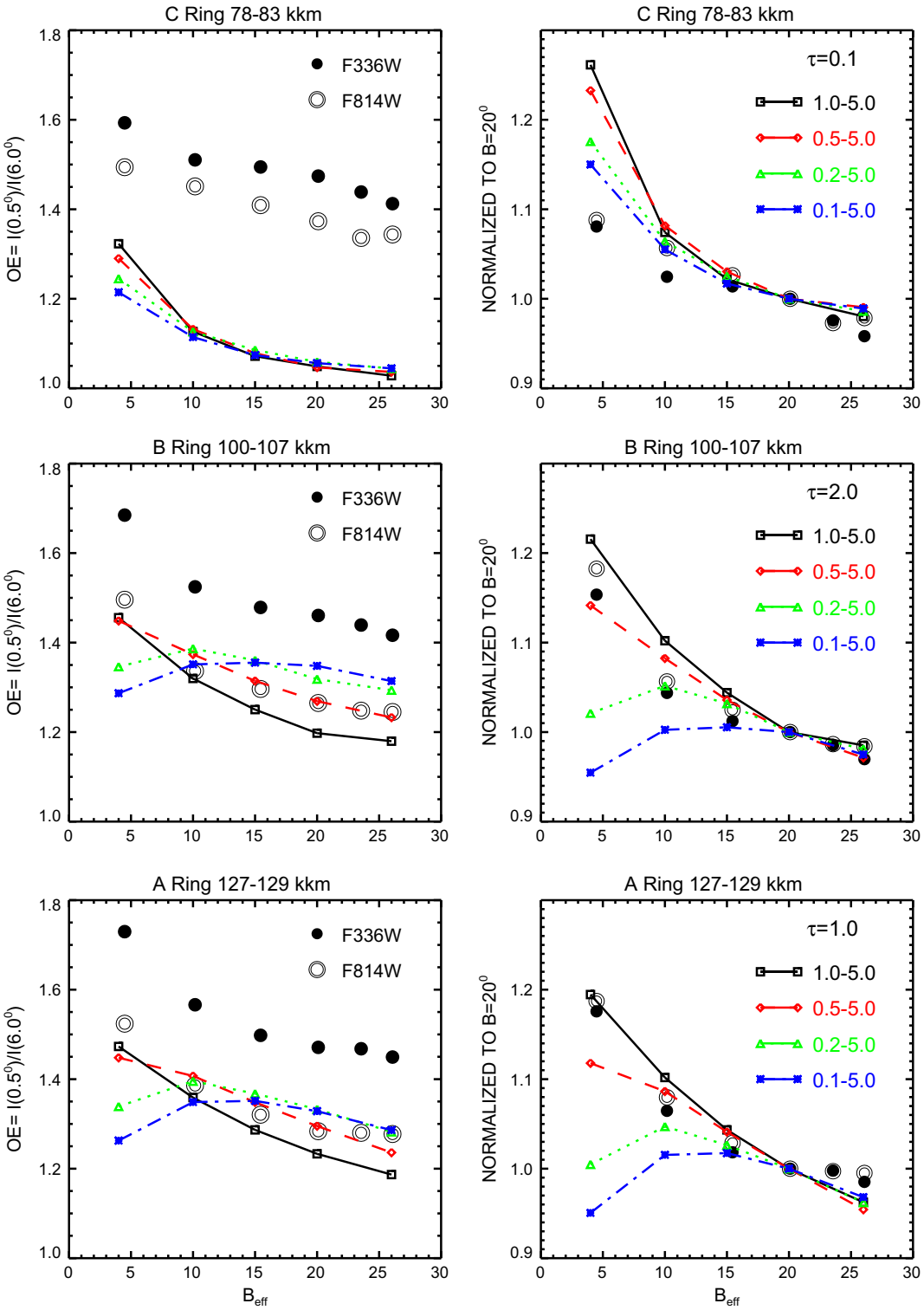

Fig. 11. The left panels show the extended opposition effect as a function of $B_{\rm eff}$, measured by $OE = I(\alpha = 0.5°)/I(\alpha = 6°)$, for the three different ring regions: solid and open symbols stand for observations in the F336W and F814W filters, respectively. The right panels show the same normalized to that at $B_{\rm eff} = 20°$. Also shown is the interparticle shadowing effect in simulations performed with various widths of the size distribution: the C, B, and A ring data are compared to simulations with dynamical optical depth $\tau_{\rm dyn} = 0.1$, 2.0, and 1.0, respectively.

The model fits shown in Fig. 13 are made with the Hapke (2002) formulation, which includes both intraparticle shadow hiding and coherent backscattering contributions,

$$g_i(\alpha) = A_i B_{\rm SH}(\alpha) B_{CB}(\alpha). \tag{24}$$

Here $B_{\rm SH}(\alpha)$ describes the intrinsic shadow hiding part, assumed to be similar in form to Eq. (16) used above for fitting the simulated interparticle shadowing, and $B_{CB}(\alpha)$ is the coherent backscattering contribution (with fractional amplitude B_{c0} and HWHM $\approx 0.72 h_c$),

$$B_{CB}(\alpha) = 1 + B_{c0}\frac{1 + \frac{1-e^{-\tan(\alpha/2)/h_c}}{\tan(\alpha/2)/h_c}}{2[1+\tan(\alpha/2)/h_c]^2}. \tag{25}$$

Compared to Hapke (2002), we have omitted from shadow hiding the part containing the Henyey–Greenstein phase function of

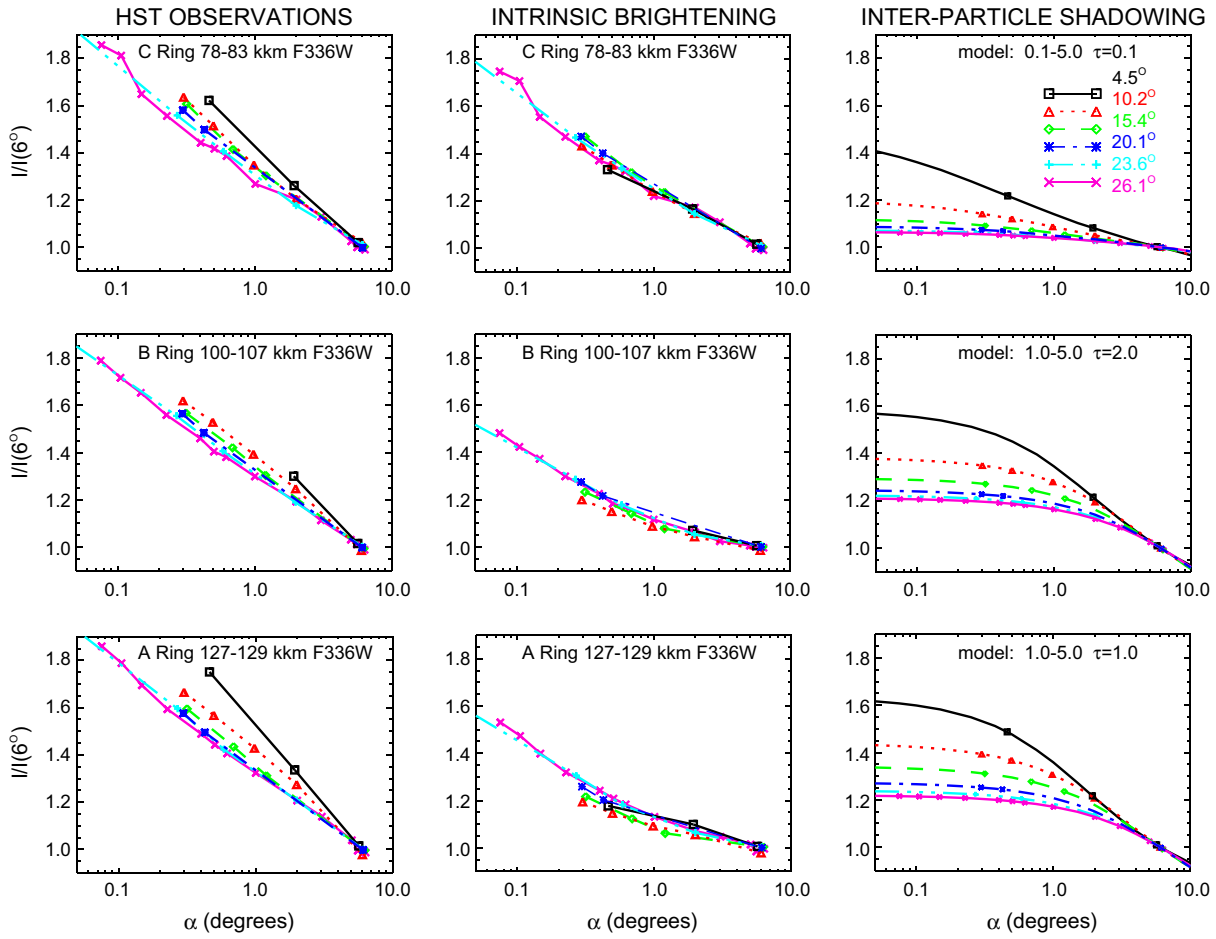

Fig. 12. The left column shows the original HST phase curves for six different sets of $B_{\rm eff}$, all normalized to $\alpha = 6°$. In the middle column, the intrinsic component $g_i(\alpha) = f_i(\alpha)P(\alpha)/[f_i(6°)P(6°)]$ is shown, obtained by dividing out the interparticle shadowing contribution, determined by the best match to the elevation angle dependence of *OE* in Fig. 11: this interparticle shadowing contribution $(f_e(\alpha)/f_e(6°))$ is shown at right. The C, B, and A ring data are compared to simulations with dynamical optical depths $\tau_{\rm dyn} = 0.1$, 2.0, and 1.0, respectively, using a size distribution 0.1–5.0 m for the C ring, and 1.0–5.0 m for the B and A rings. Only the F336W filter is shown. The lines do not represent fits to the data, but simply connect the observations for each $B_{\rm eff}$.

regolith grains, as well as the multiple scattering at the particle surface regolith, since the parameters related to these contributions cannot be reliably determined from the near-opposition data alone. Here, this part is absorbed into a single parameter A_i related to the unspecified optical properties of regolith grains. Note, however, that we apply this fit to data normalized to $\alpha = 6°$: in this case A_i is not an independent parameter but is determined by the normalization and the other parameters. A similar model, except for fitting the original high elevation I/F measurements, and including the full Hapke (2002) formulas for the grain phase function and multiple scattering, was used in French et al. (2007b). As in French et al. (2007b), here we also take into account the finite size and limb darkening of the solar disc in the calculation of model brightness for the near to opposition phase angles.

The parameters of the intrinsic effect fits shown in Fig. 13 are collected in Table 6: the typical RMS residuals of the fits normalized to $\alpha = 6°$ are of the order of 0.015–0.02 (similar to those obtained when using original uncorrected high elevation angle data). For comparison, fits to the intrinsic $g_i(\alpha)$ using the linear-exponential formula (Table 7) yield residuals comparable in magnitude to those using the simplified Hapke model.

Fig. 13 also shows separately the intra-particle SH contribution: in the fitted models, this is conveniently quantified by the enhancement factor at the zero phase, $\mathrm{SH}(0°) = A_i(1 + B_{s0})$. Interestingly, for the A and B rings, the amount of the deduced intra-particle SH is almost negligible ($\mathrm{SH}(0°) \sim 1.0$), except for F336W, where $\mathrm{SH}(0°) \sim 1.1$. For the A and B ring regions, the intrinsic brightening can thus be accounted for almost entirely by the coherent backscattering, with a typical value $CB(0°) = (1 + B_{c0}) \approx 1.4$–1.5. On the other hand, for the C ring the SH brightening is clearly stronger in all filters, with $\mathrm{SH}(0°) \sim 1.3$; in contrast, the CB contribution is quite similar to the B and A ring regions. Note that this kind of separation is not possible when using the original data without removal of the interparticle contribution.

The linear-exponential and Hapke-model fit parameters are further displayed in Figs. 14 and 15, respectively. Altogether, fits to three different data sets are compared:

(1) The original high elevation angle data set used in French et al. (2007b), combining the Cycle 13 exact opposition point for $B_{\rm eff} = 22.9°$ with the $B_{\rm eff} = 26°$ data (upper row).
(2) The original $B_{\rm eff} = 23°$ (Cycles 13 and 9 combined) and $B_{\rm eff} = 26°$ (Cycles 10–12) data sets, the latter normalized to $B_{\rm eff} = 23°$ as described in footnote 6 (middle row).
(3) The combined data set from all $B_{\rm eff}$'s, containing just the intrinsic component (lower row).

Data sets (2) and (3) are those discussed in connection to Fig. 13. A comparison of data sets (1) and (2) (the two first rows in Fig. 14) shows that the A and B ring fits are nearly identical: both sets indicate that HWHM is about 0.1° for the BVRI filters, rising to 0.15–0.20° toward U. However, for the C ring region, although the

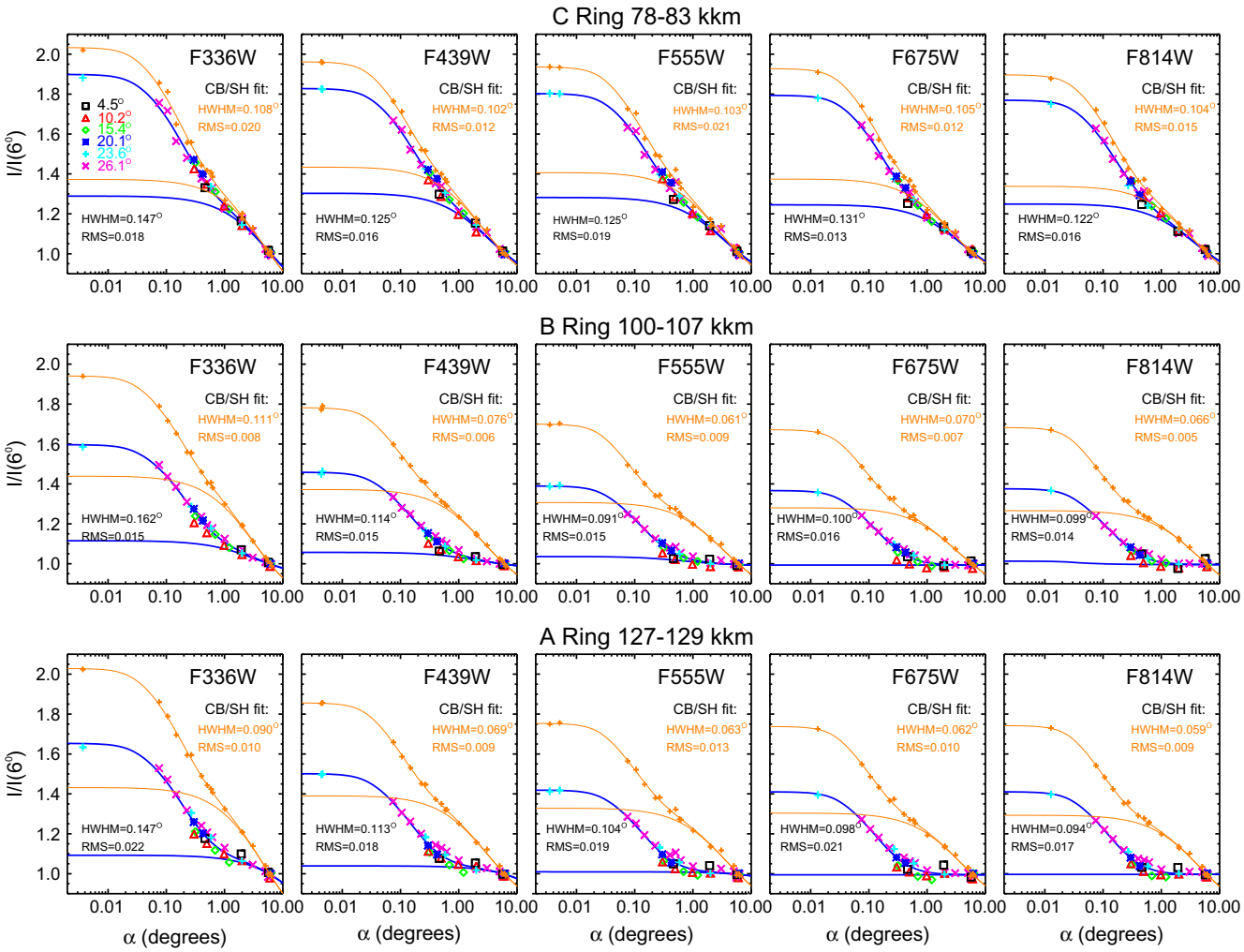

Fig. 13. The intrinsic component of opposition brightening in all five filters, after removing the interparticle shadowing contribution displayed in Fig. 12 (for F336W the points are the same as the middle column of Fig. 12). Thick blue curves indicate the CB/SH (simplified Hapke (2002) model) fits to the data; the lower curve shows the SH contribution separately, while the CB contribution corresponds to the ratio between the two curves. For comparison, the original HST phase curves at $B_{\rm eff}$ = 23–26° are also shown (thin curves, small orange crosses); the ratio between orange and blue curves indicate the magnitude of the interparticle shadowing contribution. The HWHM and residual RMS for both fits are indicated. (For interpretation of the references to color in this figure legend, the reader is referred to the web version of this article.)

Table 6
CB–SH (simplified Hapke) model parameters for the intrinsic opposition effect.[a]

Ring	Filter	A_i	B_{C0}	B_{S0}	h_C	h_S	SH(0)	HWHM	RMS
C	F336W	0.725	0.516	0.781	0.0036	0.052	1.290	0.147	0.0183
	F439W	0.837	0.447	0.559	0.0030	0.029	1.305	0.125	0.0163
	F555W	0.841	0.452	0.526	0.0030	0.032	1.284	0.125	0.0193
	F675W	0.844	0.489	0.477	0.0032	0.036	1.247	0.131	0.0135
	F814W	0.852	0.467	0.469	0.0030	0.034	1.251	0.122	0.0155
B	F336W	0.930	0.467	0.201	0.0039	0.031	1.116	0.162	0.0154
	F439W	0.975	0.426	0.084	0.0028	0.019	1.057	0.114	0.0147
	F555W	0.991	0.395	0.047	0.0022	0.006	1.037	0.091	0.0148
	F675W	0.993	0.431	0.000	0.0024	−0.000	0.993	0.100	0.0164
	F814W	0.996	0.416	0.046	0.0024	0.000	1.041	0.099	0.0136
A	F336W	0.693	0.559	0.578	0.0036	0.165	1.093	0.147	0.0218
	F439W	0.535	0.500	0.940	0.0027	0.591	1.039	0.113	0.0183
	F555W	0.524	0.461	0.928	0.0025	1.920	1.009	0.104	0.0191
	F675W	0.518	0.480	0.921	0.0024	43.44	0.994	0.098	0.0213
	F814W	0.518	0.481	0.924	0.0023	–	0.997	0.093	0.0166*

[a] Intrinsic effect normalized to $\alpha = 6°$ ($=g_i(\alpha)$ defined by Eq. (22)). The A_i, B_{C0}, B_{S0}, h_C, h_S are the original parameters in the fits, while SH(0) = A_i (1 + B_{S0}) and HWHM = 0.72h_c expressed in degrees.

estimated HWHM is more or less the same in all filters for both data sets, there is a nearly twofold difference in the fitted values. A similar difference between the data sets (1) and (2) is also seen in the Hapke model parameters (compare the two uppermost rows of Fig. 15). The difference arises from the inaccurate inclusion of the Cycle 13 exact opposition point among the 26° data without

Table 7
Linear-exponential model parameters for the intrinsic opposition effect.[a]

Ring	Filter	a'	b'	d'	k'	a'/b'	k'/b'	HWHM	RMS
C	F336W	0.632	1.248	0.301	−2.3252	0.507	−0.033	0.208	0.0195
	F439W	0.603	1.223	0.283	−2.0944	0.493	−0.030	0.196	0.0202
	F555W	0.590	1.210	0.285	−1.9575	0.487	−0.028	0.198	0.0211
	F675W	0.579	1.193	0.292	−1.7778	0.485	−0.026	0.202	0.0159
	F814W	0.551	1.192	0.288	−1.7842	0.462	−0.026	0.199	0.0190
B	F336W	0.492	1.095	0.307	−0.9147	0.449	−0.015	0.213	0.0150
	F439W	0.423	1.050	0.212	−0.5067	0.403	−0.008	0.147	0.0152
	F555W	0.389	1.025	0.170	−0.2875	0.379	−0.005	0.118	0.0153
	F675W	0.367	1.001	0.194	−0.0456	0.367	−0.001	0.134	0.0153
	F814W	0.372	1.004	0.184	−0.0684	0.370	−0.001	0.128	0.0152
A	F336W	0.544	1.113	0.249	−1.1088	0.489	−0.017	0.173	0.0209
	F439W	0.469	1.056	0.192	−0.5569	0.444	−0.009	0.133	0.0188
	F555W	0.420	1.027	0.174	−0.2891	0.409	−0.005	0.120	0.0192
	F675W	0.416	1.011	0.173	−0.1587	0.411	−0.003	0.120	0.0209
	F814W	0.416	1.014	0.164	−0.1740	0.411	−0.003	0.114	0.0168

[a] Intrinsic effect normalized to $\alpha = 6°$ ($=g_i(\alpha)$ defined by Eq. (22)). The a', b', d', k' are the original fit parameters, a/b', k'/b' indicate the normalized amplitude of the exponential part, and the normalized linear slope, the HWHM $= d'\ln 2$ expressed in degrees.

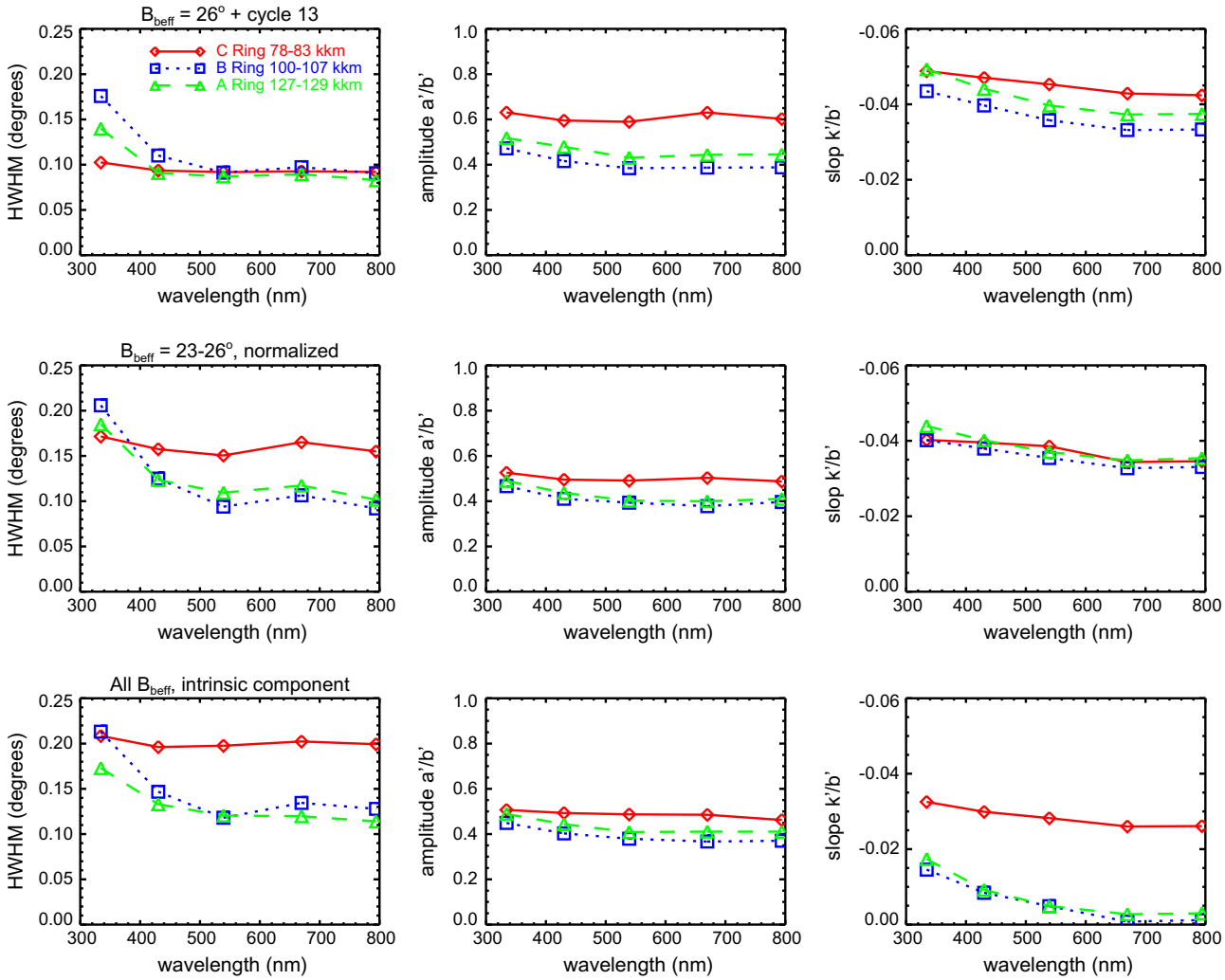

Fig. 14. Wavelength dependence of linear-exponential model fits for the C, B, and A ring regions. The upper row corresponds to the data set used in French et al. (2007b): the $B_{\rm eff} \approx 26°$ data (Cycles 10–12) are combined with the Cycle 13 opposition data point for $B_{\rm eff} \approx 23°$, without any normalization of the I/F levels. The frames display the HWHM, amplitude, and normalized slope from the fits. In the middle row, all original data for $B_{\rm eff} \sim 23°$ and $\sim 26°$ are combined (Cycles 9–13), after proper normalization of the I/F levels to $B_{\rm eff} = 23°$; the interparticle shadowing component has not been eliminated (this corresponds to the thin curves and small orange symbols in Fig. 13). The lower row combines the data from all elevation angles, after removal of the interparticle shadowing component (corresponding to the thick curves and large symbols in Fig. 13).

accounting for the different elevation (data set 1). The strong elevation angle dependence when combining such nearby $B_{\rm eff}$'s is due to the low optical depth of the C ring, making its I/F decrease sharply with elevation angle. That is, for $\tau = 0.1$ the geometrical

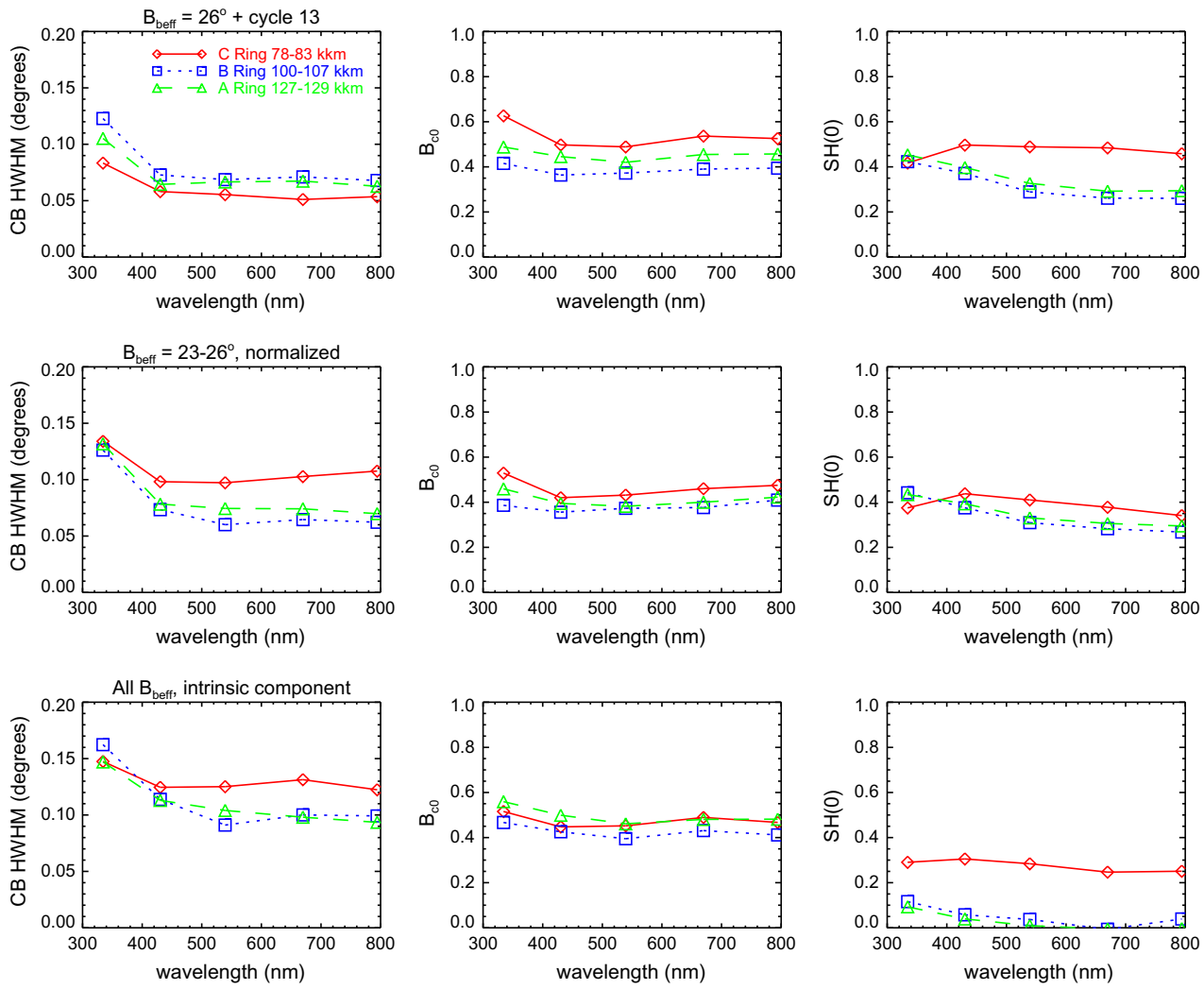

Fig. 15. Same as Fig. 14, except for CB/SH fits. The frames display the coherent backscattering HWHM = $0.72h_{cb}$ (left column) and amplitude B_{c0} (middle column), and the shadow hiding contribution at zero phase angle, $SH(0°) = A_0(1 + B_{s0})$ (right column).

factor in the singly scattered I/F (the exponential term in Eq. (6)) is about 1.1 times larger for $B_{eff} = 23°$ than for $B_{eff} = 26°$. For the higher optical depth B and A rings the dependence is much weaker (for $\tau = 0.5, 1.0, 2.0$ the difference in $(I/F)_{ss}$ is 1.03, 1.005, 1.0001, respectively) and the nearby B_{eff}'s can be safely combined.[7]

Comparing the fits for the intrinsic opposition effect data, and for the original $B_{eff} = 23° + 26°$ data set properly normalized to $B_{eff} = 23°$ (third and second rows, respectively, in Figs. 14 and 15), we can see that the main difference is in the linear slope (for the linear-exponential fits), and in the SH(0) amplitude (for the simplified Hapke-model fits). For the linear-exponential model the slope is significantly reduced, in particular for the B and A rings, and the same is true for the SH(0) in the Hapke model. This quantifies the difference seen in Fig. 13 between the two sets of model curves. On the other hand, the HWHM's are almost unaffected by the removal of interparticle shadowing contribution.

Table 8 lists the intrinsic (SH + CB) and external (interparticle shadowing) contributions to $OE(0.5°) \equiv I(0.5°)/I(6°)$ and $OE(0°) \equiv I(0°)/I(6°)$, for different filters and ring regions. The internal contribution OE_i is calculated from the Hapke fit parameters (solid curves in Fig. 13), and the interparticle contribution OE_e has been calculated for $B_{eff} = 23°$, using the best fit simulation models shown in Fig. 12. The modeled total opposition enhancement is then $OE = OE_i \times OE_e$; for $OE(\alpha = 0°)$ this can be compared to the observed (Cycle 13) $I(0°)/I(6°)$ listed in the last column (showing agreement to within 2%). Table 9 is similar, except that OE_e has been calculated for $B_{eff} = 4.5°$: combined with OE_i the predicted total enhancement $I(0°)/I(6°)$ is about 2.7, 2.5, and 2.6 for the C, B, and A rings, respectively. Unfortunately there are no HST comparison data, since the minimum phase angle during the low elevation angle opposition (Cycle 6) was ≈0.3° (the smallest observed $\alpha = 0.46°$).

5. Tilt effect: interparticle shadowing or multiple scattering?

5.1. HST observations of the tilt effect at different filters and phase angles

Traditionally, the term *tilt effect* refers to the brightening of the B ring with increasing elevation, amounting to as much as 30% for the ground-based range of B_{eff}'s (e.g. Lumme et al., 1983), in contrast to the nearly constant brightness one would expect for an optically thick classical multilayer ring dominated by single scattering. On the other hand, for the A ring the observed I/F was found

[7] In principle, the fact that we are fitting $I/I(6°)$ instead of I/F itself could affect our fits. However, we confirmed that a similar change in the C ring fit parameters is seen in the French et al. (2007b) original fits, if the I/F for the Cycle 13 point is divided by $I_{ss}(23°)/I_{ss}(26°) \approx 1.1$ before combining with the 26° data.

to be nearly constant or slightly decreasing with increasing ring tilt (Lumme and Irvine, 1976b), more consistent with the single scattering prediction, Eq. (6) (I_{ss}/F is a decreasing function of $B_{\rm eff}$ in the case of $\tau \lesssim 0.5$, and practically constant for $\tau \geqslant 0.5$). Note that these early measurements actually refer just to the brightest innermost portion of the A ring: the HST images (Cuzzi et al., 2002) revealed that for the mid-A ring the brightness in fact decreases quite markedly with elevation, much more than predicted by Eq. (6).

In Salo et al. (2004) this A-ring negative tilt effect was attributed to the increased visibility of the gaps between self-gravity wakes at larger elevations. Indeed, this explanation in terms of gaps/wakes is now fully supported by the Cassini occultation measurements (Colwell et al., 2006, 2007; Hedman et al., 2007).

The B ring tilt effect has been viewed as a consequence of multiple scattering, which becomes more important with increasing ring elevation: this is also supported by the fact that the tilt effect is pronounced for the optically thick B ring (Lumme and Irvine, 1976b; Esposito and Lumme, 1977; Lumme et al., 1983). However, from analysis of HST observations showing the lack of significant color variations with respect to ring elevation, Cuzzi et al. (2002) and Poulet et al. (2002) concluded that multiple scattering must be quite weak in the backscattering geometry of Earth-based observations. SK2003 proposed that the tilt effect is a consequence of the variation in the effective filling factor with opening angle, taking place for vertically non-uniform rings. According to this view, based on N-body simulations and Monte Carlo scattering calculations, the observed reflection at low elevations is dominated by the rarefied upper ring layers, which should have a very narrow opposition peak. Thus the tilt-effect observations, made typically at a phase angle of a few degrees, fall outside the opposition peak. However, as the elevation angle increases, the reflection is more and more dominated by the dense equatorial ring layer. This should exhibit a much wider opposition peak, which increases the observed brightness. The magnitude of this effect should also increase with increasing τ. However, in SK2003 no suitable data were available for testing this hypothesis. Note that this explanation is intimately tied to the mechanism generating the opposition effect of the rings: in the previous section we have shown that this contains both intrinsic and interparticle contributions. It is therefore important to test the SK2003 hypothesis for the tilt effect, using the HST data.

The observed tilt effect is illustrated in Fig. 16, which displays radial profiles of the ring ansa brightness at several elevations, normalized to that at $B_{\rm eff} = 4.5°$. Observations with the filter F555W are shown separately for two phase angles: $\alpha = 6°$ (upper panel) and $\alpha = 0.5°$ (lower panel). The $\alpha = 6°$ plots correspond to Fig. 8b in Cuzzi et al. (2002), except for the normalization. They show the strong positive tilt effect (I/F increasing with increasing $B_{\rm eff}$) for the brightest part of the B ring, and a weaker but still positive effect in the innermost A and B rings. In contrast, the mid-A ring (124,000–133,000 km) has a negative tilt effect, due to the aforementioned wakes.

At low phase angle ($\alpha = 0.5°$), the behavior changes quite markedly. For the A ring, the negative tilt effect is even more pronounced at $\alpha = 0.5°$ than at $\alpha = 6°$. In the inner B ring (93,000–99,000 km), the tilt effect is now also negative, and a positive effect is prominent only in the region 105,000–110,000 km.

To exclude the possibility that the differences could be due to anomalous behavior of $B_{\rm eff} = 4.5°$ images (some of which were affected by spokes, though not the ones included to Figs. 16 and 17) compares two other filters, this time normalized to $B_{\rm eff} = 10°$. Overall, a very similar behavior is seen as in the previous figure, although the B ring $\alpha = 6°$ tilt effect appears a bit stronger for F814W than for F336W.

Table 9
Modeled intrinsic and interparticle opposition effects at $B_{\rm eff} = 4.5°$.[a]

Filter	$OE_i(0.5°)$	$OE_e(0.5°)$	$OE(0.5)$	$OE_i(0.0°)$	$OE_e(0.0°)$	$OE(0.0°)$
C ring 78,000–83,000 km, model: $\tau_{dyn} = 0.1$, 0.1–5.0 m						
F336W	1.35	1.21	1.63	1.86	1.46	2.72
F439W	1.32	1.21	1.59	1.79	1.46	2.62
F555W	1.30	1.21	1.57	1.76	1.46	2.58
F675W	1.28	1.21	1.55	1.76	1.46	2.57
F814W	1.28	1.21	1.54	1.73	1.46	2.54
B ring 100,000–107,000 km, model: $\tau_{dyn} = 2$, 1–5.0 m						
F336W	1.18	1.45	1.72	1.57	1.58	2.48
F439W	1.09	1.45	1.58	1.42	1.58	2.25
F555W	1.05	1.45	1.52	1.35	1.58	2.14
F675W	1.03	1.45	1.50	1.34	1.58	2.11
F814W	1.03	1.45	1.50	1.34	1.58	2.12
A ring 127,000–129,000 km, model: $\tau_{dyn} = 1$, 1–5.0 m						
F336W	1.18	1.48	1.74	1.62	1.63	2.64
F439W	1.09	1.48	1.61	1.46	1.63	2.39
F555W	1.05	1.48	1.56	1.38	1.63	2.26
F675W	1.04	1.48	1.53	1.37	1.63	2.24
F814W	1.04	1.48	1.53	1.37	1.63	2.24

[a] The symbols $OE(0.5°) \equiv I(0.5°)/I(6°)$, and $OE(0°) \equiv I(0°)/I(6°)$. The total opposition effect is the product of the intrinsic and external (interparticle) contributions; $OE(0°) = OE_i(0°) \times OE_e(0°)$, $OE(0.5°) = OE_i(0.5°) \times OE_e(0.5°)$. The last column lists the observed $I(0.5°)/I(6°)$.

Table 8
Modeled intrinsic and interparticle opposition effects at $B_{\rm eff} = 23°$.[a]

Filter	$OE_i(0.5°)$	$OE_e(0.5°)$	$OE(0.5°)$	$OE_i(0.0°)$	$OE_e(0.0°)$	$OE(0.0°)$	$OE_{\rm obs}(0°)$
C ring 78,000–83,000 km, model: $\tau_{dyn} = 0.1$, 0.1–5.0 m							
F336W	1.35	1.05	1.42	1.86	1.07	1.99	2.02
F439W	1.32	1.05	1.39	1.79	1.07	1.92	1.96
F555W	1.30	1.05	1.37	1.76	1.07	1.89	1.94
F675W	1.28	1.05	1.35	1.76	1.07	1.88	1.91
F814W	1.28	1.05	1.34	1.73	1.07	1.86	1.88
B ring 100,000–107,000 km, model: $\tau_{dyn} = 2$, 1–5.0 m							
F336W	1.18	1.20	1.42	1.57	1.22	1.91	1.94
F439W	1.09	1.20	1.31	1.42	1.22	1.74	1.77
F555W	1.05	1.20	1.26	1.35	1.22	1.66	1.70
F675W	1.03	1.20	1.24	1.34	1.22	1.63	1.66
F814W	1.03	1.20	1.24	1.34	1.22	1.63	1.67
A ring 127,000–129,000 km, model: $\tau_{dyn} = 1$, 1–5.0 m							
F336W	1.18	1.21	1.43	1.62	1.24	2.00	2.02
F439W	1.09	1.21	1.32	1.46	1.24	1.81	1.85
F555W	1.05	1.21	1.27	1.38	1.24	1.71	1.75
F675W	1.04	1.21	1.25	1.37	1.24	1.70	1.73
F814W	1.04	1.21	1.25	1.37	1.24	1.70	1.73

[a] The symbols $OE(0.5°) \equiv I(0.5°)/I(6°)$, and $OE(0°) \equiv I(0°)/I(6°)$. The total opposition effect is the product of the intrinsic and external (interparticle) contributions; $OE(0°) = OE_i(0°) \times OE_e(0°)$, $OE(0.5°) = OE_i(0.5°) \times OE_e(0.5°)$.

5.2. Modeling the B ring tilt effect

In principle, both interparticle shadowing and multiple scattering can cause a positive tilt effect. Our goal in this section is to provide a quantitative estimate of how much these factors contribute to the observed B ring tilt effect. For interparticle shadowing, our estimate follows directly from the opposition effect models of the previous section. An estimate for the fractional amount of multiple scattering, Q_{ms}, can be obtained by comparing the magnitude of the tilt effect at long and short wavelengths. The particle albedo increases significantly with wavelength in the visual regime, which also increases the relative amount of multiple scattering: thus the contribution of multiple scattering, if significant at all, should result in a strong wavelength dependence in the tilt effect. Our approach here, for multiple scattering, is thus very similar to the Cuzzi et al. (2002) color analysis.

We quantify the tilt effect by the ratio of scaled intensities, $\widehat{I} = I/I_{ss}$, measured at a given elevation, normalized to that of $\widehat{I}$ at $B_{\rm eff} = 4.5°$. Using the ratio of scaled intensities, instead of intensities, simply removes the geometric contribution to the tilt effect arising from the factor $1 - \exp(-2\tau/\sin B_{\rm eff})$ in I_{ss} (i.e. at small τ, $I_{ss}(B)$ is a decreasing function of B while at larger τ it is practically constant). The difference is not large: compare the two uppermost frames in Fig. 18, showing the A and B ring tilt effect, by plotting either the ratio of intensities (upper frame), or that of scaled intensities (middle frame) as a function of *Voyager* Photopolarimeter Subsystem (PPS) optical depth, obtained from the NASA Planetary Data System Rings Node (Showalter et al., 1996). Both profiles highlight the strong τ dependence of the tilt effect.

Denoting the ratio $\widehat{I}(B_{\rm eff})/\widehat{I}(B_{\rm eff} = 4.5°)$ by R_B, we have

$$R_B(\alpha, B_{\rm eff}, \tau, \lambda) = \frac{(I/I_{ss})(\alpha, B_{\rm eff}, \tau, \lambda)}{(I/I_{ss})(\alpha, B_{\rm eff} = 4.5°, \tau, \lambda)} \approx \frac{f_i(\alpha, \lambda) f_e(\alpha, B_{\rm eff}, \tau) + Q_{ms}(B_{\rm eff}, \tau, \lambda)}{f_i(\alpha, \lambda) f_e(\alpha, B_{\rm eff} = 4.5°, \tau)},$$

where we have utilized the fact that Q_{ms} in Eq. (5) is insignificant at $B_{\rm eff} = 4.5°$ (Cuzzi et al., 2002). Furthermore, when evaluated at $\alpha = 6°$, we can safely assume that $f_i \approx 1$ (since its HWHM in Section 4 found to be $\ll 6°$). Therefore,

$$R_B(\alpha = 6°, B_{\rm eff}, \tau, \lambda) \approx \frac{f_e(\alpha = 6°, B_{\rm eff}, \tau) + Q_{ms}(B_{\rm eff}, \tau, \lambda)}{f_e(\alpha = 6°, B_{\rm eff} = 4.5°, \tau)}. \quad (26)$$

Since $Q_{ms} \ll 1$, we may further approximate

$$R_B(\alpha = 6°, B_{\rm eff}, \tau, \lambda) \approx \frac{f_e(\alpha = 6°, B_{\rm eff}, \tau)}{f_e(\alpha = 6°, B_{\rm eff} = 4.5°, \tau)} + Q_{ms}(B_{\rm eff}, \tau, \lambda). \quad (27)$$

Since according to Fig. 9, the factor $f_e(\alpha = 6, B_{\rm eff} = 4{,}5°, \tau)$ should be close to unity. This approximation illustrates that the tilt effect can indeed be partly due to interparticle shadowing (the $f_e(B_{\rm eff})/f_e(4.5°)$ term), and partly due to multiple scattering (Q_{ms}): both imply enhanced ring brightness at larger $B_{\rm eff}$, and also at larger τ. Concerning the interparticle shadowing contribution, the various size distribution models of Fig. 9 in Section 3 imply an enhancement by 1.25–1.35 for $B_{\rm eff} = 26°$, $\tau_{\rm dyn} = 1.5$, all in qualitative agreement with the B ring observations. The interparticle shadowing effect is thus very robust, in the sense that it does not require very specific ring models in order to be able to account for the observed strong tilt effect.

To isolate the Q_{ms} contribution, we form the difference of R_B at two different filters, with wavelengths λ_1 and λ_2,

$$\Delta_\lambda R_B = R_B(\alpha = 6°, B_{\rm eff}, \tau, \lambda_2) - R_B(\alpha = 6°, B_{\rm eff}, \tau, \lambda_1) \approx Q_{ms}(\lambda_2) - Q_{ms}(\lambda_1). \quad (28)$$

Following Cuzzi et al. (2002; their Appendix) we assume that the multiply-scattered flux $I_{ms}(\lambda) \propto [A(\lambda)]^n$, where $n \approx 2$–3 indicates the typical order of scattering responsible for multiply scat-

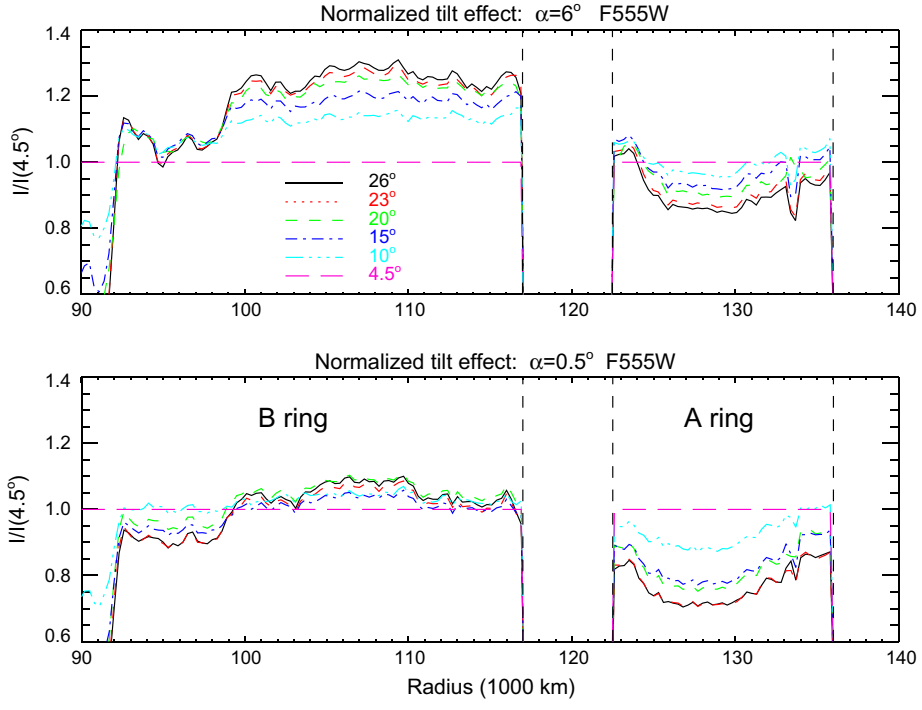

Fig. 16. The tilt effect on the brightness of the A and B rings, for $\alpha \sim 6°$ (upper frame) and $\alpha \sim 0.5°$ (lower frame). Radial F555W brightness profiles at the ansa have been grouped together by $B_{\rm eff}$ and averaged, and then normalized by the low ring elevation profile with $B_{\rm eff} = 4.5°$. Note the positive tilt effect for the B ring and the negative (inverse) tilt effect for the A ring.

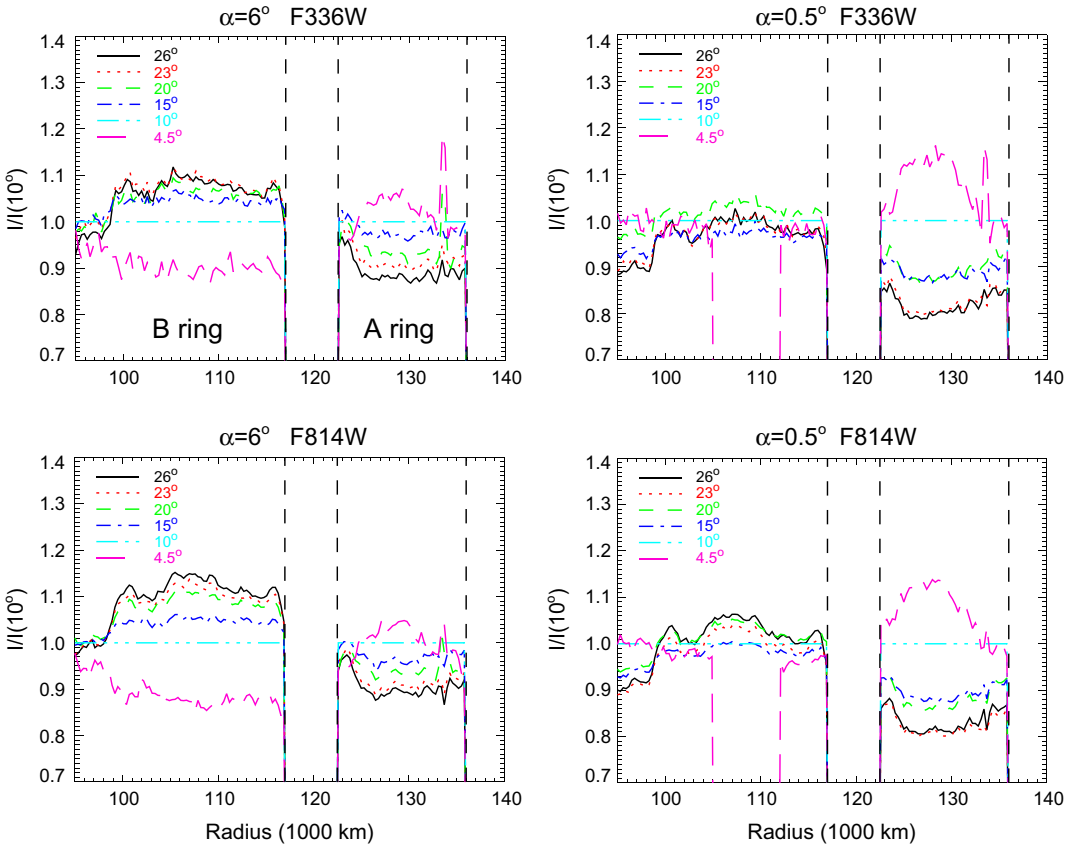

Fig. 17. Comparison of the B and A ring tilt effects, for non-opposition ($\alpha \sim 6°$) and near opposition ($\alpha \sim 0.5°$), for two filters. Since the low phase angle $B_{\rm eff} = 4.5°$ images were contaminated by spokes, we have made the normalization to $B_{\rm eff} = 10°$, and omit the affected region (105,000–112,000 km). Note how the B ring positive tilt effect is marginally larger for the larger λ in the case of $\alpha \sim 6°$, indicating that some fraction of the brightness increase is due to multiple scattering increasing with elevation, as proposed by Lumme et al. (1983); however, the contribution is small compared to that of elevation-dependent opposition brightening.

tered light. The ratio of fractional multiple scattering contributions at different wavelengths is then $Q_{ms}(\lambda_2)/Q_{ms}(\lambda_1) \sim [A(\lambda_2)/A(\lambda_1)]^{n-1}$. Eliminating $Q_{ms}(\lambda_1)$ leads to an estimate

$$Q_{ms}(\lambda_2) \sim \frac{\Delta_\lambda R_B}{1 - [A(\lambda_1)/A(\lambda_2)]^{n-1}}. \tag{29}$$

Since the backscattered flux is dominated by single scattering, the ratio of albedos can be roughly estimated as $A(\lambda_1)/A(\lambda_2) = I_{ss}(\lambda_1)/I_{ss}(\lambda_2) \approx I(\lambda_1)/I(\lambda_2)$ evaluated at $\alpha = 6°, B_{\rm eff} = 4.5°$ (having minimal contribution of multiple scattering and opposition brightening). For the studied B ring region the observed I/F's at $B_{\rm eff} = 4.5°$, $\alpha = 6°$ are 0.16 and 0.44 at F336W and F814W, respectively. Eq. (29), together with $n \sim 2$ then indicates $Q_{ms}(\text{F814W}) \sim 1.5\Delta_\lambda R_B$. According to lowermost frame of Fig. 18, the maximum of $\Delta_\lambda R_B$ is ~0.1, suggesting a maximal $Q_{ms} \sim 0.15$ for the F814W filter (and ~0.05 for F336W). This justifies the omission of Q_{ms} in previous sections (the fractional error of the derived f_i is of the order of Q_{ms}). Comparing to the interparticle shadowing contribution (about 30% enhancement in R_B) we can now estimate that the relative contribution of multiple scattering to the tilt effect should be about 1/3 of the total effect, at most, and practically negligible at shorter wavelengths. The multiple scattering contribution corresponds roughly to the difference between the F814W and F336W trends in Fig. 18 (upper or middle frame, whereas the difference of F336W points from the theoretical single scattering curve represents the interparticle shadowing factor).

The consistency of the estimated Q_{ms} can also be checked by a direct comparison with simulation models. For example, the observed I/F in the B ring region (for $B_{\rm eff} = 26°$, $\alpha = 6°$) can be reproduced with an $n_s = 3.09$ power-law phase function by assuming $A_{336} = 0.21$ and $A_{814} = 0.57$, when the dynamical model with $\tau_{\rm dyn} = 2.0, W_s = 10$ is assumed. The same model implies $R_B(814) - R_B(336) \sim 0.04$ (with the simulated maximum $Q_{ms} \sim 0.06$), which is smaller but still in fair agreement with the $\Delta_\lambda R_B \sim 0.06$ implied by the observations for the B ring region. On the other hand, for a Lambert phase function, albedo values 0.36 and 0.87 would be required for these two filters. This in turn would imply $R_B(814) - R_B(336) \sim 0.2$ (and $Q_{ms} \sim 0.35$), a factor of three larger than the observed difference between the two filters. In Fig. 18 (bottom row) we also plot the modeled ΔR_B as a function of τ, for the two phase functions, using the above albedo values. We conclude that the particles are significantly more backscattering than Lambert spheres, and are more similar to those implied by the $n_s = 3.09$ power law. This is consistent with previous studies based on direct fitting of large range Voyager phase curves (Dones et al., 1993).

The reduction of the B ring tilt effect from $\alpha = 6°$ to 0.5°, which was shown in Fig. 16, is just what is expected if the elevation-dependent interparticle shadowing is primarily responsible for the observed tilt effect. To see this, we may form

$$\begin{aligned} R_B(\alpha = 0.5°, B_{\rm eff}, \tau, \lambda) &\approx \frac{f_i(\alpha = 0.5°, \lambda) f_e(\alpha = 0.5°, B_{\rm eff}, \tau) + Q_{ms}(B_{\rm eff}, \tau, \lambda)}{f_i(\alpha = 0.5°, \lambda) f_e(\alpha = 0.5°, B_{\rm eff} = 4.5°, \tau)} \\ &= \frac{f_e(\alpha = 0.5°, B_{\rm eff}, \tau)}{f_e(\alpha = 0.5°, B_{\rm eff} = 4.5°, \tau)} \\ &\quad + \frac{Q_{ms}(B_{\rm eff}, \tau, \lambda)}{f_i(\alpha = 0.5°, \lambda) f_e(\alpha = 0.5°, B_{\rm eff} = 4.5°, \tau)}. \end{aligned} \tag{30}$$

Close to opposition, we can approximate $f_i f_e \sim 2$ in the divisor of the Q_{ms} term, leading to

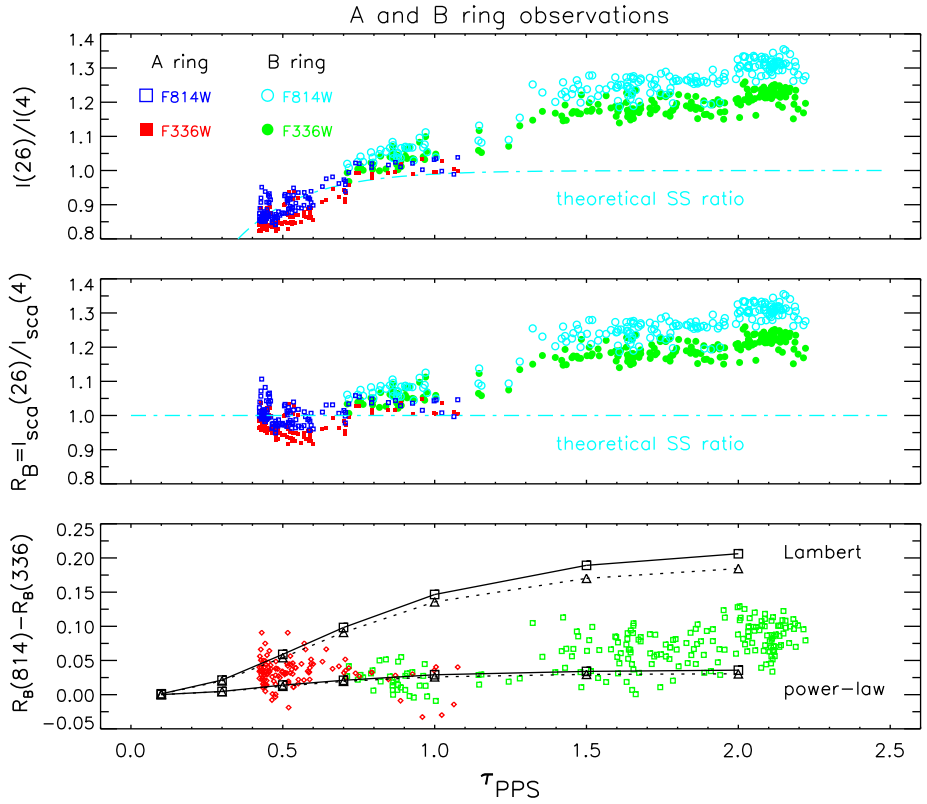

Fig. 18. Upper panel: Observed $I(B_{\rm eff}=26°)/I(B_{\rm eff}=4.5°)$ vs. Voyager PPS optical depth, plotted in F814W and F333W filters for $\alpha=6°$. The dash-dotted curve indicates the theoretical ratio of singly scattered intensities: the values exceeding this curve indicate positive (B ring) or negative (mid A ring) tilt effect. The middle panel frame shows the the same, but using scaled intensities: $R_B=\widehat{I}(26°)/\widehat{I}(4.5°)$, where $\widehat{I}(r)=I(r)/I_{ss(D=0)}(\tau_{pps}(r))$; here, the theoretical singly scattered ratio is unity. Lower row: the difference R_B(F814W) − R_B(F336W), which represents the contribution of multiple scattering. Also shown are simulation models using both Lambert phase and $n_s=3.09$ power-law phase functions: solid and dotted lines stand for simulations with size distributions of 0.1–5.0 m and 0.5–5.0 m, respectively. The assumed particle albedos for F333W and F814W filters are 0.36 and 0.87, respectively, when the Lambert phase function is used, and 0.21 and 0.57 in connection with the power-law phase function: with these assumptions the modeled I/F values for 0.5–5.0 m size distribution match the observations at $B_{\rm eff}=26°$, $\alpha=6°$.

$$R_B(\alpha=0.5°,B_{\rm eff},\tau,\lambda)\approx\frac{f_e(\alpha=0.5°,B_{\rm eff},\tau)}{f_e(\alpha=0.5°,B_{\rm eff}=4.5°,\tau)}+0.5Q_{ms}(B_{\rm eff},\tau,\lambda). \quad (31)$$

According to Fig. 9, the interparticle shadowing factor (the first term in Eq. (31)) is reduced for $\alpha=0.5°$ when compared to $\alpha=6°$: in particular, for the narrow $W_s=5$–10 size distributions, favored by the opposition phase curve fits of Section 4, the modeled $f_e(26°)/f_e(4°)\sim1.15$, significantly smaller than the ∼1.3 for $\alpha=6°$. This drop in the magnitude of the interparticle shadowing tilt effect, from ∼30% to ∼15%, is in remarkable agreement with observations shown in Fig. 16. Also, according to Eq. (31) the contribution from multiple scattering should be reduced to roughly one-half for the smaller phase angle. This is consistent with observations showing a weaker wavelength dependence of tilt effect when α is reduced (see Fig. 17).

In summary, the interparticle shadowing mechanism, by which the interparticle opposition peak widens at larger elevations, can account quite well for the observed positive tilt effect of the B ring. Additionally, its phase angle dependence – the differences seen between $\alpha=0.5°$ and 6.0° – are accounted for; this effect had not been considered in earlier studies, which concentrated on $\alpha=6.0°$. The increased amount of multiple scattering with elevation seems to be a secondary effect, accounting primarily for the slightly stronger tilt effect at longer wavelengths.

5.3. Self-gravity wakes and the negative A ring tilt effect

So far, our model comparisons have been made with non-gravitating simulations. On the other hand, Saturn's A and B rings are known to possess self-gravity wake structures (Salo, 1992b, see also Toomre and Kalnajs, 1991; Colombo et al., 1976), responsible for the optical brightness asymmetry (Camichel, 1958; Lumme and Irvine, 1976a; Thompson et al., 1981; Franklin et al., 1987; Dones et al., 1993) and the optical depth variations detected with various Cassini instruments (Colwell et al., 2006, 2007; Hedman et al., 2007; Ferrari et al., 2009). Here we address the connection of wakes to the negative tilt effect observed in the mid A ring. We model this region with the same two standard self-gravity models that were used in Salo et al. (2004) and French et al. (2007a) for studies of the A ring azimuthal brightness asymmetry. In the first model, identical particles are assumed (IDE), while the second model (SIZE) employs a $q=3$ power law with $W_s=10$. In both cases $\tau_{\rm dyn}=0.5$, internal particle density $\rho=450$ kg m^{-3} is assumed together with the Bridges et al. (1984) elasticity law. As shown in French et al. (2007a), the asymmetry amplitude implied by these two models brackets the observed asymmetry in HST observations: the IDE-model yields about 15% too large asymmetry amplitude, while that of the SIZE-model is about 40% too small. In other respects the IDE model is also clearly better: it matches nicely the elevation angle dependence of the asymmetry amplitude, and moreover yields the correct minimum longitude, whereas for the SIZE model the minimum longitude is off by about 5°; this mismatch in minimum longitude for the supposedly more realistic size distribution models was recently confirmed by Porco et al. (2008). The transmission properties of the models are also in accordance with low elevation ($B=3.45°$) VIMS occultation studies (Hedman et al., 2007): the IDE and SIZE models imply maximum transmission probabilities $T=0.09$ and 0.02, respectively, while the obser-

vations indicate $T \approx 0.08$. Although one can fine tune the strength of asymmetry in the simulation models (see Fig. 9 in French et al. (2007a), displaying the effect of changing the elasticity law or the underlying dynamical optical depth), these two models are probably sufficient to cover the qualitative effects of the wake structure on the tilt effect. For comparison, we will also show results from non-gravitating size distribution simulations with $W_s = 10$, both for $\tau_{dyn} = 0.5$ and for $\tau_{dyn} = 2.0$.

As we discussed in the previous sub-section, the $\alpha = 0.5°$ observations lie largely inside the interparticle shadowing opposition peak, regardless of the observing elevation, so there should be no significant increase of brightness with B_{eff} due to the improved visibility of the dense central layer. This dependence on phase angle is displayed in a more quantitative way in Fig. 19, showing the observed (I/F) vs. B_{eff} in the same B and A ring regions for which the opposition phase curves were studied in the previous sections. The dense B ring behavior is plotted in the upper left corner, matched reasonably well by the simulation model (similar to the SIZE model, but with no self-gravity and with $\tau_{dyn} = 2.0$), at both $\alpha = 6°$ and $\alpha = 0.5°$.

The importance of including self-gravity when modeling the A ring is clearly seen in the upper right corner of Fig. 19. Here, the agreement of the non-gravitating $\tau_{dyn} = 0.5$ model with the mid-A ring tilt curve (upper right corner) is far from satisfactory. The model curves are almost flat, whereas the observed I/F are monotonically decreasing with B. The observed brightness *difference* between the $\alpha = 6°$ (open circles) and $\alpha = 0.5°$ (filled circles) ring brightnesses is, however, well described by the difference between the corresponding model curves (dashed and solid lines, respectively). This suggests that the opposition effect-related brightening with B_{eff} acts in the A ring just as in the B ring, and that the systematic decline is due to an additional effect missing from the homogeneous non-gravitating model. Indeed, the strong asymmetry attributed to gravity wakes is expected to be accompanied by a negative tilt effect (Salo et al., 2004). The two bottom panels display the results for the two previously introduced self-gravitating models, which again bracket the observed behavior (note that no attempt was made to fit the data points). Curiously, for the tilt effect the SIZE model seems to be closer to observations than the IDE model (the opposite was true for asymmetry and transmission amplitudes; this probably implies that some ingredient is still missing from current simulation models for the A ring gravity wakes).

Gravity wakes have also been inferred for the B ring, but occultation studies (Colwell et al., 2006, 2007) suggest that the gaps in the B ring are relatively more narrow in comparison to A ring wakes. Thus their influence on the surface area and the reflection properties is not so pronounced. This is in accordance with the weaker reflection asymmetry in HST and radar observations (Nicholson et al., 2005; French et al., 2007a). Only in the less dense inner B ring is the asymmetry amplitude noticeable (French et al., 2007a). Interestingly, in this same region the tilt effect seems to be much smaller than in the other parts of the B ring (see Fig. 16). Still, the interparticle shadowing mechanism seems to be important in the inner B ring, evidenced by the reduction of the tilt effect for $\alpha = 0.5°$ (in fact, it turns into a negative tilt effect). It thus seems that the interparticle shadowing mechanism (pro-

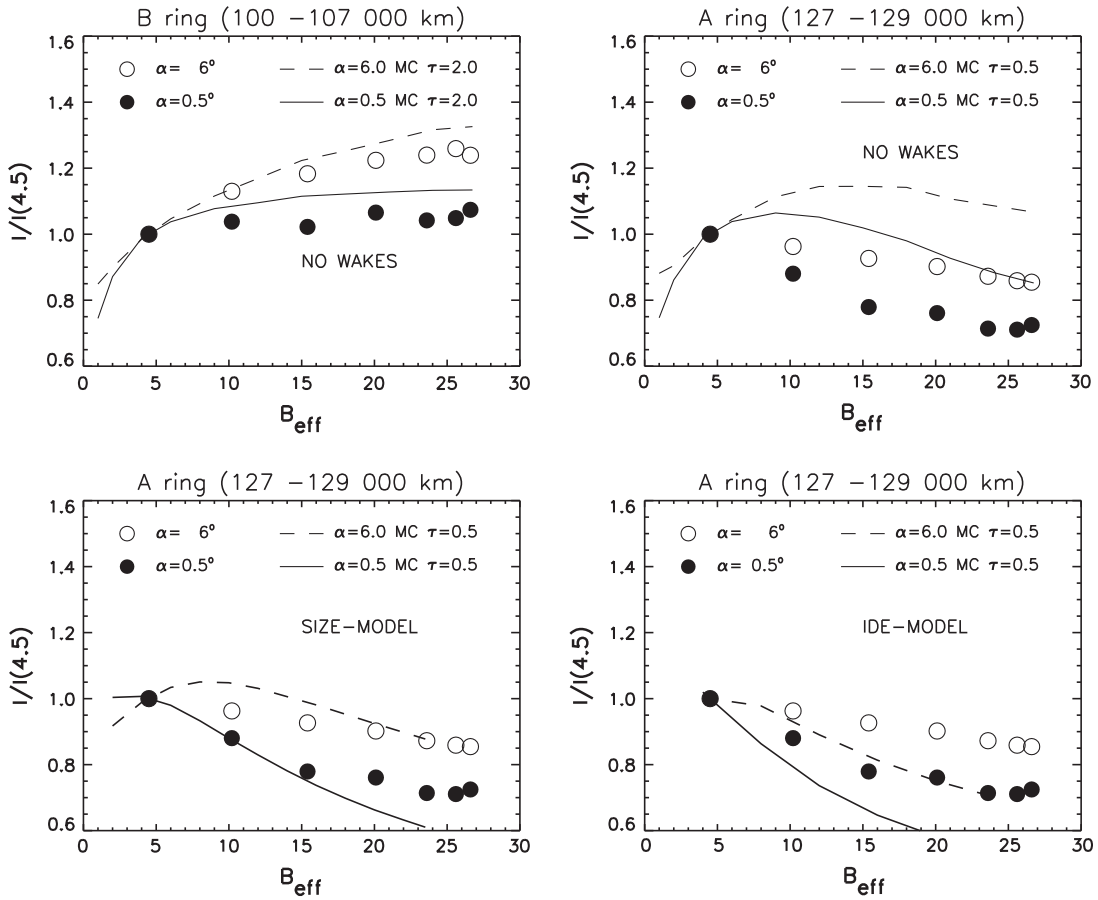

Fig. 19. Comparison of the observed B and A ring tilt effects with photometric models, for $\alpha \sim 6°$ and for $\alpha \sim 0.5°$. We have extracted the intensity at the ring ansa vs. B_{eff} at the indicated radial ranges. The upper row displays observations for the B and A rings, together with results of photometric models, using non-gravitating particle simulations, with size distribution from 0.5 to 5.0 m, and with $\tau_{dyn} = 2.0$ and $\tau_{dyn} = 0.5$. In the lower row, the A ring observations are compared with the self-gravitating SIZE and IDE models explored in Salo et al. (2004) and French et al. (2007a). The $n_s = 3.09$ power-law phase function with albedo A = 0.5 is assumed.

moting positive tilt effect) is important for both the A and B rings, though for the mid A ring, and to lesser degree also in the inner B ring, the effect of gravity wakes/gaps (providing a negative contribution to tilt effect) needs to be taken into account as well.

6. Discussion and conclusions

The analysis of Hubble Space Telescope near-opposition phase curves obtained for $B_{\rm eff} = 4.5$–$26.1°$ shows unambiguously that the opposition brightening of Saturn's rings depends on the ring elevation. This is most strikingly evidenced by Fig. 5, showing the systematic steepening of the slope of I/F vs. $\ln\alpha$ when $B_{\rm eff}$ gets smaller. This previously unreported dependence demonstrates the unique value of the 1996–2005 HST data set that spans a full Saturn season (Cuzzi et al., 2002; French et al., 2007b). Comparison of the different filters indicates that, although the magnitude of the total opposition effect increases toward shorter wavelengths, the elevation dependent part is practically the same in all filters. This elevation dependence, and its independence of wavelength, provide strong observational confirmation for the presence of an interparticle shadowing opposition effect, in accordance with dynamical/photometric simulations (SK2003).

In contrast to the present study, it is not possible from single-elevation reflection data alone to disentangle the intrinsic (coherent backscattering and/or shadow hiding at particle surfaces) and interparticle shadowing contributions, since the expected functional forms are rather similar (e.g. Hapke, 2002). This difficulty is particularly true for the intrinsic SH contribution, which is described by the same function that accurately fits the modeled near-opposition *interparticle* shadowing, although they might have different amplitudes and HWHM's. In principle, the wavelength dependence of CB might be used to disentangle the various contributions, but unfortunately there is no current theoretical agreement about what kind of wavelength dependence to expect. Also, the observational picture is not clear, probably because of differences in available α ranges, and the fitting functions used. Analysis of high-elevation HST data (French et al., 2007b) implies that the opposition effect has a nearly constant HWHM $\sim 0.1°$ for BVRI filters, increasing slightly at U. This is somewhat in contrast to the analysis of Cassini ISS data (Deau et al., 2009; similarly referring to high elevation $B_{\rm eff} \sim 22°$) that indicates a roughly twofold larger HWHM, reaching a maximum in the green filter. On the other hand, Cassini VIMS phase curves suggest that at near-infrared the HWHM increases rapidly with wavelength, from 0.2° to >1° between 1.5 μm and 3.5 μm (Hapke et al., 2006).

Polarization measurements would be helpful, since models predict (Hapke, 1990; Mishchenko, 1993; Rosenbush et al., 1997) that the CB intensity peak should be accompanied by a similar narrow peak in the degree of polarization (both circular and linear). Existing ground based measurements of linear polarization (Lyot, 1927; Johnson et al., 1980; Dollfus, 1996), although not ruling out such a peak, do not have sufficient accuracy or wavelength coverage – or mutual agreement – for quantitative comparison to intensity light curves. Unfortunately, the polarization capabilities of Cassini are inadequate for such studies.

Independent support for the interparticle shadowing opposition effect is provided by the Cassini CIRS measurements, showing a pronounced opposition effect in the ring's thermal phase curves (Altobelli et al., 2009). CB is ruled out, since there can be no interference between the incoming visual photons heating the particle and the infrared photons reradiating the heat. Compared to the strongly peaked visual phase curves the thermal opposition effect extends over several tens of degrees. However, quantitative comparison to the optical phase curve must await detailed thermal modeling that extends beyond the current models such as those of Ferrari and Leyrat (2006) and Morishima et al. (2009).

As demonstrated in Section 4, the elevation-dependent part of the opposition effect in the HST data can be removed via model comparisons. In practice, we used a set of photometric/dynamical simulations performed for various optical depths and widths of size distributions, and used a fixed phase angle range $\alpha = 0.5$–$6°$, where the difference in the observed brightening $I(6°)/I(0.5°)$ for different $B_{\rm eff}$'s was compared with that predicted by simulations. The fact that interparticle multiple scattering is not significant simplified these comparisons, as it was sufficient to compare with the enhancement factor f_e, giving the ratio of the simulated single scattering contribution with respect to the theoretical $D = 0$ formula. The deduced interparticle contribution was divided out from the observations, leaving what presumably represents the intrinsic contribution f_i.

Comparison to simulations, with $\tau_{\rm dyn} = 0.1$–2.0, indicated that the interparticle enhancement f_e is quite well fitted with the functional form of the Hapke (1986) shadowing model for semi-infinite layers. In practice, the finite optical depth affects the maximum amplitude of f_e, which is reduced when the path optical depth decreases (this decrease in turn is in good accordance with Lumme and Bowell (1981) theoretical calculations, see SK2003). The dependence of HWHM on the width of the size distribution is at least qualitatively consistent with Hapke's Y-function. Regardless of the good agreement with theoretical treatments, the self-consistent dynamical simulations together with photometric modeling are still indispensable, in order to account correctly for the elevation-dependent interparticle shadowing, which is sensitive to the vertical structure of the ring, via the effective volume density $D_{\rm eff}$ at the layer mainly responsible for scattering. Simulations indicate roughly linear dependence, HWHM $\propto B_{\rm eff}$, which acts in addition to the size distribution dependence implied by the Hapke's formula. Additionally, simulations indicate that HWHM is practically independent of $\tau_{\rm dyn}$ (see Fig. 8).

From their analysis of Cassini ISS phase curves, typically extending to $\alpha \sim 25°$, Deau et al. (2009) found that the slope of the phase curve outside the opposition peak shows a clear correlation with optical depth (they used a linear-by-parts fit, and this outer slope corresponds to linear component beyond $\alpha > 0.3°$). They conclude that this steepening is contrary to what would be expected from interparticle shadowing: they reason that higher $\tau_{\rm dyn}$ generally implies larger volume density and thus presumably also more extended interparticle shadowing opposition effect, e.g. phase curves should have less steep slope outside the central peak due to the intrinsic opposition effect. Deau et al. (2009) then conclude that the τ dependence of the slope must follow from different particle surface properties at low and high τ environments, rather than be a result of interparticle shadowing. However, according to our detailed calculations, the variation of the interparticle shadowing effect with optical depth seems consistent with the observations. For example, Fig. 10 indicates that the slope beyond the central maximum is generally steeper for larger $\tau_{\rm dyn}$'s. The reason for this behavior is that, although the maximum central plane filling factor $D(z = 0)$ does indeed increase with $\tau_{\rm dyn}$, the optical properties are determined by $D_{\rm eff}$ at the layer dominating the scattering. The fact that we found the HWHM of f_e to be nearly independent of $\tau_{\rm dyn}$ suggests that the variations in $D_{\rm eff}$ are much smaller than those in $D(z = 0)$. On the other hand, the maximum amplitude of f_e does increase with $\tau_{\rm dyn}$, until saturation is reached at large $\tau_{\rm path}$. This, together with nearly constant HWHM, accounts for the increased slope. Therefore, our conclusion is that the τ dependence of the outer slope gives additional support for the interparticle shadowing effect. Of course, there may be additional indirect correlations between particle surface properties and local optical depth as suggested by Deau et al. (2009).

Based on the elevation-dependent part of the observed opposition effect, we find that the C ring region we study is best described

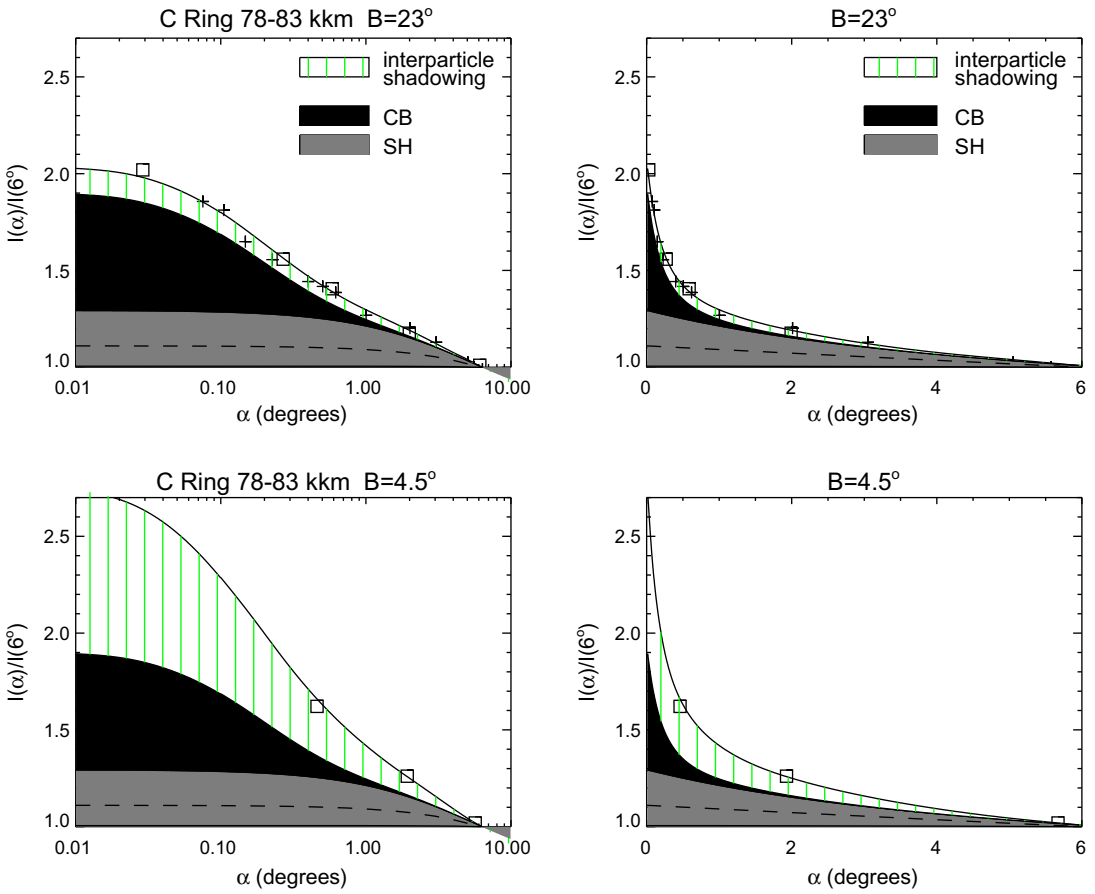

Fig. 20. Modeled contributions to the C ring opposition effect, measured in terms of $I/I(6°)$, shown for $B_{\rm eff} = 23°$ and $B_{\rm eff} = 4.5°$ (upper and lower frames, respectively), on logarithmic (left) and linear (right) scales. The models are for F336W filter: the vertically banded shaded regions indicate the SH (gray) and CB (black) contributions to the intrinsic component, obtained from a SH–CB fit to HST data from all elevations, after removal of the modeled interparticle contribution; they are identical for both $B_{\rm eff}$'s. The shaded region indicates the interparticle contribution, which depends on $B_{\rm eff}$. The interparticle contribution is calculated for the best fitting model of Section 4 (dynamical optical depth $\tau_{\rm dyn} = 0.1$, $W_s = 50$, Bridges et al. (1984) coefficient of restitution formula; photometric calculations use a Lambert law with $A = 0.5$). Symbols indicate the HST observations at the F336W filter, for the indicated $B_{\rm eff}$. The dashed line indicates the relative change of an $n_s = 3.07$ power-law phase function.

by an extended size distribution with $W_s \gtrsim 100$, whereas for the A and B rings a significantly narrower $W_s \lesssim 5$–10 is deduced. The estimated C ring lower bound is consistent with French and Nicholson (2000), who found $W_s \sim 1000$ from the analysis of forward scattered light in ground based stellar occultation data. However, for the A and B rings our upper bound is definitely smaller than $W_s \sim 70$ found by French and Nicholson (2000): most likely this discrepancy follows from the fact that the uniform ring models we have studied are too simple to describe all aspects of ring reflection and transmission.

In our models, the Bridges et al. (1984) coefficient of restitution and a power law size distribution with $q = 3$ was assumed. The dominant factor affecting the fit is the volume density $D_{\rm eff}$, which depends not only on the size distribution, but also on the elasticity of particles. Less dissipative particles lead to collisional energy balance corresponding to geometrically thicker rings, whereas increased dissipation flattens the rings, until a minimum thickness corresponding to few times the maximum particle radii is achieved (see e.g. Schmidt et al., 2009). Thus, for significantly less dissipative particles,[8] say with the scale factor $v_c = 10 v_B$ in Eq. (14) instead of $v_c = v_B$, the best fit for the C ring would be obtained for a size distribution with $W_s \gtrsim 10$ (combined with the resulting vertically thicker ring, $W_s = 10$ would lead to roughly the same $D_{\rm eff}$ as the original Bridges et al. elasticity formula in combination with $W_s = 50$). Clearly, such a narrow distribution would be very hard to reconcile with French and Nicholson (2000) estimates. On the other hand, even if the particles were more dissipative than implied by the Bridges formula (say, having a constant $\epsilon_n = 0.1$), the best fit for B and A rings would still imply a fairly narrow $W_s \sim 10$. In conclusion, we cannot claim that any unique formula for the elastic properties of particles could be deduced from the matching of the elevation-dependent opposition effect, taking into account the uncertainties in the size distribution. However, it seems that the match in terms of a Bridges et al. (1984) type, frosty particle elasticity model, is a fairly robust one, and suggests a significantly wider size distribution in the C ring in comparison to B and A rings. Most importantly for the current goal, the deduced intra-particle opposition effect contribution is not overly sensitive to which particular simulation model is used in the extraction of f_e, as long as it can correctly account for the elevation angle dependence.

After removal of the interparticle opposition effect, fits to the intrinsic opposition effect were made, using both linear-exponential and Hapke-model fits (the SH part of the latter models was simplified, as only the near-opposition part of phase curve is fitted). Both types of fits imply that the intrinsic effect is mainly due to CB (in linear-exponential model this can be identified with the exponential component). In fact, for the *B* and *A* rings the intrinsic SH contribution is almost negligible: the fitted SH component is very close to what is implied by the $n_s = 3.09$ power-law phase function used in

[8] Such systems are potentially quite interesting, as they can be susceptible to viscous instability (see Salo and Schmidt, 2010).

Dones et al., 1993, when extrapolated to near-opposition phase angles. For the C ring, the deduced intra-particle SH is less than half of the implied coherent backscattering contribution. Compared to the earlier fits based on the original high-elevation HST data, without separation of the interparticle effect (French et al., 2007b), there is rather little difference in the deduced CB parameters. In particular, the amplitude $B_{c0} \approx 0.4$ for all ring components, as in fits to the original data, whereas the HWHM $\approx 0.1°$ is slightly increased. Nevertheless, in any careful analysis of the intrinsic opposition effect aiming to deduce, for example, the regional variations in the properties of regolith-grains covering particle surfaces, the elevation dependent part should first be excluded. For example, the difference in the deduced SH components between the C ring and the higher density B and A rings, not distinguishable without exclusion of the interparticle shadowing, might reflect the different collisional environments in the ring components.

The various modeled contributions are best illustrated in Figs. 20 and 21, for the C and B rings, respectively. (The A ring case would be almost indistinguishable from the B ring.) The CB and SH contributions are shown separately by the black and gray shaded regions; these are identical in the upper and lower frames, corresponding to $B_{\rm eff} = 23.5°$ and 4.5°. The modeled interparticle shadowing contribution is shown by the dashed region, which is much more pronounced for the lower elevation. Also shown are the HST data points corresponding to the indicated $B_{\rm eff}$. (Note that the the models are based on fitting simultaneously the whole range of $B_{\rm eff}$'s.) To emphasize the extremely narrow CB peak, the phase curves are also shown on a linear scale in the right-hand frames.

For comparison with spacecraft observations, we predict the behavior of the intraparticle shadowing effect for phase curves beyond the regime accessible by ground based studies ($\alpha < 6.37°$) in Fig. 22. This shows the single scattering contribution for our adopted B ring model, now covering a full range $0° \leqslant \alpha \leqslant 180°$.

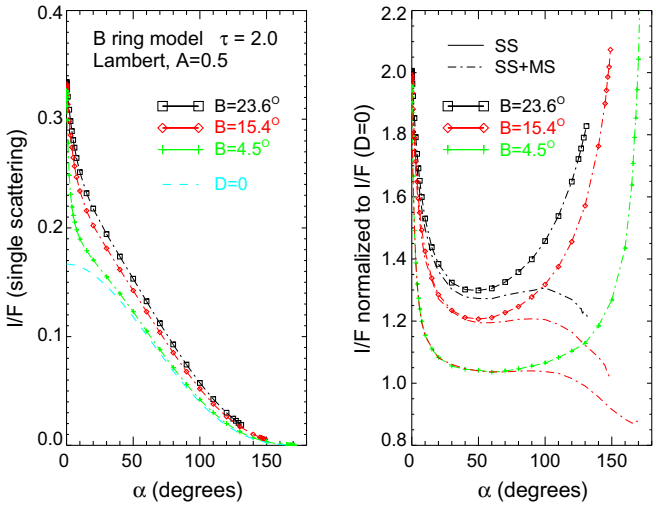

Fig. 22. The behavior of the modeled B ring I/F for a full range of phase angles (dynamical optical depth $\tau_{\rm dyn} = 2.0$, $W_s = 5$, Bridges et al. (1984) coefficient of restitution formula is assumed; together with Lambert phase function with Bond albedo $A = 0.5$). At left, the single scattering contribution is shown, for three different $B_{\rm eff}$'s. For comparison, the classical $D = 0$ single scattering contribution is also shown by a dashed line. At the right, the same single scattering model curves are shown, normalized to $D = 0$ curve. Also shown by dashed lines are corresponding ratios when both single and multiple scattering are included.

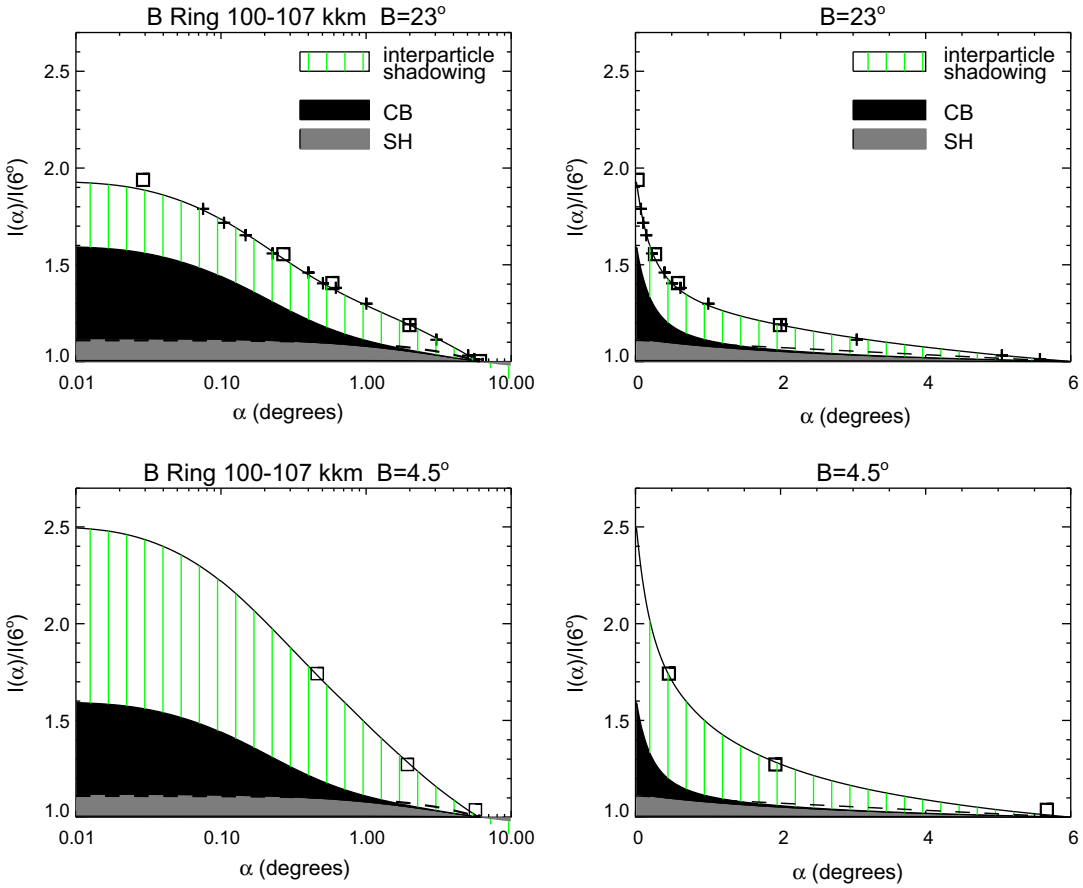

Fig. 21. Same as Fig. 20, except for the B ring region. The interparticle shadowing model is calculated for dynamical optical depth $\tau_{\rm dyn} = 2.0$, $W_s = 5$, Bridges et al. (1984) coefficient of restitution formula.

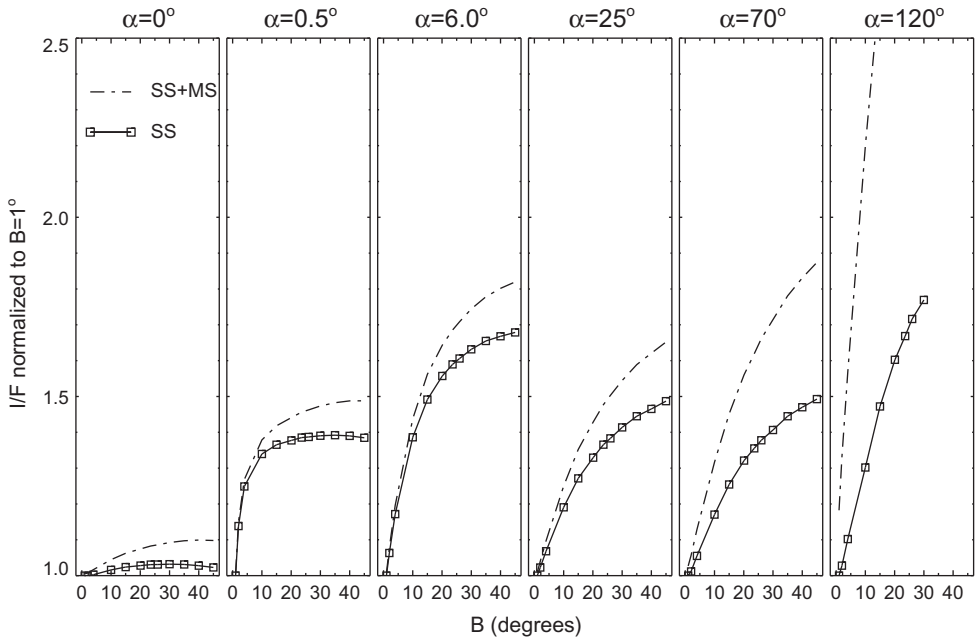

Fig. 23. Comparison of the modeled tilt effect for a range of phase angles: the dynamical/photometric parameters are the same as in Fig. 22.

Three different elevations are compared, as well as the elevation-independent theoretical $D = 0$ curve, following in form the spherical-particle Lambert phase function. According to Fig. 21, the intrinsic peak would affect just a very narrow portion near zero phase angle. On the other hand, as mentioned previously, the interparticle shadowing contribution extends to all phase angles. In fact, the relative brightening over the classical ($D = 0$) multilayer starts to increase again beyond $\alpha \approx 50°$. Clearly this is no longer an "opposition effect," but relates to a general reduction of shadowing in geometrically thin layers of particles (see footnote 5). Nevertheless, in practice this enhanced I_{ss} has little significance, since it is offset by an even larger reduction in the multiple scattering contribution (Fig. 22 right panel; see also Fig. 7 in SK2003). Since multiple scattering dominates at high phase angles, the total brightness $I/I(D = 0)$ is reduced. It was shown in SK2003 that this combination of geometrically thin layers appearing brighter in backscattering and dimmer at forward-scattering makes it possible to match simultaneously both the low and high phase angle brightnesses of the inner A ring. Indeed, for this ring region, Dones et al. (1993) found that the phase curve from Voyager images cannot be accounted for by classical radiative transfer models, and suggested that this might be due to geometrically thin rings. Clearly, a similar effect needs to be taken into account in the interpretation of Cassini ISS observations. In particular, by combining observations from several different elevations, one can eliminate the uncertainties related to particle phase function and albedo, and deduce constraints for the ring vertical profile and size distribution.[9]

[9] Porco et al. (2008) claim to have deduced accurate ring thicknesses, based on small deviations between the observed and modeled $D = 0$ phase curves, repeating calculations such as described in SK2003. However, there are problems in their approach: for example, they assume that the ring particle phase function is determined precisely by a power-law phase function, and use two observations to deduce simultaneously three unknown parameters: the ring thickness, the particle albedo, and the index n_s of a power-law phase function. Moreover, the ring models they use are not dynamically self-consistently calculated size distribution models: they assume a Gaussian distribution of identical particles, which assumption is prone to affect the resulting model brightness (see e.g. Fig. 21 in SK2003). Apart from these considerations, there also seem to be some problems in the convergence of their model results when the classical limit should be reproduced exactly (see their Figs. 10–13).

The characteristics of the B and A ring tilt effects were explored in Section 5. We showed a new observational result: the strong positive B ring tilt effect seen at $\alpha = 6°$ (the phase angle most often addressed in ground based studies) is significantly weakened when observations at $\alpha = 0.5$ are compared. We showed that the tilt effect itself, as well as its smaller amplitude as $\alpha \to 0°$, follow in a natural manner from the same models which match the elevation-dependent opposition effect. Briefly summarized, at low $B_{\rm eff}$ the width of interparticle opposition peak is much less than 6°, so that near-opposition brightening has no contribution to the ring brightness. On the other hand, when $B_{\rm eff}$ increases the opposition peak gets wider, leading to an increased contribution to the brightness. For example, the best-matching B ring interparticle shadowing model has HWHM $\sim$ 1–10°, for $B_{\rm eff} = 4$–26° (see Fig. 8). Clearly, at phase angles smaller than the minimum width, the interparticle contribution is present regardless of $B_{\rm eff}$: this accounts for the reduced tilt effect for $\alpha = 0.5°$. The A ring negative tilt effect was attributed to gravitational wakes, which have a larger effect on the reflection in the moderate-τ A ring (and the inner B ring) in comparison to the densest part of the B ring. Nevertheless, the shadowing contribution was also present, evidenced by the difference between $\alpha = 6°$ and $\alpha = 0.5°$.

The dependence of the expected B ring tilt effect as function of phase angle is further illustrated in Fig. 23: here, the second and third frames show the $\alpha = 0.5°$ and 6° cases discussed just above. (Note the arbitrary normalization to $B_{\rm eff} = 1°$.) The first frame is for exact opposition, where the predicted interparticle contribution to the tilt effect practically vanishes (the small residual effect follows from the weak dependence of maximum f_e on path optical depth). In the figure, the modeled tilt effect is shown separately for single scattering and for total brightness (single + multiple scattering): the difference between these indicates the contribution due to increased multiple scattering when $B_{\rm eff}$ increases. Also shown in Fig. 23 is the expected B ring tilt effect for phase angles >6°. Clearly, if the brightening of I_{ss} in the case of non-zero D were limited to near opposition, there would be no shadowing contribution to the tilt effect for α larger than the width of the opposition peak. However, due to the aforementioned general brightening of geometrically thin layers, the tilt effect due to enhanced I_{ss} is present

for all $\alpha's$: the strength of the effect is proportional to the difference between the various $B_{\rm eff}$ curves in Fig. 22. Additionally, for $\alpha \gtrsim 120^\circ$ the multiple scattering contribution to the tilt effect should become more and more important.

The effect of elevation-dependent interparticle shadowing, seen in the HST observations, should be present also in the Cassini ISS, VIMS, and CIRS data, particularly for the recent epoch with low solar elevation. In fact, the effect might be noticeable also for $B_{\rm eff} \sim 15$–25°, for which range Cassini data have already been analyzed. For example, often phase curve data from different tilt angles are combined together: it will be important to determine what influence this has on the fitted parameters (e.g. on the HWHM of the opposition peak). Also, removing the wavelength-independent interparticle opposition effect will affect the relative amplitudes of the intrinsic opposition peak deduced at different filters: obtaining an unbiased view of the wavelength trends of opposition peak is important for the physical interpretation of the observations. Our plan for the future is to expand our photometric modeling to cover a larger range of observing geometries relevant for Cassini, and moreover cover a larger set of dynamical models. Clearly, this will help to provide improved constraints for both the photometric properties of ring particles, as well as for the local structure of rings, influenced by the particles' physical properties and their size distribution.

Acknowledgments

We thank Luke Dones and Linda Spilker for detailed and constructive reviews. Our results are based on observations with the NASA/ESA Hubble Space Telescope, obtained at the Space Telescope Science Institute (STScI), which is operated by the Association of Universities for Research in Astronomy, Inc. under NASA Contract NAS5-26555. This work was supported in part by grants from STScI, by the Academy of Finland and by Wellesley College.

References

Akkermans, E., Wolf, P., Maynard, R., Maret, G., 1988. Theoretical study of the coherent backscattering of light by disordered media. J. Phys. 49, 77–98.
Altobelli, N., Spilker, L., Leyrat, C., Pilorz, S., Edgington, S., Flanders, A., 2009. Thermal phase curves observed in Saturn's main rings by Cassini-CIRS: Detection of an opposition effect? Geophys. Res. Lett. 36. L10105.
Araki, S., Tremaine, S., 1986. The dynamics of dense particle disks. Icarus 65, 83–109.
Bobrov, M.S., 1970. The Rings of Saturn. NASA TT F-701 (Translation of Kol'tsa Saturna, Nauka, Moscow). 128p.
Bridges, F.G., Hatzes, A., Lin, D.N.C., 1984. Structure, stability and evolution of Saturn's rings. Nature 309, 333–335.
Camichel, H., 1958. Mesures photométriques de Saturne et de son anneau. Ann. d'Astrophys. 21, 231–242.
Colombo, G., Goldreich, P., Harris, A.W., 1976. Spiral structure as an explanation for the asymmetric brightness of Saturn's A ring. Nature 264, 344–345.
Colwell, J.E., Esposito, L.W., Sremčević, M., 2006. Self-gravity wakes in Saturn's A ring measured by stellar occultations from Cassini. Geophys. Res. Lett. 33, L07201.
Colwell, J.E., Esposito, L.W., Sremčević, M., Stewart, G.R., McClintock, W.E., 2007. Self-gravity wakes and radial structure of Saturn's B ring. Icarus 190, 127–144.
Cook, A.F., Franklin, F.A., Palluconi, F.D., 1973. Saturn's rings – A survey. Icarus 18, 317–337.
Cuzzi, J.N., French, R.G., Dones, L., 2002. HST multicolor (255–1042 nm) photometry of Saturn's main rings. I. Radial profiles, phase and opening angle variations, and regional spectra. Icarus 158, 199–223.
Déau, E., Charnoz, S., Dones, L., Brahic, A., Porco, C. The opposition effect in Saturn's rings seen by Cassini/ISS: I. Morphology of phase curves. Icarus, submitted for publication.
Dollfus, A., 1996. Saturn's rings: Optical reflectance polarimetry. Icarus 124, 237–261.
Dones, L., Cuzzi, J.N., Showalter, M.R., 1993. Voyager photometry of Saturn's A ring. Icarus 105, 184–215.
Drossart, P., 1993. Optics on a fractal surface and the photometry of the regoliths. Planet. Space Sci. 41, 381–393.
Esposito, L.W., Lumme, K., 1977. The tilt effect for Saturn's rings. Icarus 31, 157–167.
Ferrari, C., Leyrat, C., 2006. Thermal emission of spherical spinning ring particles. The standard model. Astron. Astrophys. 447, 745–760.
Ferrari, C., Brooks, S., Edgington, S., Leyrat, C., Pilorz, S., Spilker, L., 2009. Structure of self-gravity wakes in Saturn's A ring as measured by Cassini CIRS. Icarus 199, 145–153.
Franklin, F.A., Cook, A.F., Barrey, R.T.F., Roff, C.A., Hunt, G.E., de Rueda, H.B., 1987. Voyager observations of the azimuthal brightness variations in Saturn's rings. Icarus 69, 280–296.
French, R.G., Nicholson, P.D., 2000. Saturn's rings II. Particle sizes inferred from stellar occultation data. Icarus 145, 502–523.
French, R.G., Salo, H., McGhee, C.A., Dones, L., 2007a. HST observations of azimuthal asymmetry in Saturn's rings. Icarus 189, 493–522.
French, R.G., Verbiscer, A., Salo, H., McGhee, C.A., Dones, L., 2007b. Saturn's rings at true opposition. PASP 119, 623–6422.
Hämeen-Anttila, K.A., Pyykko, S., 1972. Photometric behaviour of Saturn's rings as a function of the Saturnocentric latitudes of the Earth and the Sun. Astron. Astrophys. 19, 235–247.
Hämeen-Anttila, K.A., Vaaraniemi, P., 1975. A theoretical photometric function of Saturn's rings. Icarus 25, 470–478.
Hapke, B., 1986. Bidirectional reflectance spectroscopy. IV – The extinction coefficient and the opposition effect. Icarus 67, 264–280.
Hapke, B., 1990. Coherent backscatter and the radar characteristics of outer planet satellites. Icarus 88, 407–417.
Hapke, B., 2002. Bidirectional reflectance spectroscopy. V – The coherent backscatter opposition effect and anisotropic scattering. Icarus 157, 523–534.
Hapke, B.W., and 29 colleagues, 2006. Cassini observations of the opposition effect of Saturn's rings 2. Interpretation: Plaster of Paris as an analog of ring particles. Lunar Planet. Inst. Conf. Abstr. 37, 1466–1467.
Hapke, B.W., Shepard, M.K., Nelson, R.M., Smythe, W.D., Piatek, J.L., 2009. A quantitative test of the ability of models based on the equation of radiative transfer to predict the bidirectional reflectance of a well-characterized medium. Icarus 199, 210–218.
Hedman, M.M., Nicholson, P.D., Salo, H., Wallis, B.D., Buratti, B.J., Baines, K.H., Brown, R.H., Clark, R.N., 2007. Self-gravity wake structures in Saturn's A ring revealed by Cassini VIMS. Astron. J. 133, 2624–2629.
Irvine, W.M., 1966. The shadowing effect in diffuse reflection. J. Geophys. Res. 71, 2931–2937.
Irvine, W.M., Muinonen, K., Lumme, K., 1988. Is the mutual shadowing explanation for the opposition effect of Saturn's rings still valid? Bull. Am. Astron. Soc. 20, 853.
Johnson, P.E., Kemp, J.C., King, R., Parker, T.E., Barbour, M.S., 1980. New results from optical polarimetry of Saturn's rings. Science 283, 146–149.
Kaasalainen, S., Piironen, J., Kaasalainen, M., Harris, A.W., Muinonen, K., Cellino, A., 2003. Icarus 161, 34–46.
Lumme, K., 1970. On photometric properties of Saturn's rings. Astrophys. Space Sci. 8, 90–101.
Lumme, K., Bowell, E., 1981. Radiative transfer in the surfaces of atmosphereless bodies. I – Theory. Astron. J. 86, 1694–1704.
Lumme, K., Irvine, W.M., 1976a. Azimuthal brightness variations of Saturn's rings. Astrophys. J. 204, L55–L57.
Lumme, K., Irvine, W.M., 1976b. Photometry of Saturn's rings. Astron. J. 81, 865–893.
Lumme, K., Irvine, W.M., Esposito, L.W., 1983. Theoretical interpretation of the ground-based photometry of Saturn's B ring. Icarus 53, 174–184.
Lyot, B., 1929. Recherce sur la polarization de la lumière des planètes et de quelques substances terrestres. Ann. Obs. Meudon VIII, Fasc 1. (NASA-TTF-187, 1964).
Marouf, E.A., Tyler, G.L., Zebker, H.A., Simpson, R.A., Eshleman, V.R., 1983. Particle size distributions in Saturn's rings from Voyager 1 radio occultation. Icarus 54, 189–211.
McGhee, C.A., French, R.G., Dones, L., Cuzzi, J.N., Salo, H.J., Danos, R., 2005. HST observations of spokes in Saturn's B ring. Icarus 173, 508–521.
Mishchenko, M.I., 1992. The angular width of the coherent back-scatter opposition effect – An application to icy outer planet satellites. Astrophys. Space Sci. 194, 327–333.
Mishchenko, M.I., 1993. On the nature of the polarization opposition effect exhibited by Saturn's rings. Astrophys. J. 411, 351–361.
Mishchenko, M.I., Dlugach, Z.M., 1992. Can weak localization of photons explain the opposition effect of Saturn's rings? MNRAS 254, 15P–18P.
Morishima, R., Salo, H., Ohtsuki, K., 2009. A multi-layer model for thermal infrared emission of Saturn's rings: Basic formulation and implications for Earth-based observations. Icarus 201, 634–654.
Muinonen, K.O., Sihvola, A.H., Lindell, I.V., Lumme, K.A., 1991. Scattering by a small object close to an interface. II. Study of backscattering. J. Opt. Soc. Am. A 8, 477–482.
Nelson, R.M., 2008. Laboratory investigations relevant to Cassini VIMS reports of coherent constructive interference in Saturn's rings. In: 37th COSPAR Scientific Assembly, Plenary Meeting, July 3–20, 2008, Montréal, Canada, Paper Number: B08-0009-08.
Nelson, R.M., Hapke, B.W., Smythe, W.D., Spilker, L.J., 2000. The opposition effect in simulated planetary regoliths. Reflectance and circular polarization ratio change at small phase angle. Icarus 147, 545–558.
Nelson, R.M., Smythe, W.D., Hapke, B.W., Hale, A.S., 2002. Low phase angle laboratory studies of the opposition effect: Search for wavelength dependence. Planet. Space Sci. 50, 849–856.
Nicholson, P., French, R.G., Campbell, D.B., Margot, J.-L., Nolan, M.C., Black, G.J., Salo, H., 2005. Radar imaging of Saturn's rings. Icarus 177, 32–62.
Peltoniemi, J.I., Lumme, K., 1992. Light scattering by closely packed particulate media. J. Opt. Soc. Am. A 9, 1320–1326.

Plass, G.N., Kattawar, G.W., 1968. Monte Carlo calculations of light scattering from clouds. Appl. Opt. 7, 415–419.
Porco, C.C., Weiss, J.W., Richardson, D.C., Dones, L., Quinn, T., Throop, H., 2008. Simulations of the dynamical and light-scattering behavior of Saturn's rings and the derivation of ring particle and disk properties. Astron. J. 136, 2172–2200.
Poulet, F., Cuzzi, J.N., French, R.G., Dones, L., 2002. A study of Saturn's ring phase curves from HST observations. Icarus 158, 224–248.
Price, M.J., 1973. Optical scattering properties of Saturn's rings. Astron. J. 78, 113–120.
Rosenbush, V., Avramchuk, V., Rosenbush, A., Mishchenko, M., 1997. Polarization properties of the Galilean satellites of Jupiter: Observations and preliminary analysis. Astrophys. J. 487, 402–412.
Salo, H., 1988. Monte Carlo modeling of the net effects of coma scattering and thermal reradiation on the energy input to cometary nucleus. Icarus 76, 253–269.
Salo, H., 1992a. Numerical simulations of dense collisional systems. II – Extended distribution of particle sizes. Icarus 96, 85–106.
Salo, H., 1992b. Gravitational wakes in Saturn's rings. Nature 359, 619–621.
Salo, H., 1995. Simulations of dense planetary rings. III. Self-gravitating identical particles. Icarus 117, 287–312.
Salo, H., Karjalainen, R., 2003. Photometric modeling of Saturn's rings: I. Monte Carlo method and the effect of nonzero volume filling factor. Icarus 164, 428–460. SK2003.
Salo, H., Schmidt, J., 2010. N-body simulations of viscous instability of planetary rings. Icarus 206, 390–409.
Salo, H., Schmidt, J., Spahn, F., 2001. Viscous overstability in Saturn's B-ring: I. Direct simulations and measurement of transport coefficients. Icarus 153, 295–315.
Salo, H., Karjalainen, R., French, R.G., 2004. Photometric modeling of Saturn's rings. II. Azimuthal asymmetry in reflected and transmitted light. Icarus 170, 70–90.
Schmidt, J., Ohtsuki, K., Rappaport, N., Salo, H., Spahn, F., 2009. Dynamics of Saturn's dense rings. In: Brown, R.H., Dougherty, M. (Eds.), Saturn after Cassini–Huygens. Kluwer, pp. 413–458.
Shepard, M.K., Helfenstein, P., 2007. A test of the Hapke photometric model. J. Geophys. Res. 112, 1–17. EO3001.
Shkuratov, I.G., 1988. A diffraction mechanism for the formation of the opposition effect of the brightness of surfaces having a complex structure. KFNT 4, 33–39.
Shkuratov, Y.G., Kreslavsky, M.A., Ovcharenko, A.A., Stankevich, D.G., Zubko, E.S., Pieters, C., Arnold, G., 1999. Opposition effect from Clementine data and mechanisms of backscatter. Icarus 141, 132–155.
Shkuratov, Y., Bondarenko, S., Kaydash, V., Videen, G., Muñoz, O., Volten, H., 2007. Photometry and polarimetry of particulate surfaces and aerosol particles over a wide range of phase angles. J. Quant. Spectrosc. Radiat. Trans. 106, 487–508.
Showalter, M.R., Bollinger, K.J., Nicholson, P.D., Cuzzi, J.N., 1996. The rings node for the planetary data system. Planet. Space Sci. 44, 33–45.
Thompson, W.T., Lumme, K., Irvine, W.M., Baum, W.A., Esposito, L.W., 1981. Saturn's rings – Azimuthal variations, phase curves, and radial profiles in four colors. Icarus 46, 187–200.
Toomre, A., Kalnajs, A.J., 1991. Spiral chaos in an orbital patch. In: Sundelius, B. (Ed.), Dynamics of Disc Galaxies. Almquist-Wiksell, pp. 341–358.
van de Hulst, H.C., 1980. Multiple Light Scattering. Tables, Formulas and Applications. Academic Press, New York.
Wisdom, J., Tremaine, S., 1988. Local simulations of planetary rings. Astron. J. 95, 925–940.